Classical and Quantum Critical Phenomena in the Dipolar Antiferromagnet LiErF$_4$

THÈSE N^O 5372 (2012)

PAR

Neda NIKSERESHT GHANEPOUR

(EPFL

ÉCOLE POLYTECHNIQUE
FÉDÉRALE DE LAUSANNE

Suisse
2012

Acknowledgements

I would like to thank my supervisor Henrik Rønnow for all his supports during the last four years. Obviously, this project would not have reached to this satisfactory stage if it was not guided properly by an expert. Working with Henrik was a great pleasure for me, and gave me the opportunity to recognize my abilities, become more independent while still feel supported. I admire his wonderful talents and creative ideas, and appreciate his way of trusting his students, and giving them the chance and courage to try what they are mostly interested in.

Many thanks go to prof. Romuald Houdré, the president of my PhD defence, and the jury members Prof. Jens Jensen, Steve Bramwell, and Marco Grioni for the careful reading of the manuscript and their useful comments for improving the thesis.

Many thanks to Jose Rodriguez, who performed the analysis of the μSR experiment we performed at PSI. He is not only a good scientist but also a great teacher. Through him I learned the basics of this completely new area. I very much appreciate his simple way of explaining complicated problems and his patience in answering all my elementary questions. I would also like to thank Klaus Kiefer and Bastian Klemke at the Helmholtz Center Berlin (Laboratory for Magnetic Measurements LaMMB - MagLab) for their great help in specific heat measurements. In addition, we got many supports from Klaus regarding to sample environment and cryogenics for our neutron experiments at HZB, where stable dilution temperatures within few mK was inevitable for the critical exponent measurements. Karel Prokes and Slavomir Matas helped for the order parameter measurements at E4 diffractometer, and Markos Skoulatos was a great company for the correlation length measurements on V2 triple–axis–spectormeter at HZB. Rob Bewley at ISIS arranged us three beamtimes within the last year of my PhD at unique time–of–flight facility LET, which provided the beautiful inelastic data on LiErF$_4$ presented at the end of chapter 4. Niels B. Christensen, who taught me the principles of TAS for my very first neutron experiments, was more than a local contact

Acknowledgements

Abstract

The collective behavior of systems consisting of interacting dipoles is a subject of considerable studies. The anisotropic nature of such interactions opens an arena to explore fundamental questions in correlated electron physics, ranging from quantum entanglement, phase transitions, spin glass states to disorder and fluctuations. $LiHoF_4$ is a textbook example of a ferromagnetic Ising-dipolar model, offering a simple and well-understood Hamiltonian. The system undergoes a quantum phase transition (QPT) in a field transverse to the easy axis, which induces quantum fluctuations between the ground state doublet. Dilution of Ho sites with non–magnetic Yttrium ions lowers only the transition temperature (T_c), and eventually lead to spin–glass state. While T_c decreases in a linear fashion, as expected from simple mean–field (MF) calculation, critical field decreases much faster. The behavior upon dilution has been pointed out to be related to randomness and off–diagonal dipolar interactions. In chapter 5 of this thesis I quantify the deviation of experimental results from neutron scattering studies from MF prediction, with the aim that this analysis can be used in future theoretical efforts towards a quantitative description.

The aim of this thesis, however, deals with $LiErF_4$ which is an unexplored planar dipolar antiferromagnetic member of $LiReF_4$ family, with $T_N \simeq 370$ mK. The system undergoes a QPT in an applied field $H_{\parallel c} = 4.0 \pm 0.1$ kOe, confirmed by a softening of the characteristic excitations at H_c. A combined neutron scattering, specific heat, and magnetic susceptibility study reveals a novel non–MF critical scaling of the classical phase transition, belonging to the $2DXY/h_4$ universality class. In accord with this, the quantum phase transition at H_c exhibits a three-dimensional classical behavior. The effective dimensional reduction may be a consequence of the intrinsic anisotropic nature of the dipolar interaction. Four-fold anisotropy and degeneracy breaking could be due to the "order-by-disorder" phenomena, which could open a gap in dispersion of the magnetic excitations.

Abstract

keywords: magnetism, neutron scattering, universality class, quantum phase transition, classical phase transition, Ising and XY models, order-by-disorder.

Résumé

Les comportements collectifs des systèmes contenant des dipoles interagissant entre eux sont sujets à de nombreuses études. La nature anisotrope de ces intéractions ouvre un vaste champ d'investigation sur les questions fondamentales concernant la physique des systèmes d'électrons corrélés, tels que l'intrication quantique, les transitions de phase, les verres de spin ,*etc.*. Le LiHoF$_4$ est un exemple typique de système ferromagnétique de type Ising, possédant un Hamiltonien simple et bien compris. Le système subit une transition de phase quantique (QPT) dans un champ transverse à l'axe facile, ce qui induit des fluctuations quantiques entre les doublets de l'état fondamental. La dilution des sites d'Ho par de l'Yttrium non magnétique diminue la température de transition T$_c$, et peut amener à un état de verre de spin. Alors que T$_c$ décroît linéairement, suivant les prédictions de calculs de champ moyen, le champ critique décroît beaucoup plus rapidement. Le comportement en fonction de la dilution se révèle avoir pour origines le caractère aléatoire de la distribution des sites d'Y et les termes non diagonaux des intéractions dipolaires. Dans le chapitre 5 de cette thèse, je quantifie la déviation entre les résultats expérimentaux obtenus par diffusion de neutrons et les prédictions des calculs de champ moyen, afin que cette analyse puisse être utile pour de futurs travaux théoriques permettant une description quantitative.

Cependant, le principal objet de cette thèse est le LiErF$_4$, membre de la famille des LiReF$_4$, qui est un système antiferromagnétique dipolaire planaire encore inexploré, dont la température de transition est T$_N$=370 mK. Le système subit une QPT sous un champ magnétique $H_{\parallel c} = 4.0 \pm 0.1$ kOe, caratérisé par une atténuation des excitations caractéristiques à H$_c$. Les études combinées de diffusion de neutrons, de chaleur spécifique et de susceptibilité magnétique revèlent dans la transition de phase classique une nouvelle dimensionnalité critique n'ayant pas pour origine le champ moyen, qui appartient à la classe d'universalité $2DXY/h_4$. Le comportement de la transition de phase quantique est tridimentsionnel, ce qui est le résultat attendu, compte tenu de la bidimensionalité de la transition classique. Cette réduction de dimensionnalité

Abstract

pourrait être une conséquence de la nature intrinsèquement isotrope de l'interaction dipolaire. L'anisotropie h_4 et la levée de dégénérescence peuvent être dues à un phénomène d'*order-by-disorder,* qui pourrait ouvrir un gap dans la dispersion des excitations magnétiques.

mots-clefs : magnétisme, diffusion de neutrons, classes d'universalité, transition de phase quantique, transition de phase classique, modèles d'Ising et XY, phénomènes d'*order-by-disorder.*

Contents

Contents

1 Introduction

Magnetic behavior of a macroscopic system is a collective phenomenon, which arises from the cooperation of many microscopic particles the system has been composed of. Within the last decades, magnetism has attracted enormous theoretical and experimental investigations, where the concerns in understanding the fundamental questions is seconded by technological interests in finding new materials for use as permanent magnets, and information storage devices [1, 2]. Although the most fundamental interaction in electromagnetism, dipolar systems have been less studied mostly due to the lack of enough material realizations with such dominant forces.

In the context of phase transitions and order-disorder phenomena, where great efforts have been made to understand the basic mechanics driving the nature of the transition, dipolar systems are excellent materials to test the concept; *e.g.* $LiHoF_4$, with simple and well-understood Ising Hamiltonian, is a realization of a quantum phase transition (QPT) in transverse field to the easy axis [3, 4, 5, 6].

Rare earth (Re) lithium fluorides, $LiReF_4$, where tightly localized 4f electrons are far enough apart for the dipolar interactions to dominate exchange interactions, are rich candidates to study the physics governing dipolar-coupled systems. To date, the $LiHoF_4$ ferromagnetic model and its diluted series with non magnetic Yttrium (Y) ions (to test the effect of disorder and randomness in the behavior of the real systems) have been the center of many investigations [7, 8, 9, 10, 11, 12].

With the development of renormalization group (RG) theory, the critical exponents of various systems could be investigated in the vicinity of the phase transitions. Systems with similar macroscopical symmetries, but very different in microscopical properties,

were found to lie in the same universality class. Therefore, high-precision experimental studies of the critical behavior around critical points classify the system into the corresponding category, and open the avenue to distinguish the observed properties. To this regard, $LiReF_4$, whose 3D long–ranged dipolar interactions place them at the upper marginal dimension for the applicability of the mean-field theory, are interesting subjects to test the role of anisotropy and critical fluctuations on the nature of the magnetic systems.

This research project has focused on $LiErF_4$, an antiferromagnetic (AFM) member of the $LiReF_4$ family, which has not received much attention except from few studies mostly in 1970s and 1980s [13, 14, 15, 16, 17]. With the advantage of the weak nuclear-electronic sub-system couplings [18, 19], that can be even canceled by replacing the nuclear-spin free ^{168} Er isotopes, the material highlights a QPT in a magnetic field of 40 kOe applied transverse to the easy plane.

This PhD thesis is organized as follows:

- Chapter 2 presents a brief collection of the theoretical background on QPT and mean-field (MF) theory. The Hamiltonian of the $LiReF_4$ system is derived, and the generalized susceptibility and MF/RPA calculations are explained.

- Chapter 3 outlines methods used within this work. Neutron scattering, as the primary experimental method, and its instrumentation depending on the subject of study are introduced. A few complementary methods *e.g.* specific heat, AC-susceptibility and muon spin rotation are presented. Sample environment, dilution refrigerator and split-coil magnets extensively used in this research are discussed, following a brief introduction to $LiReF_4$ system.

Results are divided into two chapters: The relevant background is given in the beginning of each chapter, and the results are compared with earlier studies, being referred to the related literature.

- In chapter 4, $LiErF_4$, the core of this project has been introduced. Magnetic structure and the classical and quantum phase transitions are described. A set of critical exponents classifying the system into the 2DXY/h_4 universality class

are derived. Energy excitations and dynamics of the system, which could be modeled by MF/RPA picture, have been studied.

- In chapter 5, LiHo$_x$Y$_{1-x}$F$_4$ (0.25 $\leq x \leq$ 1), an example of a random field quantum Ising magnet in a transverse field has been investigated briefly. The phase diagram mapped by means of neutron scattering is compared with MF calculations.

2 General theory

2.1 Quantum phase transition

In *classical phase transitions* that occur at finite temperatures, critical properties are determined by thermal fluctuations. There exist another type of transitions taking place at "zero temperature", driven by quantum fluctuations, called *quantum phase transitions (QPT)*. In the systems exhibiting QPT, the order–disorder transition between two different quantum ground states is due to an external applied magnetic field, pressure or variation in chemical composition. Although both quantum and classical ($T > 0$) phase transitions might happen in the same system, they are of different nature, since in the latter thermal fluctuations are the control parameter.

Because the distances (l) and timescales ($\tau \propto 1/\omega$) over which the order parameter fluctuates coherently increase towards the transition, the correlation length (ξ_l) and the correlation time (ξ_τ) diverge. In the quantum mechanical picture τ–divergence corresponds to a vanishing energy ($E = \hbar\omega$), according to the energy-time uncertainty principle ($\Delta E \Delta t \sim \hbar$). Within this characteristic time there is a correlation between the sites and their neighbors, which leads to an additional dimension to the system [20]. The time scale and length scale divergences are connected through the dynamic exponent z [21]:

$$\xi_\tau = \xi_l{}^z.$$ (2.1)

Therefore, a classical d–dimensional system maps into $d + z$ at QPT. In the simple Ising-like compounds, $z = 1$, whereas in strongly correlated or disordered systems it can show higher values [22]. A schematic phase diagram of a system exhibiting QPT is illustrated in Fig. 2.1. On the other hand, at finite temperatures where $k_B T_c \gg \hbar\omega$, the time divergence is cut off, as a consequence of thermal fluctuations [23].

A textbook example of a QPT is the Ising ferromagnet in the presence of a transverse applied magnetic field. In the basis of the uniaxial axis the Hamiltonian of the system has the form:

$$\mathcal{H} = -\mathcal{J}\sum_{i,j}^{N}\sigma_i{}^z\sigma_j{}^z - \Gamma\sum_i^N\sigma_i{}^x, \tag{2.2}$$

where σ_i's are the Pauli matrices, $\mathcal{J}$ represents the coupling strength, and Γ is the transverse field, which introduces off-diagonal terms into the Hamiltonian.
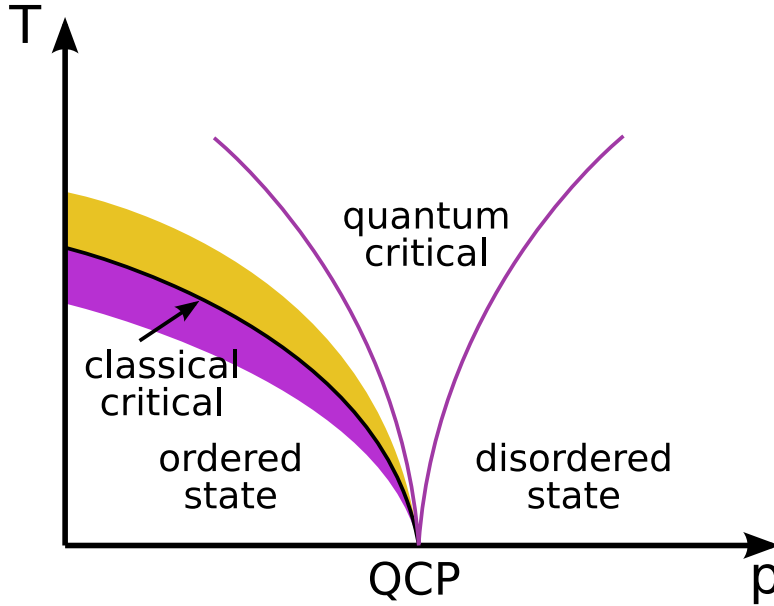
Figure 2.1: Schematic phase diagram of a system exhibiting quantum phase transition as a function of a control parameter p.

2.2 Magnetism in rare-earth fluorides

Magnetism is basically the collective response of the magnetic units of a magnetic material, induced by the spin and angular momentum motion of the electrons. Within the last decades, magnetism is the subject of many experimental tests in many body

physics and correlated electron systems. However, the quantitative understanding is often not trivial in complex magnetic systems. Therefore, pure compounds with well characterized Hamiltonian have attracted great interest. LiReF$_4$ where Re=*rare earth*, provide an ideal example to study dipolar interactions, and have been investigated both theoretically and experimentally [24, 16, 17, 14, 13, 15, 4].

The strong spin–orbit coupling in $4f$ valance electrons of Re^{3+} dominates the crystal field effect of the surrounding F$^-$ ions. Therefore, the ground state can preserve its degeneracy, having the maximum angular momentum J. Due to the small radius of the $4f$ shell, the electrons in this layer are tightly bound to the nucleus, causing *Hyperfine* interactions. The lack of orbital overlap leads to very small nearest neighbor exchange interactions compared to the long-range dipolar interactions. The total Hamiltonian describing the magnetic model of LiReF$_4$ is given by:

$$\mathcal{H} = \mathcal{H}_{cf} + \mathcal{A}\sum_i \mathbf{I}_i \cdot \mathbf{J}_i - g\mu_B \sum_i \mathbf{H} \cdot \mathbf{J}_i - \sum_{i,j}\sum_{\alpha,\beta} \mathcal{D}_{i,j}^{\alpha\beta} J_i{}^\alpha J_j{}^\beta - \mathcal{J}\sum_{i,j} \mathbf{J}_i \cdot \mathbf{J}_j, \qquad (2.3)$$

where the first three terms are due to the single ion interactions, called crystal field, hyperfine coupling (with coupling strength $\mathcal{A}$), and Zeeman term in an applied field H, respectively. The two latter items describe the the dipolar and exchange inter-ion interactions.

In LiReF$_4$ the nearest-neighbor exchange interactions, $\mathcal{J}\sum_{i,j}\mathbf{J}_i \cdot \mathbf{J}_j$, are much smaller than the long range dipole-dipole couplings of the $4f$ electron moments:

$$\mathcal{H}_{ij}^D = \sum_{\alpha,\beta} \mathcal{D}_{i,j}^{\alpha\beta} J_i{}^\alpha J_j{}^\beta = (\mu_B g)^2 \left[\frac{\mathbf{J}_i \cdot \mathbf{J}_j}{\mathbf{r}_{ij}^3} - \frac{3(\mathbf{J}_i \cdot \mathbf{r}_{ij})(\mathbf{J}_j \cdot \mathbf{r}_{ij})}{\mathbf{r}_{ij}^5} \right]. \qquad (2.4)$$

g is the *Landé* factor:
$$g = \frac{3}{2} + \frac{S(S+1) - L(L+1)}{2J(J+1)}. \qquad (2.5)$$

The *hyperfine* interactions between the $4f$ moments and the nuclear spins $\mathbf{I}$,

$$\mathcal{H}^{hf} = \mathcal{A}\sum_i \mathbf{I}_i \cdot \mathbf{J}_i \qquad (2.6)$$

with the coupling constant $\mathcal{A}$ in the order of few μeV can influence the low temperature behavior of the system, *e.g.* when the electronic energy scale is reduced close to a

QPT.

2.2.1 Crystal field

The electric field produced by charge distribution around F^- ions in the lattice interact with the rare earths' $4f$ electron shell via Coulomb repulsion. As mentioned, in $LiReF_4$ the spin-orbit coupling ($\sim \mathbf{L} \cdot \mathbf{S}$) is stronger than the crystal field energy. Therefore, the ground state can appear as a multiplet of degenerate states. The electrical potential felt by $4f$ electrons arising from the neighboring ions with the charge density $\rho(\mathbf{r})$ is given by:

$$V_{cf}(\mathbf{r}) = \int \frac{e\rho(\mathbf{r})}{|\mathbf{R} - \mathbf{r}|} d\mathbf{r}. \tag{2.7}$$

In the frame of spherical harmonics the crystal field potential can be written in terms of multipole expansion:

$$V_{cf}(\mathbf{r}) = \sum_{lm} A_l{}^m \mathbf{r}^l Y_{lm}(\hat{\mathbf{r}}). \tag{2.8}$$

According to Stevens [25], the matrix elements of $V_{cf}(\mathbf{r})$ are proportional to the operator equivalents in terms of the $\mathbf{J}$ operators [26]. Therefore, the crystal field can be described by *Stevens factors* (α) depending on the electronic charge distribution of orbitals' angular momentum:

$$\mathcal{H}_{cf} = \sum_i \sum_{lm} A_l{}^m \alpha_l \langle \mathbf{r}^l \rangle \left(\frac{2l+1}{4\pi} \right)^{\frac{1}{2}} \tilde{\mathbf{O}}_{lm}(\mathbf{J}_i). \tag{2.9}$$

$\tilde{\mathbf{O}}_{lm}(\mathbf{J})$ operators are obtained from spherical harmonics transformed into Cartesian basis in terms of $\mathbf{J}$ operators. It is more convenient to write Eq. 2.9 in terms of *Stevens operators,* where the real combination of the spherical harmonics is taken into account:

$$\mathcal{H}_{cf} = \sum_i \sum_{lm} B_l{}^m \mathbf{O}_l{}^m(\mathbf{J}_i). \tag{2.10}$$

$B_l{}^m$ are *crystal field parameters*, and $\mathbf{O}_l{}^m$ the *Stevens* operators. Because the electronic charge distribution around the ions is usually not accurately known, crystal field parameter calculation is not a trivial task. One way to calculate them is the *point charge* calculation, replacing all atoms inside the unit cell with point charges. Neglecting the electron cloud in favor of a simple point charge is a crude approximation, which is the reason for the little success of point charge calculation at the quantitative levels [26]. However, experiment is the most accurate way to get the crystal field set of parameters. Neutron and optical spectroscopy are in fact powerful techniques in crystal field energy level determinations [24, 18].

Crystal field parameters are symmetry restricted, and in the case of LiReF$_4$ (with S_4 point-group symmetry) they have the following form:

$$\mathcal{H}_{cf} = \sum_{l=2,4,6} B_l{}^0 \mathbf{O}_l{}^0 \sum_{l=4,6} B_l{}^4(c)\mathbf{O}_l{}^4(c) + B_6{}^4(s)\mathbf{O}_6{}^4(s). \tag{2.11}$$

The x-axis is in the *ab* plane, resulting in $B_4{}^4(s) = 0$. In this representation, the Stevens operators are expressed by:

$$
\begin{aligned}
\mathbf{O}_2^0 &= 3\mathbf{J}_z^2 - \mathbf{X} \\
\mathbf{O}_4^0 &= 35\mathbf{J}_z^4 - (30\mathbf{X} - 25)\mathbf{J}_z^2 + 3\mathbf{X}^2 - 6\mathbf{X} \\
\mathbf{O}_4^4(c) &= \frac{1}{2}(\mathbf{J}_+^4 + \mathbf{J}_-^4) \\
\mathbf{O}_6^0 &= 231\mathbf{J}_z^6 - (315\mathbf{X} - 735)\mathbf{J}_z^4 + (105\mathbf{X}^2 - 525\mathbf{X} + 294)\mathbf{J}_z^2 \\
&\quad -5\mathbf{X}^3 + 40\mathbf{X}^2 - 60\mathbf{X} \\
\mathbf{O}_6^4(c) &= \frac{1}{4}\left[(11\mathbf{J}_z^2 - \mathbf{X} - 38)(\mathbf{J}_+^4 + \mathbf{J}_-^4) + (\mathbf{J}_+^4 + \mathbf{J}_-^4)(11\mathbf{J}_z^2 - \mathbf{X} - 38)\right] \\
\mathbf{O}_6^4(s) &= \frac{1}{4i}\left[(11\mathbf{J}_z^2 - \mathbf{X} - 38)(\mathbf{J}_+^4 - \mathbf{J}_-^4) + (\mathbf{J}_+^4 - \mathbf{J}_-^4)(11\mathbf{J}_z^2 - \mathbf{X} - 38)\right],
\end{aligned}
\tag{2.12}
$$

where $\mathbf{X} \equiv \mathbf{J}(\mathbf{J} + 1)$. Diagonalizing the crystal field Hamiltonian gives the crystal field energy levels and eigenfunctions.

2.3 Introduction to mean-field theory

Mean field (MF) theory basically approximates the two-ion interactions as a single ion interaction with a bath including surrounding ions. This mean interaction is the same at each site, therefore the solution of the Hamiltonian. In the case of a ferromagnetic interaction, the average response is proportional to the magnetization of the system. Let us assume a simple form of the Hamiltonian for a magnetic system in a constant applied magnetic field $\mathbf{H}$:

$$\mathcal{H} = \sum_i \mathcal{H}_{cf}(i) - g\mu_B \sum_i \mathbf{J}_i \cdot \mathbf{H} - \frac{1}{2} \sum_{ij} \mathcal{J}_{ij} \mathbf{J}_i \cdot \mathbf{J}_j, \tag{2.13}$$

$\mathbf{J}_i \cdot \mathbf{J}_j$ in the Hamiltonian can be replaced by:

$$\mathbf{J}_i \cdot \mathbf{J}_j = (\mathbf{J}_i - <\mathbf{J}_i>) \cdot (\mathbf{J}_j - <\mathbf{J}_j>) + \mathbf{J}_i \cdot <\mathbf{J}_j> + \mathbf{J}_j \cdot <\mathbf{J}_i> - <\mathbf{J}_i> \cdot <\mathbf{J}_j> . \tag{2.14}$$

Since in the mean-field approximation the fluctuations of the magnetic moments around their equilibrium value are neglected, the first term in the right hand side of the Eq. 2.14 disappears. $\mathcal{J}$ is the coupling term and $<\mathbf{J}>$ stands for thermal average of $\mathbf{J}$ operators of the neighboring ions. Rewriting the Hamiltonian in the mean-field (MF) gives:

$$\mathcal{H}_{MF} = \sum_i \mathcal{H}_{cf}(i) - \sum_i \mathbf{J}_i \cdot h - \sum_i \sum_j \mathcal{J}_{ij} \left(\mathbf{J}_i - \frac{1}{2} <\mathbf{J}_i> \right) \cdot <\mathbf{J}_j>, \tag{2.15}$$

Where, $h = g\mu_B \mathbf{H}$, and an effective field can be introduced by:

$$h_i^{eff} = h + \sum_j \mathcal{J}_{ij} <\mathbf{J}_j> . \tag{2.16}$$

Therefore, the mean field Hamiltonian can be written in form of an effective field, h_i^{eff}:

$$\mathcal{H}_{MF} = \sum_i \mathcal{H}_{cf}(i) - \sum_i \mathbf{J}_i \cdot h_i^{eff} + \frac{1}{2} \sum_i <\mathbf{J}_i> \cdot (h_i^{eff} - h). \tag{2.17}$$

With a starting point for $< \mathbf{J}_j >$, the effective field and hence the $\mathcal{H}_{MF}$ for the ith site can be calculated. Diagonalizing the Hamiltonian gives the $< \mathbf{J}_i >$ at each site, which can be an input for the new mean-field Hamiltonian. This process continues until the self-consistency is attained, which for a ferromagnetic case is a non zero magnetization even at zero field, describing the spontaneous magnetic ordering. In the presence of an antiferromagnetic ordering, a finite staggered magnetization is characteristic for the solution of the mean field Hamiltonian.

From $< \mathbf{J}_i >$ extracted through diagonalizing the MF Hamiltonian, the susceptibility can be calculated. Let us denote the $(2J+1)$ eigenstates and energies by $|m>$ and E_m, respectively. A small change in the effective field (δh_β^{eff}), introduces a new set of energies and eigenstates, which in the first order perturbation is given by:

$$E'_m \;=\; E_m - \langle m|J_{i\beta}|m\rangle \delta h_\beta^{eff} \tag{2.18}$$

$$|m'> \;=\; |m> - \delta h_\beta^{eff} \sum_n |n> <n|J_{i\beta}|m> / (E_m - E_n). \tag{2.19}$$

Hence, to first order in δh_β^{eff}, $< J'_{i\alpha} >$ would be:

$$
\begin{aligned}
< J'_{i\alpha} > = \sum_m < m'|J_{i\alpha}|m' > N'_m &= \sum_m < m|J_{i\alpha}|m > N'_m \\
&- \delta h_\beta^{eff} \sum_{mn} < m|J_{i\alpha}|n > < n|J_{i\beta}|m > N_m / (E_m - E_n) \\
&- \delta h_\beta^{eff} \sum_{mn} < m|J_{i\beta}|n > < n|J_{i\alpha}|m > N_m / (E_m - E_n).
\end{aligned}
\tag{2.20}
$$

N_m and N'_m are the population factors for $\delta h_\beta^{eff} = 0$ and $\delta h_\beta^{eff} \neq 0$, respectively. Therefore, the susceptibility is calculated from:

$$
\chi_{\alpha\beta}^0(i) = \frac{\partial < J_{i\alpha} >}{\partial h_\beta^{eff}} = \sum_{mn}^{E_m \neq E_n} \frac{< m|J_{i\alpha}|n > < n|J_{i\beta}|m >}{E_n - E_m} (N_m - N_n) \tag{2.21}
$$

$$
+ \beta \sum_{mn}^{E_m = E_n} < m|J_{i\alpha}|n > < n|J_{i\beta}|m > N_m - \beta < J_{i\alpha} > < J_{i\beta} > .
$$

The first term is called the *Van Vleck* susceptibly – which is constant at zero tem-

perature – and the second term is the *Curie* susceptibility, which diverges at low temperatures. The Eq. 2.21 is obtained by varying the effective field. It is interesting, at least from an experimental point of view, to calculate the susceptibility when the external applied field varies slightly, $\delta h_{\mathbf{q}} exp(i\mathbf{q}\cdot\mathbf{R}_i)$. Hence, according to Eq. 2.16:

$$\delta h_i^{eff} = \delta h_{\mathbf{q}}\, exp(i\mathbf{q}\cdot\mathbf{R}_i) + \sum_j \mathcal{J}_{ij}\, \overline{\overline{\chi}}^0(j)\, \delta h_j^{eff}. \qquad (2.22)$$

Assuming $\overline{\overline{\chi}}$ and $<\mathbf{J}>$ to be site independent, the susceptibility can be deduced from:

$$\overline{\overline{\chi}}(\mathbf{q}) = \left\{1 - \overline{\overline{\chi}}^0 \mathcal{J}(\mathbf{q})\right\}^{-1} \overline{\overline{\chi}}^0. \qquad (2.23)$$

If the crystal field ground state is degenerate, the second term in Eq. 2.21 is not zero and diverges at zero temperature. If B_2^0 parameter of the crystal field is negative, the z component of $\overline{\overline{\chi}}(\mathbf{q})$ is the largest component, whereas if $B_2^0 > 0$ the xy planar components are larger.

2.4 The generalized susceptibility

For analysis of the excitation spectra obtained by neutron scattering experiments, a more detailed theoretical understanding is required. In this section a brief collection of some important and related identities is presented. More comprehensive information can be found in Ref. [26]. In a scattering event the so-called *dynamic correlation function* or, in other words, the *scattering function* is being measured. It is defined as

$$S_{\mathbf{GF}}(t) \equiv\, <\mathbf{G}(t)\mathbf{F}> - <\mathbf{G}><\mathbf{F}>, \qquad (2.24)$$

where $\mathbf{G}$ and $\mathbf{F}$ are physical observables, for instance angular momentum or magnetization. Using statistical mechanics and the Heisenberg notation for the time evolution of an operator

$$\mathbf{G}(t) = e^{i\mathcal{H}t/\hbar}\mathbf{G}e^{-i\mathcal{H}t/\hbar}, \qquad (2.25)$$

one can define

$$< \mathbf{G}(t)\mathbf{F} > \quad = \quad \frac{1}{Z} Tr \left\{ e^{-\beta \mathcal{H}} e^{i\mathcal{H}t/\hbar} \mathbf{G} e^{-i\mathcal{H}t/\hbar} \mathbf{F} \right\} \tag{2.26}$$

$$= \quad \frac{1}{Z} Tr \left\{ e^{-\beta \mathcal{H}} \mathbf{FG}(t + i\beta\hbar) \right\} = < \mathbf{FG}(t + i\beta\hbar) > .$$

$\mathcal{H}$ is the Hamiltonian, Z is the partition function and $\beta = 1/k_B T$. Therefore, the relation

$$S_{\mathbf{GF}}(t) = S_{\mathbf{FG}}(-t - i\beta\hbar) \tag{2.27}$$

is satisfied. The generalized susceptibility is the response of the system to a perturbation, *i.e.* a small applied field, varying in space and time, and can be expressed by *Kubo* formula:

$$K_{\mathbf{GF}}(t) = \frac{i}{\hbar} < [\mathbf{G}(t), \mathbf{F}] > = \frac{i}{\hbar} < [\mathbf{G}, \mathbf{F}(-t)] > \tag{2.28}$$

The Fourier transform of Eq. 2.28 results in the generalized susceptibility, whose imaginary part can be simply described by

$$\chi''_{\mathbf{GF}}(z) = \frac{1}{2i} K_{\mathbf{GF}}(z), \tag{2.29}$$

where $z = \omega + i\epsilon$ is a complex number, and ϵ is a positive infinitesimal value ensuring that χ'' is an analytical function. It should be noticed that the above equation is valid under the casual assumption that the perturbation term vanishes when $t \rightarrow -\infty$. On the other hand, the relation between the correlation function and the response function follows:

$$K_{\mathbf{GF}}(t) = \frac{i}{\hbar} \left\{ S_{\mathbf{GF}}(t) - S_{\mathbf{FG}}(-t) \right\}. \tag{2.30}$$

Hence, the *fluctuation-dissipation* theorem – which connects the spontaneous fluctuations of the system to a response from a perturbation – described by the susceptibility can be extracted from Eq. 2.29 and 2.30

$$S_{\mathbf{GF}}(\omega) = 2\hbar \frac{1}{1 - e^{\beta\hbar\omega}} \chi''_{\mathbf{GF}}(\omega), \tag{2.31}$$

where $S_{\mathbf{GF}}(\omega)$ is the Fourier transform of $S_{\mathbf{GF}}(t)$.

If the eigenvalues (E_m) and eigenstates $(|m>)$ of the Hamiltonian are known, an explicit equation for $\chi_{\mathbf{FG}}(\omega)$ can be extracted according to Eq. 2.28:

$$K_{\mathbf{GF}}(t) = \frac{i}{\hbar} \sum_{m,n} <m|\mathbf{G}|n><n|\mathbf{F}|m> (N_m - N_n) e^{i(E_m - E_n)t/\hbar}. \tag{2.32}$$

N_m and N_n are the population factors of states m and n respectively, which in thermal equilibrium follow the Boltzmann distribution:

$$N_m = \frac{1}{Z} e^{-\beta E_m} \quad ; \quad Z = Tr \ e^{-\beta E_m} \tag{2.33}$$

Where, $\beta = 1/(k_B T)$. As mentioned, the frequency dependent generalized susceptibility can be calculated by the Fourier transform of the response function

$$\begin{aligned} \chi_{\mathbf{GF}}(w) &= \lim_{\epsilon \to 0^+} \int_0^\infty K_{\mathbf{GF}}(t) e^{i(w+i\epsilon)t} dt \\ &= \lim_{\epsilon \to 0^+} \sum_{m,n} \frac{<m|\mathbf{G}|n><n|\mathbf{F}|m>}{E_n - E_m - \hbar\omega - i\hbar\epsilon} (N_m - N_n) \end{aligned} \tag{2.34}$$

It should be noticed that, at zero frequency the obtained real part of the susceptibility $(\chi^0_{\mathbf{GF}})$ is similar to the results extracted by MF calculations (Eq. 2.21).

2.5   The random phase approximation

Random phase approximation (RPA) defines a simple way of investigating the *dynamics* of the system, and therefore provides a qualitative comparison with experimental observations of inelastic scattering. The scattering function measured by neutron experiments can be calculated within the framework of the two particle correlations.

Starting from the effective Hamiltonian:

$$\mathcal{H} = \sum_i \mathcal{H}_{MF}(i) - \frac{1}{2} \sum_{i \neq j} \mathcal{J}(ij)(\mathbf{J}_i - <\mathbf{J}_i>) \cdot (\mathbf{J}_j - <\mathbf{J}_j>), \qquad (2.35)$$

the first term includes the mean field sum of the single ions plus the non correlating terms. In analogy to the previous section, the aim is to calculate the linear response of the $<\mathbf{J}_i(t)>$ operator to a small perturbative field $\mathbf{h}_j(t) = g\mu_B \mathbf{H}_j(t)$. Therefore, the time-dependent effective Hamiltonian can be written as follows

$$\mathcal{H}_i(t) = \mathcal{H}_{MF}(i,t) - (\mathbf{J}_i(t) - <\mathbf{J}_i>) \cdot (\sum_j \mathcal{J}(ij)(\mathbf{J}_j(t) - <\mathbf{J}_j>) + \mathbf{h}_i(t)). \qquad (2.36)$$

At low temperatures when the fluctuations are small and in the limit of long-range interactions summing over many sites, the fluctuating terms can be neglected. Hence, $\mathbf{J}_i(t)$ could be approximated by $<\mathbf{J}_i(t)>$. This so-called *random phase approximation* is valid at $T = 0$, but when the temperature increases, thermally populated magnetic excitations with short life time interact with each other, which invalidate the approximation. According to Eq. 2.34, by introducing RPA into Eq. 2.36, $<\mathbf{J}_i(\omega)>$ (the Fourier transform of $<\mathbf{J}_i(t)> - <\mathbf{J}_i>$) can be calculated through the single ion interaction

$$
\begin{aligned}
<\mathbf{J}_i(\omega)> &= \overline{\overline{\chi}}_i^0(\omega) h_i^{eff}(\omega) \\
h_i^{eff}(\omega) &= \mathbf{h}_i(\omega) + \sum_j \mathcal{J}(i,j) <\mathbf{J}_j(\omega)>,
\end{aligned}
\qquad (2.37)
$$

which should coincide with its obtained value via the two ion interaction

$$<\mathbf{J}_i(\omega)> = \sum_j \overline{\overline{\chi}}(ij,\omega) \mathbf{h}_j(\omega) \qquad (2.38)$$

Therefore, within RPA model the self-consistent generalized susceptibility obeys

$$\overline{\overline{\chi}}(ij,\omega) = \overline{\overline{\chi}}_i^0(w)\left(\delta_{ij} + \sum_{j'} \mathcal{J}(i,j')\overline{\overline{\chi}}(j'j,\omega)\right). \tag{2.39}$$

It should be noticed that single ion susceptibility, $\overline{\overline{\chi}}_i^0(w)$ is extracted from mean field approximation. Hence, the approach mentioned above is considered as MF-RPA model.

2.6 Virtual Crystal Mean Field / RPA in LiReF$_4$

In the LiReF$_4$ structure there are 4 sites per unit cell. Therefore, 4 single ion Hamiltonians retained for MF calculation: $\sum_{i,j} \mathbf{J}_i \cdot \mathbf{J}_j \simeq \sum_{i,j} \mathbf{J}_i \cdot \langle \mathbf{J}_j \rangle$. One can re-write the Hamiltonian under MF approximation as follows:

$$\mathcal{H}_i^{\mathrm{MF}} = -\mathbf{J}_i \cdot \mathbf{H}_i + \mathcal{H}_{CF} + A\mathbf{J}_i \cdot \mathbf{I}_i - g_l \mu_B \mathbf{J}_i \cdot \mathbf{H}. \tag{2.40}$$

where i indexes the sites within the unit cell, $\mathcal{H}_{CF}$ is the crystal field, A the hyperfine coupling to the $\mathbf{I}_i$ nuclear magnetic moment, and $\mathbf{H}_i$ the site i mean field:

$$\mathbf{H}_i = \sum_{j(i)} \mathcal{J}_{ex}\langle \mathbf{J}_j \rangle + \sum_j (g_{\mathrm{L}}\mu_{\mathrm{B}})^2 \overline{\overline{D}}_{ij}(\mathbf{q}=0)\langle \mathbf{J}_j \rangle \tag{2.41}$$

with j(i) running on nearest neighbors NN. $\overline{\overline{D}}_{ij}(\mathbf{q}=0)$ is a 3 × 3 matrix defined as:

$$\overline{\overline{D}}_{ij}(\mathbf{q}=0) = \frac{N}{V}\left(\frac{4\pi}{3} + \left[\overline{\overline{D}}_{ij}(\mathbf{q}=0)\right]_{\mathrm{L}} - \overline{\overline{\mathcal{N}}}_{ij}\right) \tag{2.42}$$

where $\frac{4\pi}{3}$ is the Lorentz factor, $\left[\overline{\overline{D}}_{ij}(\mathbf{q}=0)\right]_{\mathrm{L}}$ the lattice sum of the dipole-dipole interaction and $\overline{\overline{\mathcal{N}}}_{ij}$ the demagnetization term [5]. $\overline{\overline{D}}_{ij}(\mathbf{q}=0)$ is calculated by a direct summation. To extract the Lorentz factor, the summation was split up into two terms including a sum over a sphere and an integral term from the sphere to the sample:

$$\sum_j \overline{\overline{D}}_{ij}(\mathbf{q}=0) = \sum_{sphere} \overline{\overline{D}}_{ij}(\mathbf{q}=0)(ij) + \frac{1}{V}\int_{sphere}^{sample} \frac{3\mathbf{r}_\alpha \mathbf{r}_\beta - \delta_{\alpha\beta}\mathbf{r}^2}{\mathbf{r}^5}d\mathbf{r}, \tag{2.43}$$

where V is the volume per ion in the lattice. Since there are four Re sites within the unit cell, the coupling term is:

$$\overline{\overline{\mathcal{J}}}(0) = 4\mathcal{J}_{ex} + \mathcal{J}_D, \overline{\overline{\mathcal{D}}}_{\alpha\alpha}(0). \tag{2.44}$$

Because of the small exchange interactions in LiReF$_4$, the first term is negligible. For Re=Ho the second term has been reported as [5]:

$$
\begin{aligned}
\mathcal{J}_D\overline{\overline{\mathcal{D}}}_{aa}(q=0) &= (\mu_B g)^2 N\left(-0.83225 + \frac{4\pi}{3}\right) = 3.912\ \mu eV \\
\mathcal{J}_D\overline{\overline{\mathcal{D}}}_{cc}(q=0) &= (\mu_B g)^2 N\left(1.66451 + \frac{4\pi}{3}\right) = 6.821\ \mu eV.
\end{aligned}
\tag{2.45}
$$

$N = 1.39 \cdot 10^{22}$ cm^{-3} is the number of magnetic ions per unit unit cell.

The MF Hamiltonians form 4 coupled self-consistence equations.

The numerical algorithm utilized to solve the self-consistence equations, takes a unit cell and performs the following:

1. First the mean moment $\langle \mathbf{J}_i \rangle$ within the unit cell is initialized *e.g.* to random values.

    (a) From the configuration of the given moments, the mean-fields $\mathbf{H}_i$ are computed.

    (b) The Hamiltonians $\mathcal{H}_i^{\text{MF}}$ are diagonalized and the mean moments $\langle \mathbf{J}_i \rangle$ are updated.

2. The system is then going through several loops from 1 until the change between the old mean moments and the updated ones falls below a given threshold. The algorithm always converges.

In the case of LiErF$_4$, where only 23% of naturally occurring Er nuclei carry spin, or LiHo$_x$Y$_{1-x}$ where non magnetic Y ions are substituted for Ho, simple Virtual Crystal Mean-Field (VCMF) approximation – that is widely used to solve the MF Hamiltonians of composites – is performed [27]. If one labels Ho and Y /(Er nuclei with and without

the spins) as A and B respectively, the magnetic moment operator can be written as:

$$\mathbf{J}_i = n_i \mathbf{J}_i^A \oplus (1 - n_i)\mathbf{J}_i^B, \tag{2.46}$$

where $n_i = 1$ if the (i) ion is A and $n_i = 0$ if it is B. The virtual crystal method uses a homogeneous approximation with a composite moment where $n_i = x$ with x the proportion of ions A. The composite MF Hamiltonian can be written as:

$$\mathcal{H}_{i,t}^{\mathrm{VCMF}} = \mathbf{J}_i^t \cdot \left(x\mathbf{H}_i^A + (1 - x)\mathbf{H}_i^B \right) + \mathcal{H}_{CF} + A_t \mathbf{J}_i^t \cdot \mathbf{I}_i^t \tag{2.47}$$

where t indexes A and B type ion and $\mathbf{H}_i^t$ is the site i and ion type t self-consistent mean field. The numerical algorithm is essentially as presented above, with the difference that VCMF not only mixes site-specific mean-fields, but also the ion type specific mean-fields. This mean field procedure is exactly the same as the one previously applied to LiHoF$_4$ [5]. The only difference being to replace the parameters for LiErF$_4$ as shown in Table 2.1. Crystal field parameters are compared in Table 4.1.

	g	$\mathcal{J}_{ex}(\mu eV)$	$A(\mu eV)$
LiHoF$_4$ [5]	1.25	0.1 ± 0.1	3.361
LiErF$_4$	1.2	0 ± 0.1	0.434

Table 2.1: The parameters used for mean-field calculations on LiHoF$_4$ and LiErF$_4$.

If there exist only one kind of Re ion in the system, VCMF is equivalent to the MF treatment. Fig. 2.2 depicts the T-H phase diagram obtained for LiHoF$_4$ mapped by the VCMF calculation.

The generalized susceptibility in RPA within q space, is obtained by a Fourier transformation of Eq. 2.39:

$$\bar{\bar{\chi}}(q,\omega) = \frac{1}{4}\sum_{i,j}\left[\delta_{ij}\bar{\bar{1}} - \bar{\bar{\chi}}_i^0(\omega)\cdot\bar{\bar{\mathcal{J}}}_{ij}(q)\right]^{-1}\cdot\bar{\bar{\chi}}_j^0(\omega). \tag{2.48}$$

$\bar{\bar{1}}$ is the unity matrix, and $\bar{\bar{\mathcal{J}}}_{ij}(q)$ is the Fourier transform of the coupling tensor for
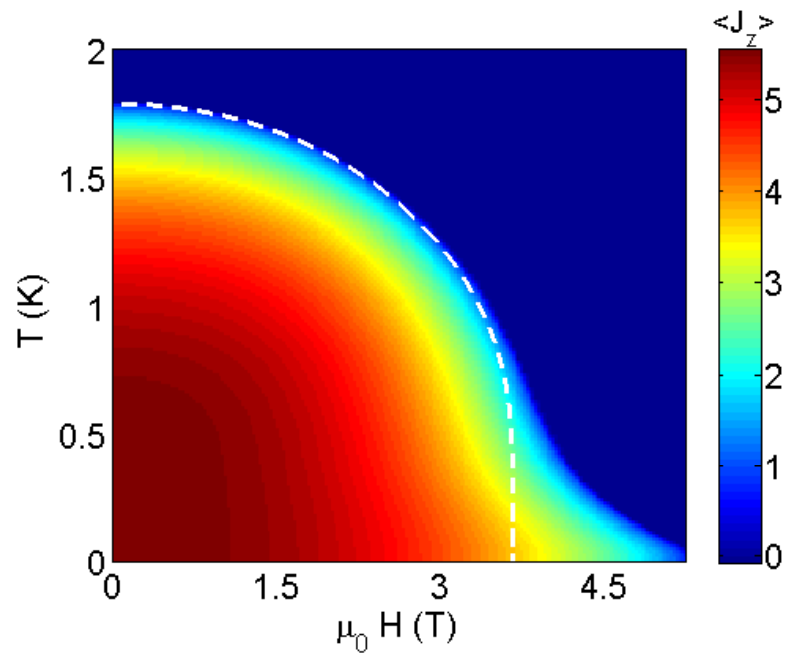
Figure 2.2: T-H phase diagram predicted by MF theory for LiHoF$_4$. The white dashed line is the calculation neglecting the hyperfine effect.

ions at sites α and β. $\overline{\overline{\chi}}_i^0$ stands for the single ion susceptibility:

$$\overline{\overline{\chi}}_i^{0,\alpha\beta}(\omega) = \lim_{\epsilon \to 0^+} \sum_{n,m} \frac{\langle n|\mathbf{J}_i^\alpha|m\rangle\langle m|\mathbf{J}_i^\beta|n\rangle}{E_m - E_n - \omega - i\epsilon}(N_n - N_m). \qquad (2.49)$$

Figure 2.3 presents the dispersion of magnetic excitations in LiErF$_4$. The comparison with experimental data – which is presented in the following chapter – exhibits the qualitatively correct prediction of RPA treatment in LiReF$_4$. However, the method has its own limitations. Overestimation of the critical temperature and critical field, and underestimation of the characteristic excitations are most probably due to the absence of fluctuations in the approximation.
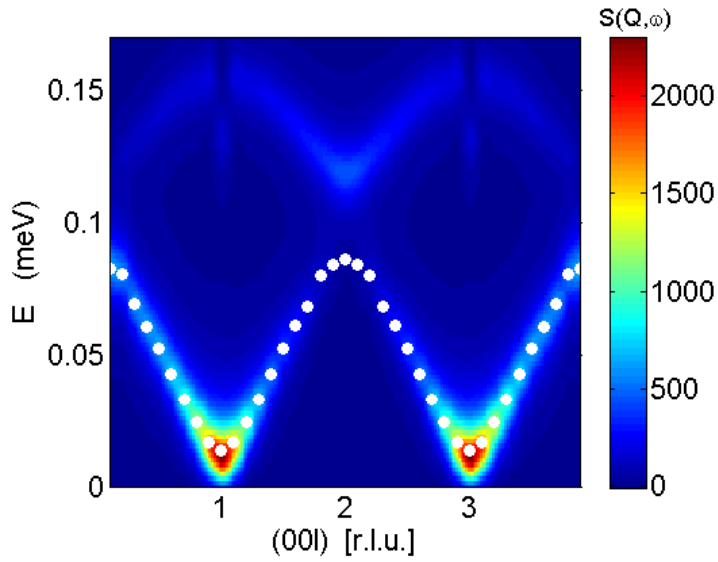
Figure 2.3: RPA prediction for the dispersion of magnetic excitations in LiErF$_4$ at H=0. The white points are the energy of the excitations obtained by the fits to a damped harmonic oscillator model.

3 Methods and Material

3.1 Methods

Most of experiments presented in this project were carried out by neutron scattering. However, a few other were used as complementary methods such as specific heat (c_p), AC-susceptibility and muon spin rotation (μSR). For a comprehensive understanding of each technique there are many available references, which some are mentioned in the following.

3.1.1 Neutron Scattering

In large scale facilities for scientific research, neutrons are produced either from fission reactors or spallation sources. Often "hot" (higher energy, shorter wavelength) or "cold" (lower energy or longer wavelengths) neutrons are needed for various studies. To obtain such distributions, neutrons are passed through moderators to obtain wavelengths similar to inter–atomic distances. Thermal neutrons have similar energies (1–100 meV) as lattice vibrations (phonons).

Since neutrons carry spin, they interact with the unpaired electron spins in the solids. On the other hand, because they are uncharged particles, they can penetrate deeply inside the materials without introducing defects. This is one of the advantages of neutron scattering comparing to for instance, X-ray technique. Neutrons interact with matter elastically or inelastically, where in the latter case the energy of the target alters through interaction process. Hence, neutrons are a powerful tool to reveal

the magnetic characteristics of the materials – through measuring time and space dependent correlation functions. For those who are not familiar with the theory of neutron scattering, the technique is explained in detail in Refs. [28, 29, 30].

Scattering cross section

The fundamental quantity, being measured by neutron scattering is the so–called cross section (σ); which is the ratio of the scattered particles in all directions per second per unit of incident flux (Ψ_0). In most experiments, the incident beam is monochromatic. That means the energy of the incoming beam (E_i) is well defined. Where, scattered neutrons with final energy between E_f and $E_f + dE_f$ are detected in a solid angle $d\Omega$. The intensity of the scattered beam can be obtained from:

$$I = \Psi_0 \frac{d^2\sigma}{d\Omega dE_f} \Delta\Omega\Delta E_f, \qquad (3.1)$$

where $\frac{d^2\sigma}{d\Omega dE_f}$ is the partial differential cross section and, since the interaction between neutrons and matter is weak, can be calculated using the combination of Fermi's Golden rule and first Born approximation, which assumes that both incident and scattered functions are plane waves:

$$\frac{d^2\sigma}{d\Omega dE_f} = \frac{k_f}{k_i} \left(\frac{m_n}{2\pi\hbar^2}\right) \sum_{\lambda_i \lambda_f} p_{\lambda_i} \left|\langle \lambda_f | V(\mathbf{Q}) | \lambda_i \rangle\right|^2 \delta\left(\hbar\omega - \left(E_i - E_f\right)\right). \qquad (3.2)$$

$\mathbf{k}_i$ (E_i) and $\mathbf{k}_f$ (E_f) are initial and final wave vectors (energy) of neutrons, respectively. $\hbar\omega_0$ is the transferred energy, $\mathbf{Q}$ is the scattering vector ($\mathbf{Q} = \mathbf{k}_i - \mathbf{k}_f$) and V the interaction potential. $|\lambda_i\rangle$ and $|\lambda_f\rangle$ stand for the initial and final states of the target. The parameter p_{λ_i} is the occupation probability for the λ_i state. There are two types of interactions between neutrons and the target:

1. **Neutron–nuclei interaction** — This interaction is not momentum dependent, because the nucleus is much smaller than the neutron wavelength. In this type of interaction, the potential depends on the isotope and the nuclear spin (if exists). This so–called Fermi pseudo–potential between a neutron at position **r**

and nuclei at distance $\mathbf{R}_j$ is:

$$\hat{\mathbf{V}}(\mathbf{r}) = \frac{2\pi\hbar^2}{m_n} \sum_j b_j \delta\left(\mathbf{r} - \mathbf{R}_j\right). \tag{3.3}$$

b_j is called scattering length and demonstrates the strength of the scattering by each atom inside the sample. This value varies from isotope to isotope and is sensitive to the direction of the nuclear spin (if present) with respect to the spin direction of the incoming beam. b_j can be a complex quantity, where its imaginary part is related to the absorption of neutrons by nucleus. However, in the majority of nuclei the imaginary part is small. Writing the delta function in the integral form for energy, and representing the position operator in time dependent Heisenberg picture, gives the master formula for nuclear scattering as:

$$\frac{d^2\sigma}{d\Omega dE_f} = \frac{k_f}{k_i} \frac{1}{2\pi\hbar} \sum_{j,j'} b_j b_{j'} \int_{-\infty}^{\infty} \langle e^{-i\hat{\mathbf{Q}}\hat{\mathbf{R}}_{j'}(0)} e^{-i\hat{\mathbf{Q}}\hat{\mathbf{R}}_j(t)} \rangle e^{-i\omega t} dt. \tag{3.4}$$

There exists a tabulated average scattering length, called b_{coh}, which is weighted over isotopes and nuclear spins. b_{coh}^2 is equal to $\overline{b_j}\,\overline{b_{j'}'}$ if $j \neq j'$, and is $\overline{b_j}^2$ if $j = j'$. Therefore, the coherent cross section would be $\sigma_{coh} = 4\pi(b_{coh})^2$. Incoherent cross section due to the fluctuations around the mean value is given by $\sigma_{inc} = 4\pi<b^2> - <b>^2 = 4\pi(b_{inc})^2$. In the case of elastic scattering, the incoherent part contributes to the background.

In a periodic structure, for the momentum transfer $\mathbf{Q} = \tau$ (τ is a reciprocal lattice vector) Bragg peaks appear in the coherent elastic part of the cross section according to the Bragg law:

$$n\lambda = 2d\sin\theta = \frac{4\pi}{|\tau|}\sin\theta \tag{3.5}$$

and the coherent differential cross section can be written as:

$$\left(\frac{d\sigma}{d\Omega}\right)_{el,coh} = N_0 \frac{(2\pi)^3}{v_0} \sum_\tau |F_\tau|^2 \delta(\mathbf{Q} - \tau) \tag{3.6}$$

N_0 is the number of unit cells, v_0 the volume of the nuclear unit cell, and $F_\tau = \sum_j \overline{b_j} e^{i\tau \cdot \mathbf{r}_j} e^{-W_j}$ the nuclear structure factor. The term e^{-W_j} is called the Debye-Waller factor related to thermal fluctuations of the lattice around its

equilibrium position.

2. **Neutron-electron interaction** — This interaction is often called *magnetic interaction* as it presents the electromagnetic relation between the neutron spin and generated magnetization from the matter with the interaction potential:

$$\hat{\mathbf{V}}_m(\mathbf{r}) = -\gamma\mu_N\hat{\sigma}\cdot\mathbf{B}(\mathbf{r}) \tag{3.7}$$

Here, $\gamma = 1.913$ is the gyromagnetic ratio of neutron, and μ_N the nuclear magneton. $\mathbf{B}(\mathbf{r})$ represents the generated magnetic field from the sample due to electronic orbital motion and their dipolar moments at position $\mathbf{r}$. Inserting magnetic pseudopotential $\hat{\mathbf{V}}_m(\mathbf{r})$ in Eq. 3.2 gives the following master formula for magnetic differential cross section in case of unpolarized beam – neglecting the orbital contribution to the magnetic moments for simplicity:

$$\frac{d^2\sigma}{d\Omega dE_f} = (\gamma r_0)^2 \frac{k_f}{k_i}F^2(\mathbf{Q})e^{-2W(\mathbf{Q})}\sum_{\alpha\beta}\left(\delta_{\alpha\beta} - \frac{\mathbf{Q}_\alpha\mathbf{Q}_\beta}{\mathbf{Q}^2}\right)S^{\alpha\beta}(\mathbf{Q},\omega), \tag{3.8}$$

where $r_0 = 0.28 \times 10^{-12}$ cm is the classical neutron radius. The magnetic scattering function $\left(S^{\alpha\beta}(\mathbf{Q},\omega)\right)$ introduces Fourier transform of the pair correlation function:

$$S^{\alpha\beta}(\mathbf{Q},\omega) = \sum_{j,j'} e^{i\mathbf{Q}(\mathbf{R}_j - \mathbf{R}_{j'})} \sum_{\lambda_i,\lambda_f} p_\lambda \langle\lambda_i|S_j{}^\alpha|\lambda_f\rangle\langle\lambda_f|S_{j'}{}^\beta|\lambda_i\rangle\delta\left(\hbar\omega - (E_i - E_f)\right). \tag{3.9}$$

Several points should be noticed in Eq. 3.8:

- The magnetic scattering cross section is proportional to the magnetic form factor $F(\mathbf{Q})$, which is related to the spatial distribution of unpaired electrons around the magnetic ions. This term decreases with increasing scattering vector ($\mathbf{Q}$).

- The polarization factor $\left(\delta_{\alpha\beta} - \frac{\mathbf{Q}_\alpha\mathbf{Q}_\beta}{\mathbf{Q}^2}\right)$ dictates neutrons to observe the components of the magnetic moments that are perpendicular to $\mathbf{Q}$. This will help to distinguish between different polarizations of the magnetic moments.

Through the fluctuation–dissipation theorem [28, 31, 32], the scattering function

is related to the imaginary part of the generalized magnetic susceptibility:

$$S^{\alpha\beta}(\mathbf{Q},\omega) = \frac{N\hbar}{\pi}\left(1 - e^{\frac{-\hbar\omega}{k_B T}}\right)^{-1}\chi''(\mathbf{Q},\omega), \tag{3.10}$$

where N is the number of magnetic ions. This is one of the elegant properties of magnetic neutron scattering, which can give comprehensive microscopic information on the magnetic systems.

In diffraction measurements, we are mostly interested in the relationship between different particles at positions j and j' in the magnetic material, where there is no energy transfer. Hence, the correlation function ($S^{\alpha\beta}(\mathbf{Q},\omega)$) is being integrated over ω and Eq. 3.9 would be simplified into terms including only the momentum transfer:

$$
\begin{aligned}
S^{\alpha\beta}(\mathbf{Q}) &= \frac{1}{2\pi}\int_{-\infty}^{\infty} S^{\alpha\beta}(\mathbf{Q},\omega)\,d\omega \\
&= \sum_{j,j'} e^{i\mathbf{Q}(\mathbf{R}_j - \mathbf{R}_{j'})}\left(\langle S_j^{\alpha}\rangle\langle S_{j'}^{\beta}\rangle + \left\langle (S_j^{\alpha} - \langle S_j^{\alpha}\rangle)(S_{j'}^{\beta} - \langle S_{j'}^{\beta}\rangle)\right\rangle\right)
\end{aligned}
\tag{3.11}
$$

The first term is related to the Bragg scattering, whereas the second term inherits the spin correlations of the scattering material. Diffuse scattering gains importance close to the critical regime, where the correlation length studies are considered.

Elastic magnetic cross section in a long range ordered magnetic probe reads:

$$\left(\frac{d\sigma}{d\Omega}\right)_{el,mag} = (\gamma r_0)^2 N_m \frac{(2\pi)^3}{v_m}\sum_{\tau_m}\delta(\mathbf{Q} - \tau_m)|\hat{\mathbf{Q}} \times \left(F_M(\mathbf{Q}) \times \hat{\mathbf{Q}}\right)|^2. \tag{3.12}$$

Magnetic reflections appear at $\mathbf{Q} = \tau_m$, and $F_M(\mathbf{Q})$ is the magnetic structure factor:

$$F_M(\mathbf{Q}) = \sum_j \left(\frac{g_j F_j(\mathbf{Q})}{2}\right)\langle S_j\rangle\, e^{-W_j(\mathbf{Q})} \tag{3.13}$$

Neutron scattering facilities

There are two ways of producing neutrons at research facilities. At the reactor based sources, neutrons are mostly obtained via fission of U^{235} by thermal neutrons. During this procedure, energy and neutrons are released. The produced neutrons then are

guided to the instruments through shielding. An alternative way is to bombard a target of some heavy elements with highly accelerated particles, which results in many particles' creation, including neutrons. The second strategy is called "spallation". After production, the high energy neutrons are passed through so–called moderators to reach the desired energy ranges. The outcome is a scattered beam with a broad distribution of energies. Therefore, the beam needs to be monochromatized and collimated to the required energy and direction. In reality, these constrains are relaxed in order to obtain sufficient statistics, which means there is always a finite distribution in both divergence and energy. Due to this fact, the measured intensity at the experiments is the scattering cross section folded with the instrumental resolution:

$$I(\mathbf{Q}_0, \omega_0) = \int R(\mathbf{Q}_0, \omega_0; \mathbf{Q}_0 - \mathbf{Q}, \omega_0 - \omega) \cdot \left(\frac{d^2\sigma}{d\Omega dE_f} \right)_{\mathbf{Q}, \omega} d\mathbf{Q} d\omega. \qquad (3.14)$$

$R_0 = \int R(\mathbf{Q}_0, \omega_0; \mathbf{Q}_0 - \mathbf{Q}, \omega_0 - \omega) d\mathbf{Q} d\omega$ determines the probability of detecting neutrons within $\Delta\mathbf{Q}$ and $\Delta\omega$ away from $\mathbf{Q}_0$, ω_0.

Neutron scattering techniques

Neutron scattering is a wide and versatile field depending on the subject of study. In the following some of the techniques used in this project are explained briefly:

The triple–axis spectroscopy (TAS)

The triple–axis spectrometer is probably the most versatile apparatus among other neutron instruments [33]. In this technique, one can determine the energy/wavevector of the incoming (E_i/$\mathbf{k}_i$) and outgoing (E_f/$\mathbf{k}_f$) beam by inserting the "monochromators" and "analyzers" before and after the sample. Monochromators and analyzers are in principle well defined crystals with d spacing between the reflecting planes at the angle θ, satisfying the Bragg condition for the neutrons traveling with the wavelength of $\lambda = 2d \sin\theta$. The scattered neutrons leave the crystals at an angle of 2θ with respect to the incoming beam. During this procedure, an energy selection of $E = \frac{h^2}{2m\lambda^2}$ is performed. Due to the beam divergence and the mosaicity of the crystals, the energy selection is never perfect, and it is in fact distributed around a mean value. In

order to reduce the beam divergence, "collimators", which are a collection of neutron absorbing sheets, are used at several places in the path. It should be noticed that tight collimation reduces the statistics. Hence, an optimum configuration which satisfies the resolution to intensity ratio is usually desired. Fig. 3.1 represents a schematic diagram of a triple–axis spectrometer. Since monochromatizer and analyzer crystals and the sample each have an axis of rotation, the instrument is called a triple-axis spectrometer. Neutrons with wavevector $\mathbf{k}_i$ scattered from the monochromator interact elastically or inelastically with the sample, where from the later process they might gain or lose energy. The desired outgoing energy will be selected by the analyzer and finally reach to the detector. Hence, TAS is ideally suited to study a selected $(\mathbf{Q}, \omega)$ in phase space:

$$\mathbf{Q} = \mathbf{k}_i - \mathbf{k}_f \tag{3.15}$$

$$\hbar\omega = \frac{\hbar^2}{2m_n} \left(k_i{}^2 - k_f{}^2 \right) \tag{3.16}$$

Therefore, each desired point in $(\mathbf{Q}, \omega)$ space introduces a specified orientation to the monochromator, sample and analyzer. An advanced sample environment usually is available at TAS facilities, providing the high magnetic field and dilution temperature studies.
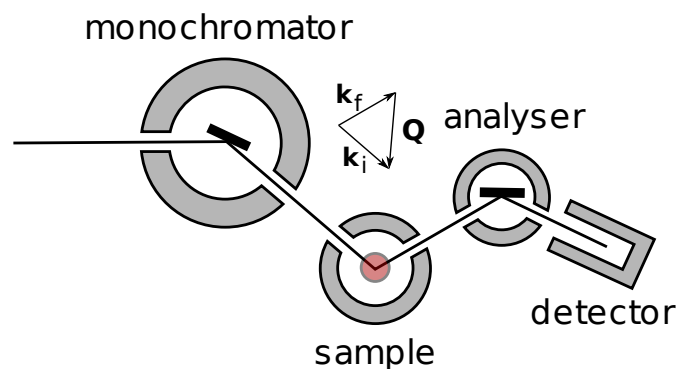

Figure 3.1: Schematic drawing of a triple-axis spectrometer. The scattering triangle is shown in the inset.

Time of flight spectroscopy (TOF)

The time of flight (TOF) technique complements the TAS method. Due to the presence of many detectors – which simultaneously collect neutrons over a wide solid angle – TOF instruments are very useful to explore a rather large area in $(\mathbf{Q}, \omega)$–space. The method is specifically useful at pulsed spallation sources, where neutrons are produced in well defined time pulses. The reactor–based facilities can also provide TOF instruments via chopping the incoming flux into pulses with the desired intervals. By knowing the travel time of neutrons to the detector, the velocity and therefore the energy transfer/gain during scattering process can be calculated. In contrary to the TAS method, where both incident and outgoing energies are selected, at TOF instruments there is just one energy constraint, either at the incident beam shining at the sample (*direct geometry*) or at the outgoing beam (*indirect geometry*). The energy filtering is performed through several choppers, and sometimes monochromator crystals are placed in the path of neutrons. The advantage of the TOF technique is the fast and parallel data acquisition within relatively large region in reciprocal space, recorded simultaneously by detector banks. Fig. 3.2 presents a schematic diagram of the LET multi-chopper direct geometry time of flight instrument at ISIS, where most of inelastic results presented in this thesis have been obtained from. Neutrons travel the distance of 25 m from the moderator to the sample within a straight super-mirror guide. There exist 5 choppers in the path to allow moderator pulse shaping, contaminant removal, pulse removal and fast time slicing of the incident neutrons. The latest, which can be rotated up to 300 Hz, produce energy resolution of about $\frac{\delta E}{E_i} \simeq 0.8\%$. The sample is placed in a 110 m^3 vacuum tank, 3.5 m away from the detectors, which are 4 m long position sensitive detectors. High incident neutron flux together with wide accessible range of $0.6 - 20 \; meV$, result in a unique setup to study low energy dynamics. Fig. 3.3 presents the position of the magnetic reflections in LiErF$_4$ within the white beam on the detector banks of LET.

Neutron diffraction

In principle, the neutron diffraction technique is very close to the TAS method, but the third axis of rotation at the analyzer is removed. Hence, the scattered beam from the
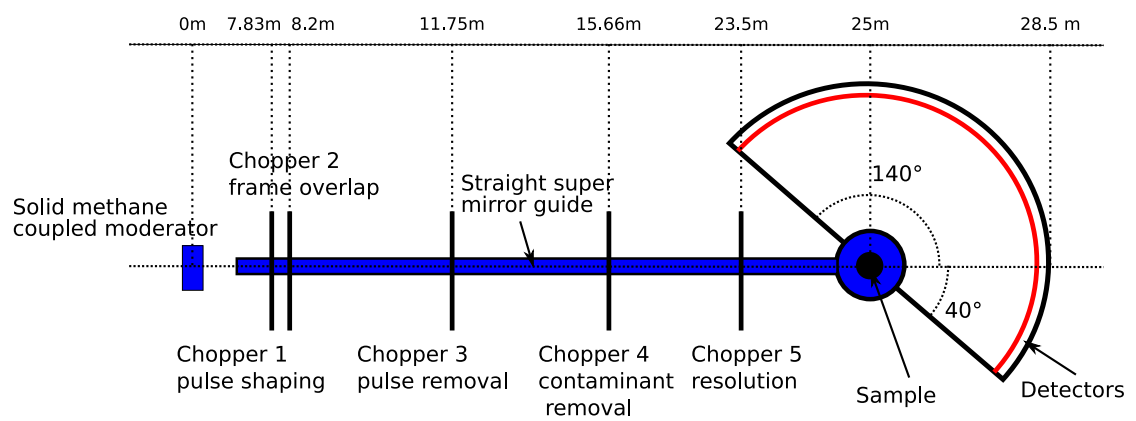
Figure 3.2: Schematic drawing of the LET time of flight spectrometer at ISIS. The figure is reproduced from [34].
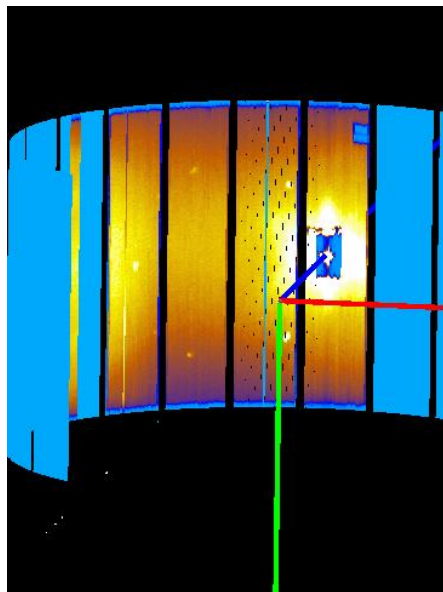

Figure 3.3: The position of the magnetic reflections in a white beam on the detector banks of LET.

sample is directly collected in the detector. In the present work, most of the diffraction measurements are performed for the purpose of order parameter investigations on the single crystals. Since no analyzer is placed after the sample, the **Q** resolution and signal-to-background ratio are not perfect in diffraction. Therefore, materials having weak and broad diffraction signals *eg.* diffuse scattering should be measured on TAS.

Backscattering spectroscopy

Very high energy resolutions (in the order of μeV) are achieved via backscattering technique. The monochromatizer and analyzer crystals (usually out of Silicon crystals) are made with the least possible mosaicity, each with fixed Bragg angle of $\sim 90°$.

$$\frac{\Delta\lambda}{\lambda} = \frac{\Delta d}{d} + \cot\theta\Delta\theta, \tag{3.17}$$

where $\Delta\theta$ is the beam divergence. The angular dependence vanishes when $\theta \to 0$. Under such condition the Bragg–reflected wavelength band ($\Delta\lambda$), and therefore ΔE becomes very narrow. In backscattering measurements, since the scans in energy are not possible – as the angle of the crystals are fixed – usually the energy can be tuned by a doppler drive attached to the monochromator. Energy scans can be also performed by varying the temperature of the crystals, so changing the lattice spacing while keeping the same scattering angle. The price for such high energy resolution is the relatively poor **Q** resolution and low flux at the sample position. On the other hand, the method is particularly efficient to study the very low energy excitations, and incoherent scattering. Fig. 3.4 demonstrates the SPHERES backscatterometer at FRMII, where an experiment in this project was performed.

3.1.2 Complementary measurements

Available laboratory facilities, for instance magnetometers (DC/AC) and specific heat c_p setups provide the first insight on bulk characterization, and their information is complementary and essential for further studies at large scale facilities for microscopic investigations.

The **heat capacity** of a system is directly connected to the entropy. In classical defi-
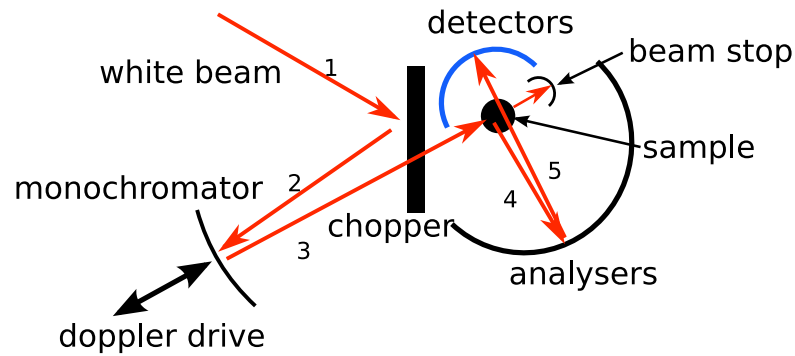
Figure 3.4: Schematic drawing of SPHERES backscatterometer at FRMII.

nition it is described by $\frac{\Delta Q}{\delta T}$ (ΔQ and δT, being heat transfer and the corresponding temperature change, respectively). C_p measurements reveal many information about the lattice and electronic structure of materials. In addition, the c_p technique is very useful to study phase transitions. An appropriate way to measure small samples with relatively poor thermal conductivity, which is the case in LiReF$_4$ family, is called time–constant or relaxation–method. Here, c_p is determined as:

$$c_p = K\tau, \tag{3.18}$$

where K is the thermal conductivity of the supporting wires and τ is the time constant:

$$T = T_0 + \Delta T e^{\frac{-t}{\tau}} \tag{3.19}$$

In the relaxation method, a small heat pulse (ΔQ) transfers to the object in a certain time period. Therefore, the temperature of the system alters slightly (ΔT) from the equilibrated bath temperature (T_0). The heater is turned off afterwards and the temperature relaxes exponentially, going back to T_0. The heat capacity (c_p) of the system is then calculated for each temperature interval. More information about the heat capacity measurements are provided in Refs. [35, 36].

AC-susceptibility measurements reveal the frequency dependance of the systems relaxation, particularly when spin glass materials and dynamics are under investigation. The technique is sensitive to the magnetic response to an applied oscillating

field. In this work the AC-susceptibility measurements performed with the help of three coils on on top of the other. The outermost one is called *primary coil*, and the two inner ones are *secondary coils*. The *secondary coils* are connected in such a way that the generated signal inside them from the *primary coil* cancels out. Therefore, they should give zero response when there is no sample. On the other hand, when a sample is inserted inside one of them, due to a different filling factor of the two coils, they exhibit different current. Hence, the outcome read by the *lock–in amplifier* is the response of the sample.

Muon spin rotation/relaxation Muons can be used as microscopic probes to investigate interesting phenomena in condensed matter physics, including magnetism. In the presence of internal local magnetic fields, muons' precession and relaxation reveals information about the static and dynamic characteristics of the system they are implanted into. Since the muon beam is 100% polarized, the experiments can be performed even in zero field. Nevertheless, measurements in the presence of static or oscillating external fields – where the field direction can be parallel or perpendicular to the muons' polarization – are also possible. In μSR facilities the produced pions from proton–target collision, decay into muons and neutrinos:

$$\pi^+ = \mu^+ + \nu \tag{3.20}$$

Pions have no spin. Therefore, muon and neutrino spins are opposite and are antiparallel to muon's and neutrino's momentum, respectively. As a consequence, a 100% polarized muon beam is produced by pions implantation inside the target. Penetration depth of muons inside the matter is few μm. After the production, muons decay to positrons (e^+) and neutrinos. Positrons are the only detectable particles in μSR experiments and are mostly emitted along the muon spin's direction. The probability of positron emission within the angle θ to the spin direction is approximately:

$$W^+(\theta, \epsilon) \propto 1 + a\cos\theta, \tag{3.21}$$

a is a constant which depends on the energy of the emitted positron. In the muon experiments where millions of muons are implanted into the sample, the quantity called *asymmetry* which contains information of the records on the forward–backward

detectors is of interest:

$$A = \frac{n_f(t) - n_b(t)}{n_f(t) + n_b(t)}. \tag{3.22}$$

n_f and n_b are the number of the positrons on the forward and backward detectors, respectively. Hence, detected positrons give information about the polarization of precessing muons inside the material. Through the time–evolution analysis of the muon polarization, a distribution of local static fields and/or dynamics related to the fluctuation fields are tractable.

In the presence of a field perpendicular to the initial muon spins ($H_\perp$), muons precess at $\omega_\mu = \gamma_\mu H$ angular frequency, where $\gamma_\mu = 85.1 \ kHz \ G^{-1}$ is the muon gyromagnetic ratio. On the other hand, a longitudinal field allows to probe spin relaxation due to the probable inhomogeneous internal field distribution. The local field is mostly produced by dipolar interactions with neighboring electronic and nuclear spins. The so-called *Kubo-Toyabe* function is usually used to analyze the zero field and longitudinal field measurements. Within this approximation, the probability distribution of the internal field components is defined by a Gaussian function of width Δ/γ_μ . Assuming the initial beam in $\hat{z}$–direction, 1/3 of muons sense a field along $\hat{z}$. Averaging the three components over the Gaussian distributions, the *Kubo-Toyabe* relaxation function is given by [37]:

$$G^{KT} = \frac{1}{3} + \frac{2}{3}(1 - \Delta^2 t^2) \ exp(-\frac{1}{2}\Delta^2 t^2). \tag{3.23}$$

At longer times, the function reaches back to the 1/3 average along the initial polarization. Longitudinal applied fields ($H_\parallel$) enhance the effect of internal fields. Therefore, the long term 1/3 tail increases to higher values.

If the internal field fluctuates, the change in the local field direction with frequency of v in a time t is predicted to obey the probability distribution $p(t) = e^{-vt}$. The randomly selected field obeying the probability function usually has a Gaussian distribution. In the fast fluctuation limit, the *dynamic Kubo-Toyabe* results:

$$G^{DKT}(t,v) = exp(\frac{-2\Delta^2 t}{v}) = exp(-\lambda t). \tag{3.24}$$

There remains no 1/3 tail within this limit. On the other hand, the intermediate fluctuating regime can be studied by a series of exponential functions. In the slow fluctuation case the effect is more obvious on the 1/3 tail which shifts to lower values in zero field, or higher values in the presence of a longitudinal field.

3.2 The LiReF$_4$ system

The LiReF$_4$ family, where Re is a rare earth ion, provides a series of compounds that are interesting both from experimental and theoretical point of view. These structures have a practical use as efficient laser materials (Chick and Naiman 1972) and can be used for frequency conversion in the infrared-visible region (Watts and Holton 1971). This group of compounds crystalize in the tetragonal Scheelite structure $I4_1/a$ (Thoma *et.al* 1961), where there are four rare earth ions per unit cell at magnetically equivalent sites, having the high point group symmetry S_4. The unit cell is shown in Fig. 3.5, and complete crystallographic details are presented in *International Tables for Crystallography* [38]. The symmetries are rather simple and crystal field models can be compared with measurements (*i.e.* susceptibility, neutron diffraction, electron paramagnetic resonance (EPR)). From various low temperature investigations [13, 39, 40], the couplings between the rare earth ions are known to be predominated by the anisotropic long-range dipole–dipole interaction of the rare earth electronic magnetic moments.

Several ingredients make this family very suited for studies:

- In these compounds, the crystal field level scheme gives effective low energy models of specific spin dimensionality such as Ising for Re=Ho, Tb; and XY planar in the case of *eg.* Re=Er, Dy.

- Albeit the dominant interaction is dipolar, which is fundamental in magnetic systems, there have not been comprehensive expanded studies on this system, except for LiHoF$_4$. Therefore, many theoretical investigations are still untested.

- The ability to dilute the rare earth sites with nonmagnetic ions like Yttrium (Y), where the structure survives without a major change except for slight differences in the lattice constants, opens an arena to explore disorder and randomness effects [3].

The materials are electrical insulators, and optically transparent. The large single crystals of LiReF$_4$ are available commercially. In addition, compounds with desired isotopes can be synthesized in laboratories.
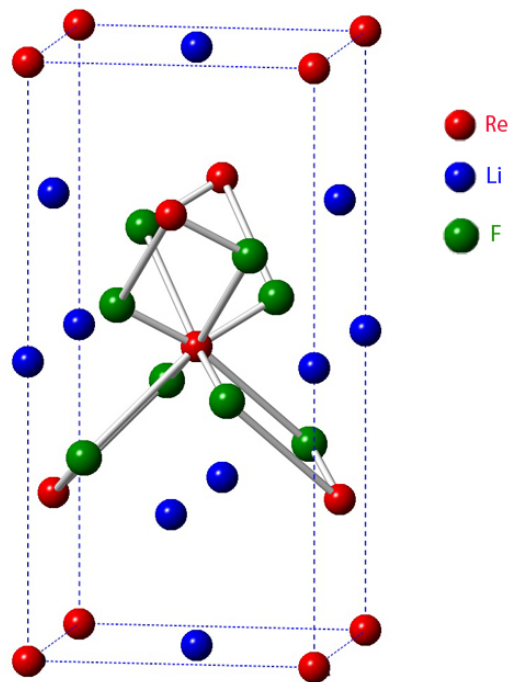
Figure 3.5: LiReF$_4$ unit cell. For better visualization the fluorine ions are only shown around the central Re atom.

The core of this research project is LiErF$_4$, a representation of the dipolar coupled planar antiferromagnet (AFM). In addition, a brief study on the phase diagram of LiHo$_x$Y$_{1-x}$F$_4$ (0.25 ≤ x ≤ 1) was performed, where the experimental results are compared to MF predictions.

3.2.1 Sample preparation

In experimental physics the sample preparation is very important. In single crystal experiments when a magnetic field along a specific crystallographic axis is required, the sample alignment is crucial, since slight misalignment can sometimes obscure the real physics. The simple tetragonal crystallographic structure of LiReF$_4$ family results in quick and relatively accurate alignment of the single crystals with the laboratory X-ray Laue diffraction camera. Nevertheless, for the special cases when less than 1 degree accuracy in alignment is required, the usual *2-axis* neutron diffractometers are suggested. In addition, since rare-earth fluorides have low thermal conductivity, they might have thermalization issue below 1K. A correct sample temperature is essential

for studying *i.e.* order parameter or specific heat, where accurate critical exponent extraction is desired. In this project, the strategy used to improve the thermalization was to cut the big crystals into thin blades of 1-1.2 mm. The blades were then sputtered by few μm of gold, and squeezed together with copper foils between them inside a gold covered sample holder made of copper. This way, waiting time for thermalization reduced by almost a factor of 6 close to the transition temperature, where the heat capacity diverges.
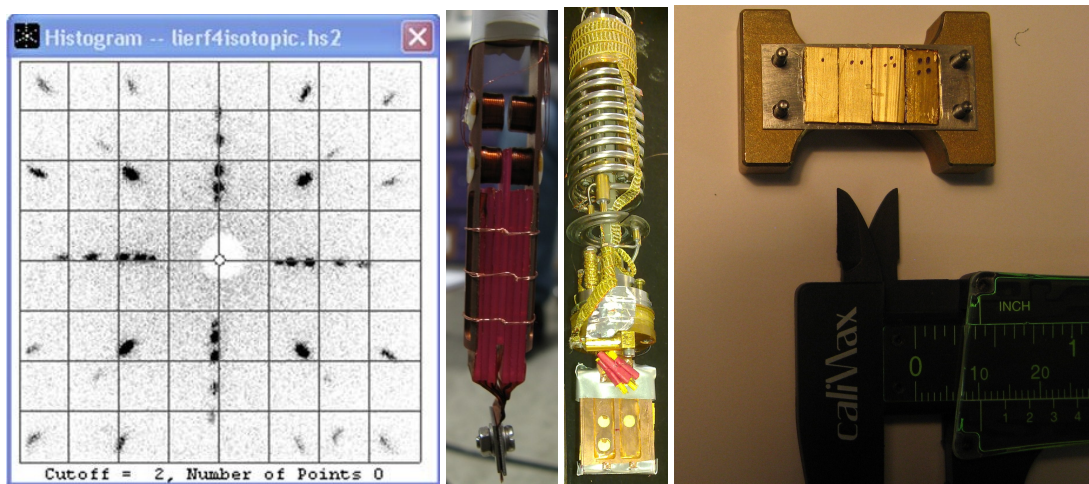

Figure 3.6: Selection of some images presenting initial sample preparations for the experiments. From left to right: A typical Laue image from the tetragonal structure of LiReF$_4$ – *a,b* are in the scattering plane. An example presenting the LiReF$_4$ blades inside a sample holder made of copper, Two LiErF$_4$ gold sputtered plates with *a,c* in-plane for LET experiment at ISIS, Setup for the μSR experiment on LTF at SINQ. Crystallographic *c*–axis is perpendicular to the big flat surface of the crystals.

3.2.2   Optimal sample thickness for neutron experiments

For the neutron experiments it is important to calculate the optimum sample diameter, which gives the best signal. Considering a rather high absorption cross sections in rare earths –particularly in Re=Er, Ho in this work – a diameter estimation helps when weak inelastic signals at low energy scales are under investigation. Scattered intensity is proportional to the sample diameter squared, and transmission is related to the absorption coefficient. Hence, the maximum signal is obtained when $d^2\,e^{(-\mu d)}$ is maximum, where μ is the attenuation factor. For a given composition μ

can be computed through http://www.ncnr.nist.gov/instruments/bt1/neutron.html, supported by NIST Center for Neutron Research. Fig. 3.7 presents an example of a calculation on LiErF$_4$ and LiHoF$_4$ to choose the proper sample diameter for the neutron backscattering experiment at SPHERES/FRMII.
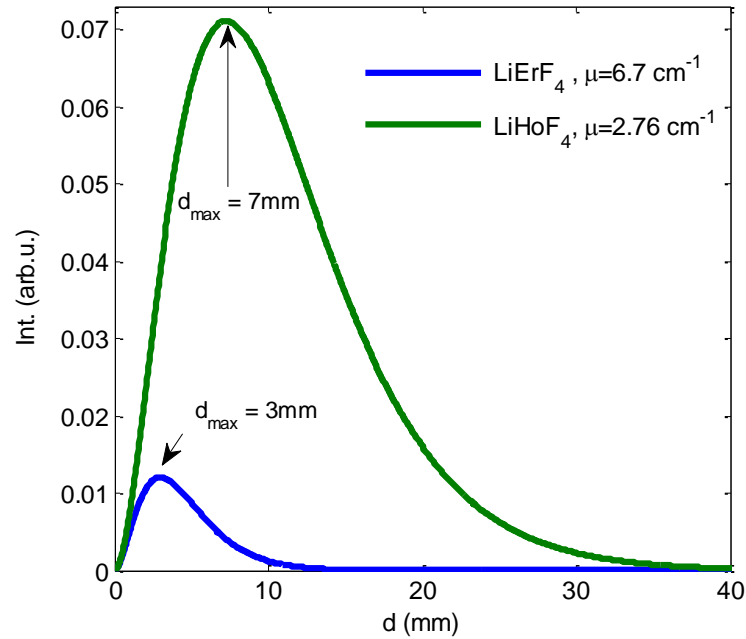

Figure 3.7: Optimal sample diameter calculation for back scattering experiment on LiErF$_4$ and LiHoF$_4$ with $\lambda = 6.271$Å.

3.2.3 Sample environment

The measurements on LiReF$_4$ was performed at dilution temperatures and in magnetic fields. The magnetic field direction was usually perpendicular to the scattering plane, although in some cases horizontal magnet was utilized. – The majority of neutron experiments were performed with *split-pair solenoid superconducting magnets,* where the windings are symmetric but split into two parts in an axial direction with a gap in between. The solenoids are mainly produced from superconducting Niobium-Titanium (NbTi) commercial superconductors, which can carry large currents. There are several compromises building such magnets to produce homogenous flux and leave enough space for the beam access. The required window transparent to neutrons is usually made of aluminium rings between the two splits or wedge shaped openings

between the solenoids. The maximum field produced by split–pair coils is about 15T.
– Studies of quantum criticality at low energy scales require temperatures close to
zero, where thermal fluctuations are negligible. Temperatures down to ~ 20 mK are
achievable with dilution refrigerators. Below ≃ 0.86 K, the mixture undergoes a phase
separation to produce a ^{3}He–rich phase and ^{3}He–poor phase in the so–called *mixing
chamber* – to which the sample is attached through pure copper rod ensuring good
thermal anchoring. The cooling power is provided by pumping ^{3}He from ^{3}He–rich
phase to ^{3}He-poor phase. Continuous operation is achieved via circulating flow of ^{3}He
from the diluted regime to the concentrated phase. The apparatus is rather complex
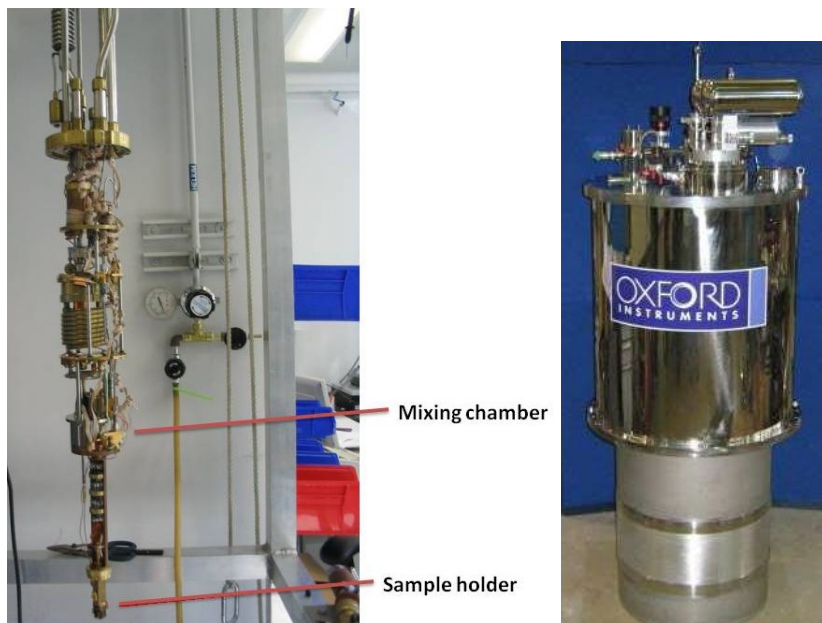and more information can be found in Ref. [41].

Figure 3.8: Left: A representative image of a dilution stick. The figure is adapted from
[41]. Right: 9T cryomagnet at ISIS.

4 LiErF$_4$ – a novel planar dipolar antiferromagnet (AFM)

The dipolar force between magnetic moments is present in all magnetic systems, from classical to quantum magnets, from bulk materials to nano–particles. However, while there exist many studies of systems with short range forces, like the exchange-coupled Heisenberg antiferromagnet RbMnF$_3$, the dipolar-coupled systems, especially antiferromagnetic (AFM) ones, have received less attention mainly due to a lack of physical realizations. An excellent subject to test the physics of dipolar-coupled systems are the rare earth (*Re*) lithium tetrafluorides, Li*Re*F$_4$, where the tightly bound $4f$ electrons are far enough apart for the dipolar interactions to dominate exchange interactions. In this chapter, the experimental results on the magnetic order, the classical and quantum phase transitions, excitations, magnetic correlations and fluctuations about the critical points for LiErF$_4$, an antiferromagnetic (AFM) member of the LiReF$_4$ family, are presented. The structure is organized as follows:

- The existing information and previous studies on the LiErF$_4$ system are summarized in the introduction.

The results obtained from this work are:

- The specific heat measurements presented in 4.2.
- AC-susceptibility measurements of both natural and isotopic samples presented in 4.3.
- Order parameter studies of natural and isotopic samples of LiErF$_4$ shown in 4.4.
- Complementary techniques to study order parameter presented in 4.5.

- Critical scattering and correlation length measurements in the vicinity of the phase transitions shown in 4.6.
- Excitations and dynamics modeled by MF/RPA presented in 4.7.

4.1 Introduction

Two members of the LiReF$_4$ family, LiHoF$_4$ and LiTbF$_4$ – with magnetic orderings at 1.53 K and 2.87 K, respectively – owing uniaxial dipolar ferromagnetism due to a large effective g–factor along the local symmetry ($g_\parallel$) while the planar factor ($g_\perp$) is almost zero, have been mostly considered [15]. Their low temperature ferromagnetic ordering is in agreement with the predictions [42] obtained by generalization of Luttinger-Tisza theory ([43]). Hansen *et. al* studied the magnetic susceptibility of the LiErF$_4$ compound in the range of $1.3 - 300$ K, where no transition to a magnetically ordered state was observed due to not having access to lower temperatures [13]. Nevertheless, they found the largest susceptibility along the crystallographic a axis, with $\frac{\chi_a}{\chi_c} \simeq 2$ in the $10 - 300$ K temperature range. The slope of the inverse (reciprocal) susceptibility versus temperature ($d\chi^{-1}/dT = 1/C$) was the same for both in-plane and out-of-plane components all the way down to 10 K, where below that $1/C_c = 110$ g/cm^3 K and $1/C_a = 36$ g/cm^3 K (C is the *Curie* constant). Furthermore, magnetic susceptibility measurements from Beauvillain *et.al* at ^{3}He temperature could reveal a transition in LiErF$_4$ at 0.38 K [14], with $g_\parallel/g_\perp \approx 0.39$. EPR studies by Magariño *et.al.* provided more information, proving the XY nature of LiErF$_4$ magnetic moments, and a planar anisotropy with the periodicity of 90° [17].

The above statements confirm the lack of existing information on LiErF$_4$ until 2009, when the magnetic structure and the nature of the phase transitions were determined for the first time via neutron diffraction studies [19]. The Hamiltonian magnetic model for LiReF$_4$ contains crystal field, external field and hyperfine coupling to the nuclear spins, as well as dipolar and exchange interactions (eq.2.3):

$$\mathcal{H} = \sum_i \left[\mathcal{H}_{cf}(\mathbf{J}_i) - g\mu_B \mathbf{J}_i \cdot \mathbf{H} + A\mathbf{J}_i \cdot \mathbf{I}_i \right] \tag{4.1}$$

$$-\frac{1}{2}\sum_{ij}\sum_{\alpha\beta}\mathcal{J}_D D_{ij}^{\alpha\beta} J_{i\alpha}J_{j\beta} - \frac{1}{2}\sum_{ij,n.n.}\mathcal{J}_{ex}\mathbf{J}_i \cdot \mathbf{J}_j$$

The dipole interaction follows the classical dipole tensor:

$$D_{ij}^{\alpha\beta} = \frac{3(\mathbf{r}_{i\alpha} - \mathbf{r}_{j\alpha})(\mathbf{r}_{i\beta} - \mathbf{r}_{j\beta}) - |\mathbf{r}_i - \mathbf{r}_j|^2\delta_{\alpha\beta}}{|\mathbf{r}_i - \mathbf{r}_j|^5}. \tag{4.2}$$

Its peculiar spatial anisotropy is illustrated in Fig.4.1. In LiHoF$_4$, the moments point along z, and nearest neighbors (NN) are coupled ferromagnetically. In LiErF$_4$, half the NN couplings are AFM, the other half FM, and rotating the moments by 90 degrees switches between FM and AFM interactions. In LiHoF$_4$ the exchange interaction is small [5], which given the similar wavefunctions for Ho and Er, is also expected for LiErF$_4$. The hyperfine coupling $A = 0.5(1)$ μeV for ^{167}Er [44] is weaker than in LiHoF$_4$ [5] and, importantly, is tunable. The ground state of Er^{3+} is $4f^{11}$, and based on Hunds' rules have the $^4I_{15/2}$ configuration . The first excited state lies at about 2.2 meV above the ground state doublet [19]. Therefore, at low temperatures the state mixing is negligible.

An effective Hamiltonian for low temperature studies can be written as:

$$\mathcal{H}_{eff} = \sum_{ij\alpha\beta}\mathcal{J}_{ij}^{\alpha\beta}\sigma_i^\alpha\sigma_j^\beta + g_\perp(\sigma_i^x B^x + \sigma_i^y B^y) + g_\parallel \sigma_i^z B^z, \tag{4.3}$$

where σ_i denotes the Pauli operators, and $\mathcal{J}_{ij}^{\alpha\beta} = (\mu_B\ g)^2 C_\alpha C_\beta D_{ij}^{\alpha\beta}$ the magnetic coupling tensor between the effective $S = 1/2$ spins $S^\alpha = C_\alpha\sigma^\alpha$ with $C_x = C_y = 3.48$, $C_z = 0.94$, calculated by the crystal field refinement. $g_\perp = 2gC_x = 8.35$ and $g_\parallel = 2gC_z = 2.25$, which directly reflect the pronounced XY-anisotropy of the system.

The electric field from neighboring ions act differently on the orbital wave-functions, and, restricted by the local symmetry, gives

$$\mathcal{H}_{cf} = \sum_{l=2,4,6} B_l^0\mathbf{O}_l^0 + \sum_{l=4,6} B_l^4(c)\mathbf{O}_l^4(c) + B_6^4(s)\mathbf{O}_6^4(s), \tag{4.4}$$

where $\mathbf{O}_l^m$ are the Stevens operators [45], with *e.g.* $\mathbf{O}_2^0 = 3\mathbf{J}_z^2 - \mathbf{J}(\mathbf{J}+1)$. In LiHoF$_4$, a

dominant negative B_2^0 leads to a strong z-axis Ising anisotropy, while a positive B_2^0 leads to planar XY anisotropy in LiErF$_4$.
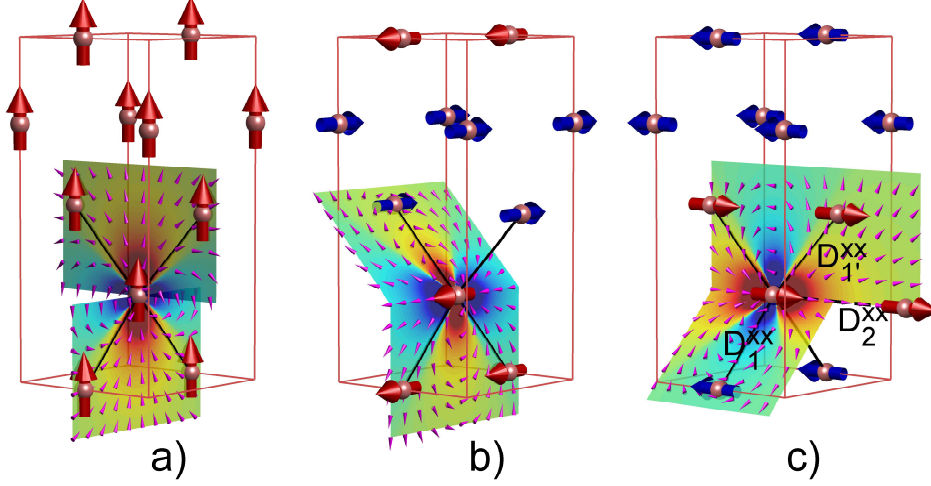

Figure 4.1: Magnetic structures of LiReF$_4$: The ferromagnetic c-axis order in LiHoF$_4$, and bi-layered antiferromagnetic (BLAFM) order with moments along x- or y-axis in LiErF$_4$. The dipole field from the central moment yields FM (red-scale) and AFM (blue-scale) couplings. Sign and strengths of the coupling depend on the direction of the moments. In the BLAFM structure, nearest and next-nearest couplings are $\nu D_1^{xx} = -5.5$ (AFM), $\nu D_{1'}^{xx} = 2.5$ (FM) and $\nu D_2^{xx} = 4.2$, $\nu = a^2 c$. The crystal structure is tetragonal, space group I4$_1$/a with $a = b = 5.162$Å and $c = 10.70$Å.

A detailed and comprehensive crystal field study is performed in [19], where the full set of cf parameters, obtained through neutron spectroscopy, is presented. Tables 4.1 and 4.2 represent the obtained cf parameters and energy levels of LiErF$_4$ from neutron scattering compared to the previous studies.

The magnetic structure was determined by single-crystal and powder neutron diffraction [19]. Magnetic Bragg peaks at ($h + k + l =$odd), distinct from the structural peaks ($h + k + l =$even), proved explicitly antiferromagnetic order. Intensity inspection lead to the bilayered antiferromagnetic (BLAFM) structure, which was verified by powder diffraction. The BLAFM has 2 equivalent configurations with moments along the a-axis or b-axis, respectively. A very small field of 300 Oe along the b-axis suppressed the (100) reflection, thus populating a single a-axis domain. Hence, the zero-field structure is a distribution of spatially separated domains with moments along the

	$10^3 B_2^0$	$10^3 B_4^0$	$10^3 B_4^4(c)$	$10^5 B_6^0$	$10^6 B_6^4(c)$	$10^6 B_6^4(s)$
neutron	60.2258	-0.1164	-4.3280	-0.19	-85	-22.7
pointcharge [19]	26.9	-0.12	-1.74	-0.04	-11.5	-2.4
Ref. [13]	67.7	-0.68	-6.82	-0.08	-133.0	-24.3
LiHoF$_4$ [5]	-60.0	0.35	3.6	0.04	70	9.8

Table 4.1: Crystal field parameters of LiErF$_4$ in meV. The parameters refined from inelastic neutron scattering are compared to a point-charge calculation and values found in literature [13].

measured	calculated	Ref. [17]	Ref. [13]	Ref. [24]
2.23 ± 0.05	2.23	2.30	2.30	2.20
3.52 ± 0.05	3.52	2.90	3.80	2.50
7.00 ± 0.05	7.01	-	8.20	7.40

Table 4.2: Crystal field levels of LiErF$_4$ in meV with respect to the ground state. All states are Kramers degenerate doublets. The measured energies are compared with the values from a calculation which uses the refined set of crystal field parameters and with values from literature.

a-axis and the b-axis, respectively.

The phase diagram as function of temperature and field along the c- and b-axes is summarized in Fig. 4.2. The transition temperature $T_N = 373 \pm 5$ mK agrees with the previous reports [14]. For fields along the c-axis, the intensity at Q=(010), corresponding to the order parameter squared, disappears at a sharp quantum phase transition at $H_{c||} = 4.0 \pm 0.1$ kOe. For fields along the b-axis, the Q=(100) Bragg peak disappears due to mono-domain formation. The (003) peak, which is independent of ab-domains, decreases towards $H_{c\perp} \simeq 2.1$ kOe, but a long tail remains up to 4 kOe. The (103) peak, measuring the uniform FM component, grows towards a kink at $H_{c\perp}$, corresponding to maximal polarization of the ground-state doublet. Above $H_{c\perp}$ a weak linear increase, coming from mixing-in higher lying crystal field levels, is well reproduced by the MF prediction.

A mean-field (MF) calculation yields a qualitatively correct phase diagram. In LiHoF$_4$,

the MF treatment accounts for most of the phase diagram except close to T_C, which is overestimated by 37% [3, 5]. In LiErF$_4$, T_N^{MF} = 728 mK, $H_{c||}^{\mathrm{MF}}$ = 5.25 kOe and $H_{c\perp}^{\mathrm{MF}}$ = 3.25 kOe are all dramatically overestimated. Unlike LiHoF$_4$, any NN exchange interaction cancels in the BLAFM and cannot fine-tune the phase boundary. Including hyperfine coupling has little effect: $H_{c||}$ = 5.75 kOe and T_N = 735 mK.
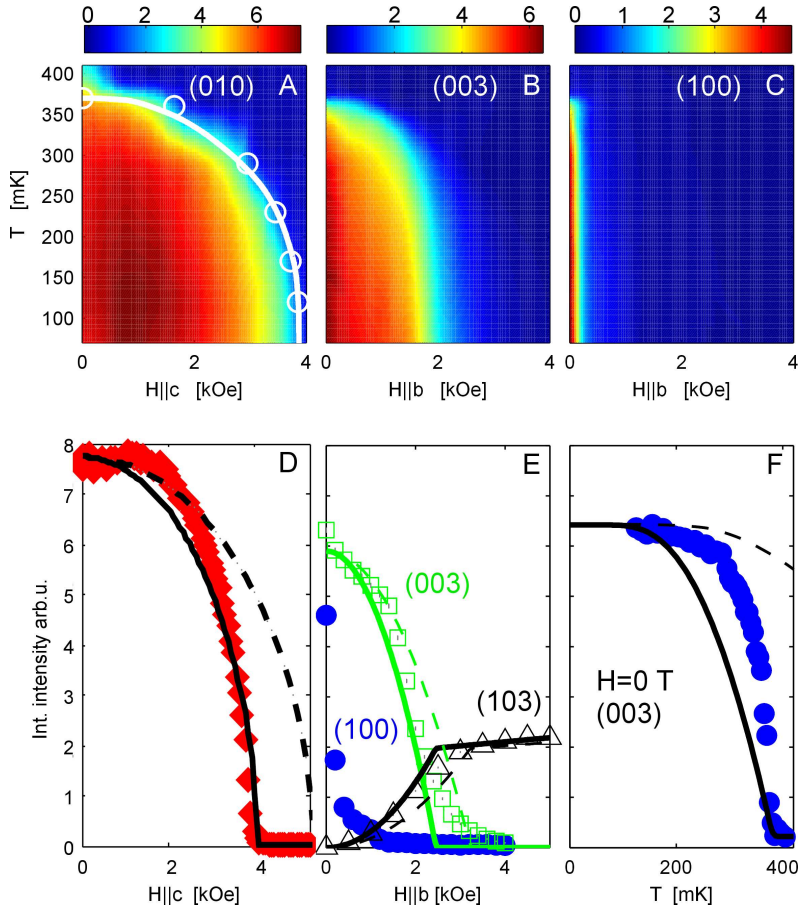

Figure 4.2: a-c) Field–temperature phase-diagrams from the intensity of magnetic Bragg peaks: (010) with $H||c$, (003) and (100) with $H||b$. d,e) Field dependence of intensities at T = 100 mK for field along c: (010) and along b: (100), (103), (003). f) Temperature dependence of the (003) intensity. In d-f), dashed lines are mean-field predictions. Solid lines are the same with temperature and field axes scaled by 0.52 and 0.76, respectively, to match the measured T_N and H_c.

4.2   Specific heat measurements

Specific heat (C_p) studies provide information on the magnetic energy of the system. In fact, integration of the C_p curves gives the energy and entropy of the ordered state. In addition, because of the low ordering temperatures of LiReF$_4$ family, the phonon contributions to specific heat are negligible or less pronounced and C_p measurements shed light on the magnetic characteristics of the systems. Mennenga *et. al* considered the heat capacity of several members of the family, including Re=Er [15]. By comparing the measured and calculated entropy and energy values, they established the layered antiferromegnetic (LAFM) as the favorable magnetic structure of LiErF$_4$, under the assumption that the exchange coupling is small. There, for instance, the quality of the data was not sufficient to track the behavior of the C_p curve close enough to the transition temperature to investigate the universality class of the system.

In this work, the specific heat measurements were performed at the Helmholtz Center in Berlin (Laboratory for Magnetic Measurements LaMMB - MagLab) using a cryogenic system consisting of an Oxford Instruments 14.5 T cryomagnet and a Heliox ^{3}He insert. This experimental setup is mainly dedicated to high-resolution caloric measurements at temperatures between 260 mK and 20 K. The heat capacity data were obtained using the standard pulse relaxation method. A single crystal of LiErF$_4$ with dimension 3x5x0.2 mm^3 (m = 7.3 mg) was attached onto the sapphire chip calorimeter with a small amount of (Apiezon N) grease (Fig. 4.3). Temperatures were measured using Lakeshore Cernox thermometers with an rms noise of 3 μK at 300 mK. The large contact area to the very thin sample ensured a fast sample–chip thermalization ($\approx$ 5 s), completely separated from the long ($\approx$ 1000 s) relaxation time to the thermal bath. This separation of relaxation times together with the very low noise in the temperature measurement, allowed measurements with relative temperature increments down to 0.05 %. Most data were collected with temperature increments of 0.2 %, which was verified to give identical results to the 0.05 % data, but with better statistical quality. A typical time-scan of the thermometer on the calorimeter chip during a heat pulse is depicted in Fig. 4.4. The heat capacity of the sample, C_p, was obtained from the total heat capacity by subtracting the contributions of the sapphire chip and grease, which constituted < 0.2% of the total at T_N. In addition, the shape of the C_p curves obtained from natural sample revealed a rounding of the thermal transition

on the order or 1% in reduced temperature. There was the idea this to be due to the hyperfine coupling in the 23% of naturally occurring Er-nuclei that carry spin. However, the measurements on a crystal grown using isotopically pure ^{168}Er, which has no nuclear moment, result in no significant differences that could be observed within the accuracy of the measurement.
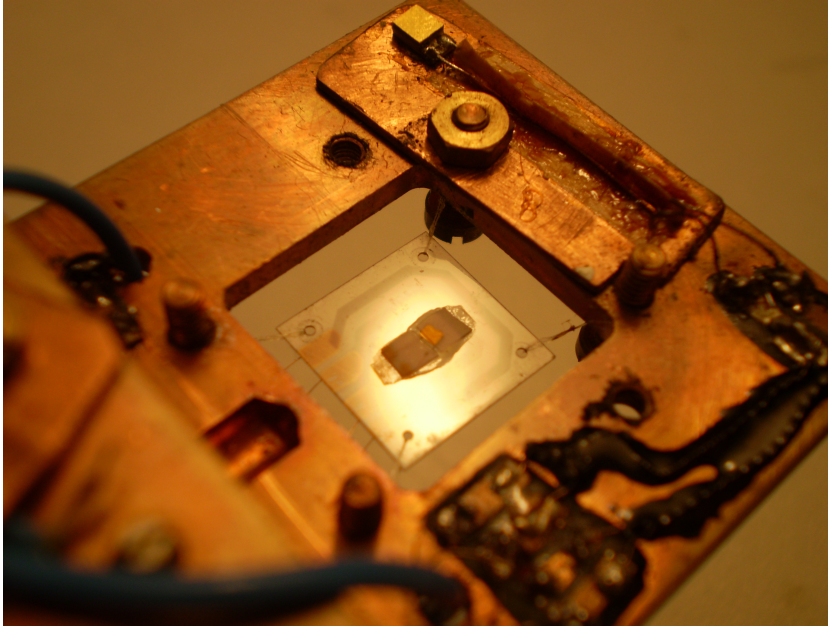

Figure 4.3: Photo of the 3x5x0.2 mm^3 crystal of LiErF$_4$ mounted on the sapphire chip calorimeter, suspended from a copper heat bath.

Fig. 4.5 summarizes the specific heat measurements on LiErF$_4$, with the method mentioned above. The pronounced peak at $T \simeq 0.37$ K establishing the magnetic phase transition [15] is in agreement with the previous studies [15] and the neutron scattering measurements in this work. Panel a of the figure shows the heat capacity measurements at several fields. The transition temperature (T_N) decreases in field and the long tail above T_N, which continues to high temperatures, is more significant than in the ferromagnetic LiHoF$_4$ and LiTbF$_4$ [46, 47, 48]. At high temperatures, the specific heat is dominated by the magnetic interactions (following T^{-2} in leading order [15]), crystal field and phononic contributions. The latter with the tendency of ρT^3, where $\rho = (6.6 \pm 0.1 \cdot 10^{-7})$J/g K^4, is less pronounced after cf subtraction at high temperature around 11 K. This is in contrast with the results in [15], where, by mistake, the higher level cf part was assumed to be phonon contribution. Around T_N, the specific heat

follows the universal power law

$$C_p = A \, |\tau|^{-\alpha} + B, \qquad \tau = T/T_N - 1, \tag{4.5}$$

for $T < T_N$ and $T > T_N$ around the critical regime. As indicated in the c panel of Fig. 4.5, the fit to the data in reduced temperature satisfies equal exponent values ($\alpha = -0.28 \pm 0.04$) below and above T_N within the window $t \leq 0.03$, while $A_+/A_- = 1.68 \pm 0.04$. Subtracting B reveals a crossover to $\alpha = -0.07 \pm 0.05$ for $\tau > 0.03$. The extracted critical parameters are far from the mean field predictions and the 3D models. In panel d, the $C_p(T)$ curves at different fields are scaled to the peak heights in reduced temperature. Below T_N the curves collapse to a single unique curve.
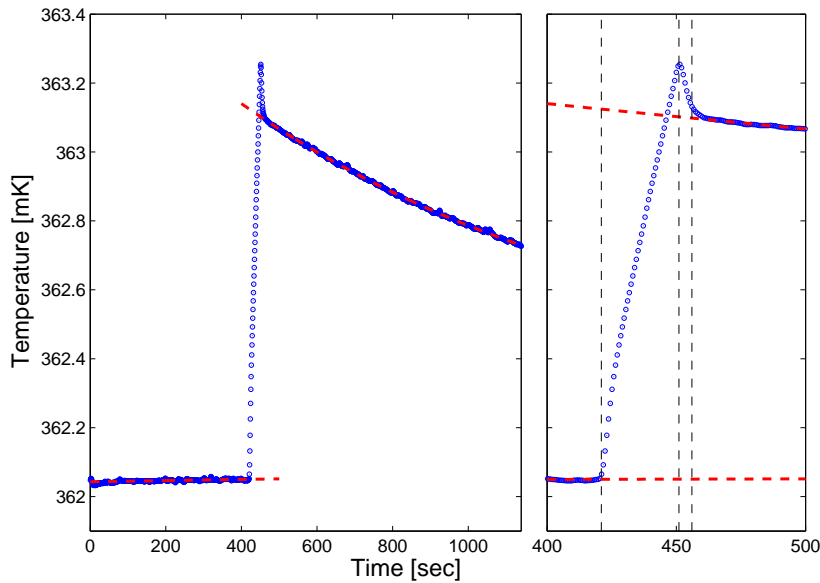

Figure 4.4: Typical time–scan of the thermometer on the calorimeter chip during a heat pulse. In the initial state (up to $t = 400$ s), the chip is in equilibrium with the thermal bath, to which it is weakly coupled. During the 30 second long heat pulse, there is a steep rise in temperature. The 5 s long, sharp drop in temperature marks equilibrium between chip and sample. Thereafter a slow equilibration back towards the thermal bath temperature is observed with the exponential relaxation time of 1060 ± 10 sec.
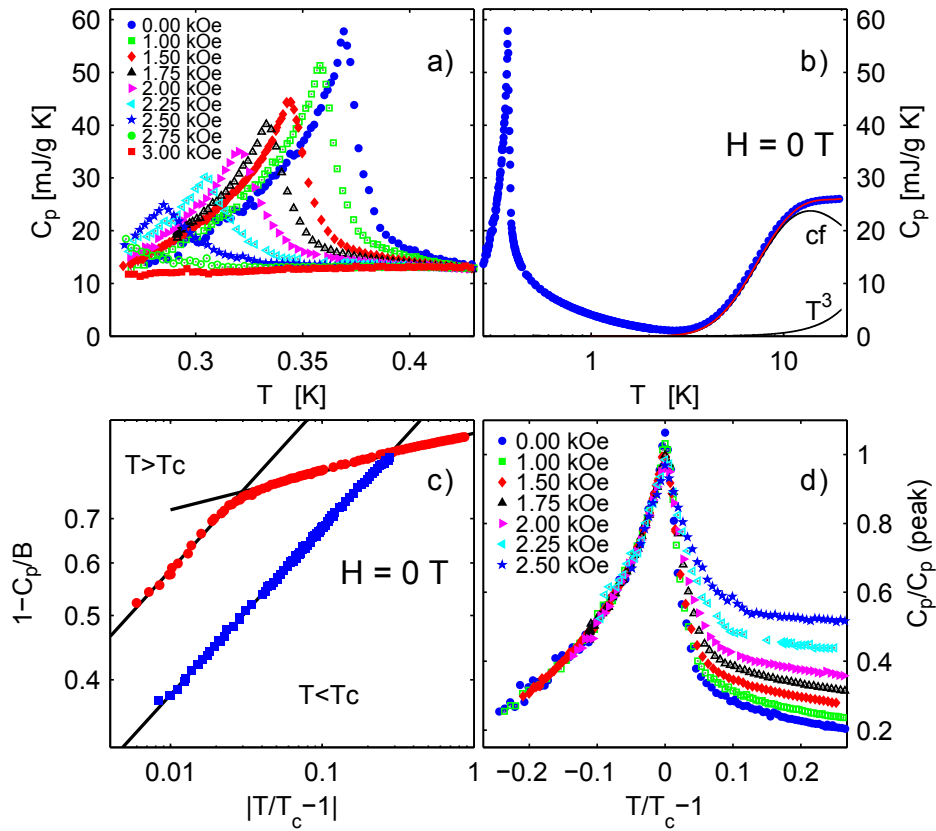
Figure 4.5: a) Specific heat versus temperature for several fields along the c-axis. b) Above 2K, specific heat is described by the crystal field Shottky anomaly (cf) and very weak T^3 phonon contribution (red line). c) Power law behavior of specific heat at $H = 0$ T determines critical exponents. d) Curves measured at different field values shifted to the same peak center and normalized by peak height to compare the evolution of peak shape. Below T_N the data collapse onto a unique curve.

4.3 AC susceptibility measurements

The AC susceptibility technique measures the local flux density ($\mathbf{B}$), induced inside a sample through an external excitation $H_{Ac} = H_{Ac0}\cos(\omega t)$ generated by a coil. The sample response is then collected by a second inductive coil, where its real and imaginary parts are [49]:

$$\chi' = \left(\frac{\omega}{\pi\mu_0 H_{Ac0}}\int_0^{2\pi/\omega} <\mathbf{B}> \cos(\omega t)dt\right) - 1, \tag{4.6}$$

$$\chi" = \left(\frac{\omega}{\pi\mu_0 H_{Ac0}}\int_0^{2\pi/\omega} <\mathbf{B}> \sin(\omega t)dt\right) \tag{4.7}$$

χ' measures the elastic in-phase component of the susceptibility, whereas $\chi"$ indicates the dissipation in the system.

The AC susceptibility measurements on LiHoF$_4$ revealed the MF behavior of the system around both thermal and quantum phase transitions [50]. χ' diverges at the transition temperature, and a power law fit results in a critical exponent $\gamma = 1 \pm 0.09$, in agreement with the MF predictions [51]. The same behavior is observed at QPT, confirming the fact that the system retains its MF character, while entering quantum ferromagnetic transition. Below 400 mK, the phase diagram revealed a sudden upturn in H$_c$, reflecting the Ho nuclear moments' alignment by the hyperfine interaction [3].

The AC susceptibility measurements on LiErF$_4$ were performed on a $1 \times 1 \times 10$ mm^3 piece of natural single crystal, and a $1 \times 1 \times 1$ mm^3 piece of the (^{168}Er) isotopic single crystal. The AC field was set to ≈ 42 Oe and the crystallographic *c*-axis of the samples was aligned with the direction of the DC field. Thermalization was carried out using 1200 μm diameter copper wires, which from one end anchored to the copper plate of the weak link and from the other end attached to the sample using Stycast *W*19. Due to the fact that the two samples had different geometries, the demagnetization was taken into account simply by scaling the magnetic field data by a constant, so that the bulk of the measured phase diagrams overlap. The measured T-H phase diagram of the natural sample is shown in Fig. 4.6, in agreement with neutron scattering results. Above 2 kOe,

$T_N(H)$ scales as a power law with exponent 0.34 ± 0.01. At H$_c$, $\chi(T)$ exhibits quantum critical scaling following a power-law exponent 0.70 ± 0.03 up to 250 mK, above which it crosses over to the classical Curie-Weiss behavior. This behavior around the QCP is in stark contrast to the MF behavior observed in ferromagnetic LiHoF$_4$ [50].
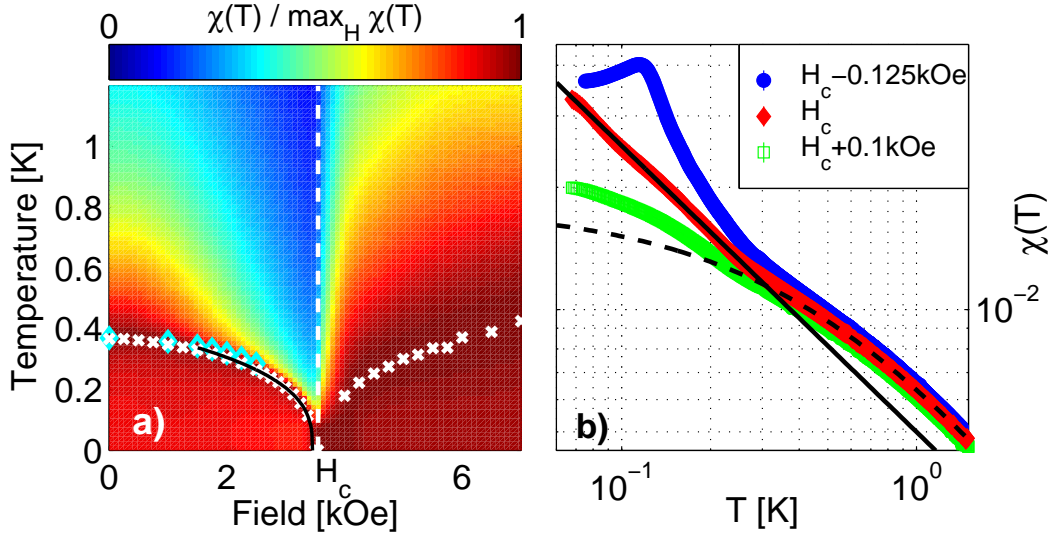

Figure 4.6: Susceptibility along the c-axis in LiErF$_4$. a) Susceptibility $\chi(T)$ normalised for each field. Peak positions are marked by crosses ($\chi(T)$) and diamonds ($C_p(T)$). Black line is power law fit to $T_N(H)$. b) $\chi(T)$ just below, at and just above H$_c$. At H$_c$, $\chi(T)$ displays quantum critical scaling with exponent 0.70 ± 0.03 (solid line), up to a crossover around 250 mK, above which, regular Curie-Weiss behaviour $C/(T - \theta_{CW})$ with $\theta_{CW} = -0.55 \pm 0.01$ K describes the data (dashed line).

In Li^{168}ErF$_4$ (fig. 4.7), the AC response from the sample is clearly more rounded than in the case of the natural sample. This could be due to a lower quality of the isotopic sample. Indeed, the sample is less optically transparent. At the base temperature ($T \sim 35$ mK) the critical field (H$_c$) of the isotopic sample is lower than the natural sample. This tendency continues until $T \sim 260$ mK, where both curves show similar response. Fig. 4.7 exhibits this behavior at different temperatures. Furthermore, the phase diagram could be mapped out by performing field scans at different temperatures (Fig. 4.8). The H$_c$ values were determined from the position of the χ' peak. An alternative way to extract the critical field is the minimum of the second derivative of χ' ($d^2\chi'/dH^2$) curve. The comparison between the phase diagrams obtained for both samples shows that the upturn around the quantum critical point in the natural

sample is due to the hyperfine interaction between the nuclear and electronic spins, which vanishes in the nuclear spin free isotopic $Li^{168}Er F_4$ case. This result gives the first experimental demonstration of the importance of hyperfine effect on the low temperature part of the phase diagram.
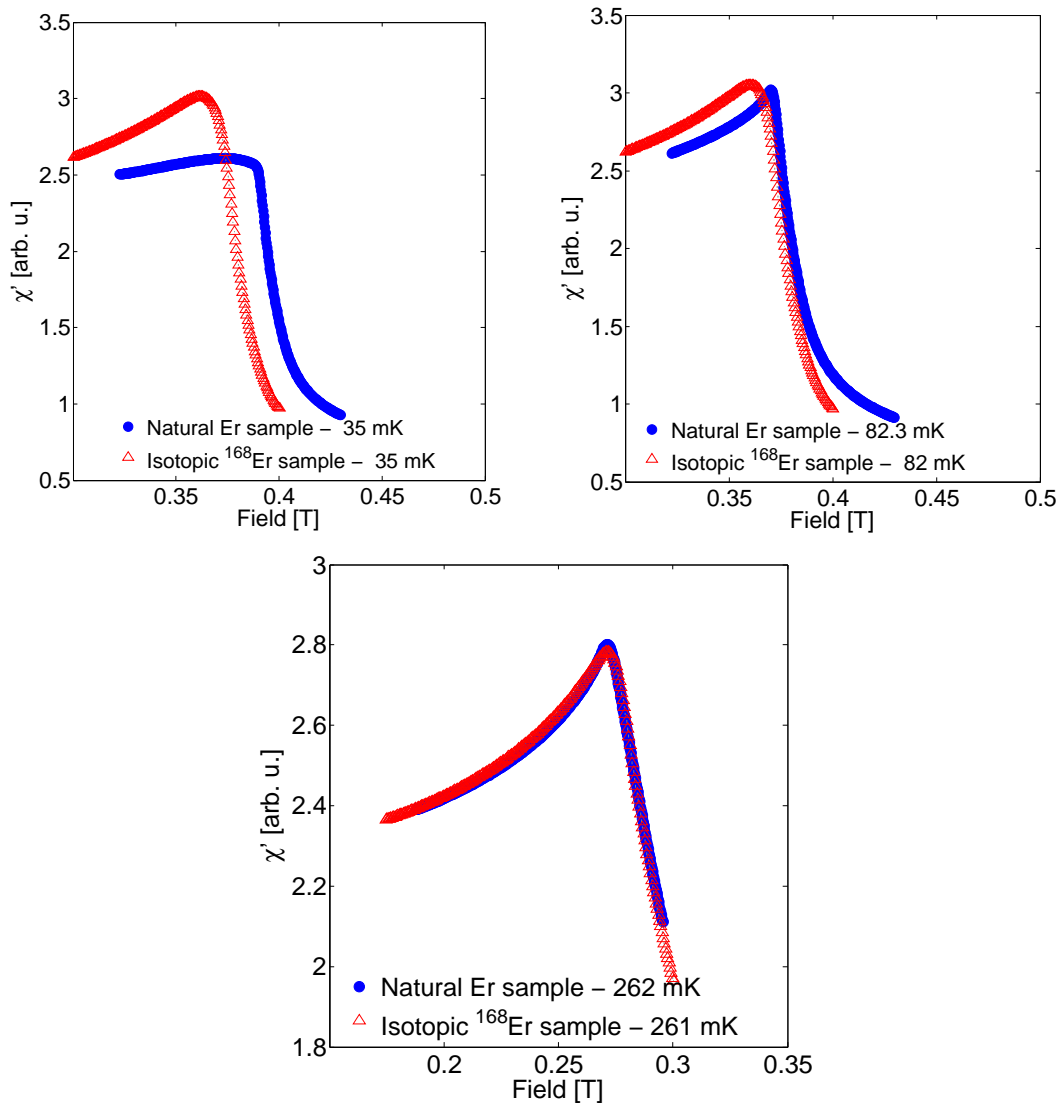

Figure 4.7: Real response of the AC-susceptibility (χ') comparison of natural (blue) and isotopic LiErF$_4$ (red) samples versus field at three different temperatures. At the base temperature, the H$_c$ value of the isotopic sample is lower. The curves move closer to each other until $T \sim 260$ mK, where they overlap.
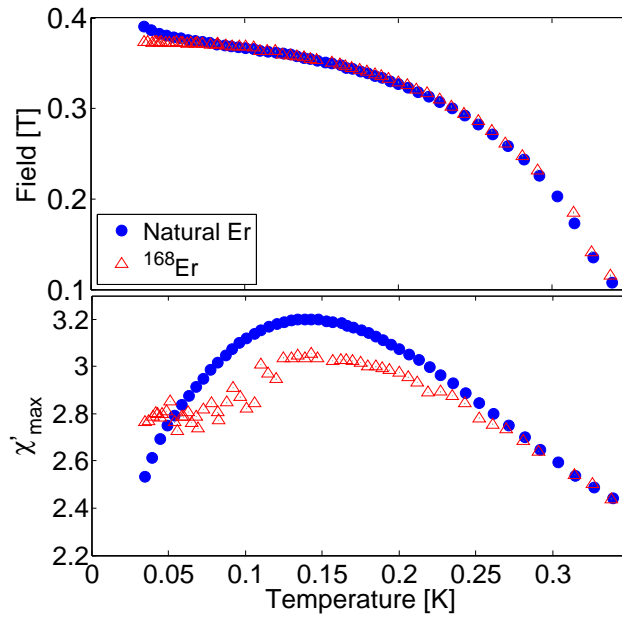
Figure 4.8: Phase diagram of natural (blue) and isotopic (red) samples. The upturn in the vicinity of the QPT is due to hyperfine coupling of the nuclear and electronic states. It vanishes in the isotopic sample due to the absence of nuclear spin in the ^{168}Er isotope.

4.4 Order parameter studies of LiErF$_4$ by neutron scattering

In this section, order parameter investigations performed on both natural and isotopic samples, and the related critical exponents (revealing interesting possibilities for the universality class of the system) are discussed. Further separation of the system from the expected 3D behavior is supported by the critical scattering and spin-spin correlation length studies presented in the next section.

4.4.1 Order parameter studies of the natural sample

As mentioned, rare earth fluorides are insulators with rather high heat capacities. In the critical experiments like order parameter or correlation length studies – where knowing the exact temperature of the sample is important for subtle analysis – one should make sure that the sample is well thermalized with the the temperature of the

thermometer attached or close to it. To improve the thermalization of the samples, a $10 \times 10 \times 30$ mm^3 single crystal of LiErF$_4$ was cut into blades of $10 \times 1.5 \times 30$ mm^3. The blades were then gold plated and squeezed together (with 150 μm of copper foils between them) inside a holder out of copper, covered with a few μm of gold.

Because the specific heat of the sample (Fig.4.5) is maximal at the transition temperature, the waiting time for thermalization increases close to T_N. Figure 4.9 compares the time scan of the Q=(100) magnetic Bragg peak intensity at two different temperatures. The thermalization was tracked by setting the sample temperature to the desired value and counting the intensity of the Bragg peak (BP) as a function of time. The required thermalization is achieved when the intensity is constant in time – confirmed by a simple exponential fit of the obtained curve.
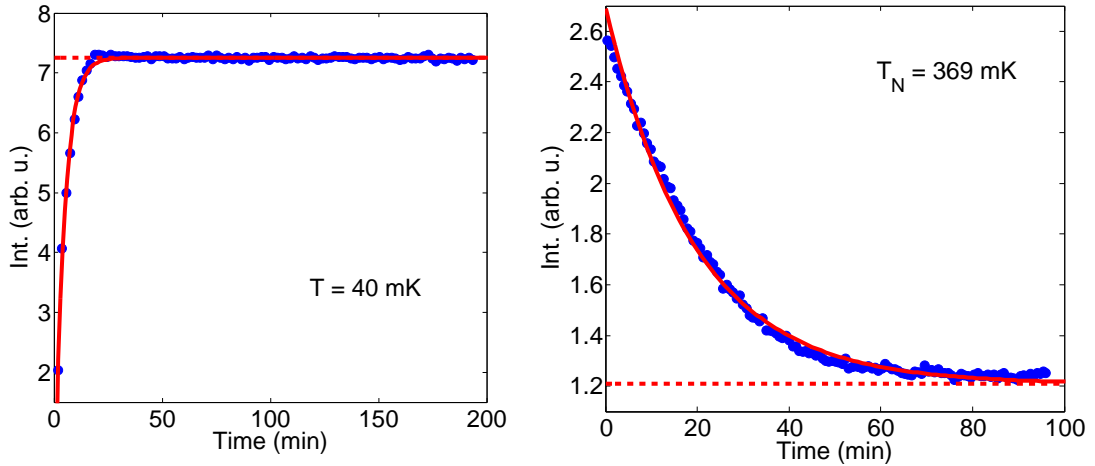

Figure 4.9: Intensity versus time scan of the (100) magnetic Bragg peak at base temperature (left) and transition temperature (right). The maximum waiting time for thermalization is $\sim$ 100 min.

Order parameter experiments of both natural and isotopic samples were carried on the E$_4$ 2-axis diffractometer and V$_2$ (FLEX) cold triple axis spectrometer at Helmholtz-Zentrum in Berlin. The sample was aligned with *ab* in the scattering plane and the magnetic field was applied along the *c* axis. At the elastic line, $\sim$ 110 μeV resolution was achieved at FLEX with $\mathbf{k}_i = \mathbf{k}_f = 1.55$ Å^{-1}. Because the relevant energy scale of the system is below this value (<0.1 meV), the measurements are effectively integrated over the relevant energy range. Therefore, with proper selection of collimators critical scattering (correlation function (s(q)) integrated over energy) could be investigated on

TAS with the advantage of the low background. The analyzer was fixed at the elastic position during the whole time. The advantage of the analyzer is an improvement of the signal to background ratio, compared to normal diffractometers. A Beryllium filter was placed in front of the analyzer to prevent the contamination by higher harmonics. There are two ways of measuring the order parameter: either to measure the intensity of the magnetic BP as function of temperature/field, or to perform reciprocal space scans (Q) at each value of temperature/field. The advantage of the first choice is the fast data acquisition. Besides, the uncertainties from the movement of the sample/instrument and the possible misalignment is prevented in this method. On the other hand, the second choice is more time consuming, but provides information on the the overall change of the signal distribution in Q space. The method is more appropriate for the case of correlation length studies, where diffuse scattering around the intense Bragg peak is being investigated. In the presented data, several scans are performed for each value of field/temperature. The quality of the measurements were tested by comparing the Q scans. Therefore, any sudden change in the background/intensity of the signal could be observed. These information could not be obtained from the simple temperature/field ramp at the BP.

At zero field, the onset of the order parameter appears at $T_N = 370$ mK. An applied magnetic field of $H \sim 4$ kOe along the crystallographic c-axis at base temperature ($\sim$ 80 mK), destroys the ordered state through QPT. The reciprocal space scans (obtained by the rotation of the sample by $\pm15°$ away from the magnetic BP), were fitted with a Lorentzian line shape – which can describe the critical correlations on the sides of the BP – folded with a Gaussian function with the fixed width corresponding to the finite instrumental resolution. Figures 4.11 and 4.10 demonstrate the intensity of the Q=(010) magnetic BP versus field and temperature. Order parameter obeys a universal power–low behavior close to the transitions. The critical exponents extracted in the vicinity of both thermal ($\beta_T = 0.15 \pm 0.02$) and quantum phase transition ($\beta_H = 0.31 \pm 0.02$) are depicted in the Fig. 4.11. These values significantly deviate from $\beta = 1/2$ predicted by the mean-field theory. Critical scattering, which diverges at the critical points, provides an independent way of T_N and H$_c$ determination, and thus ensures the accuracy of the fits.
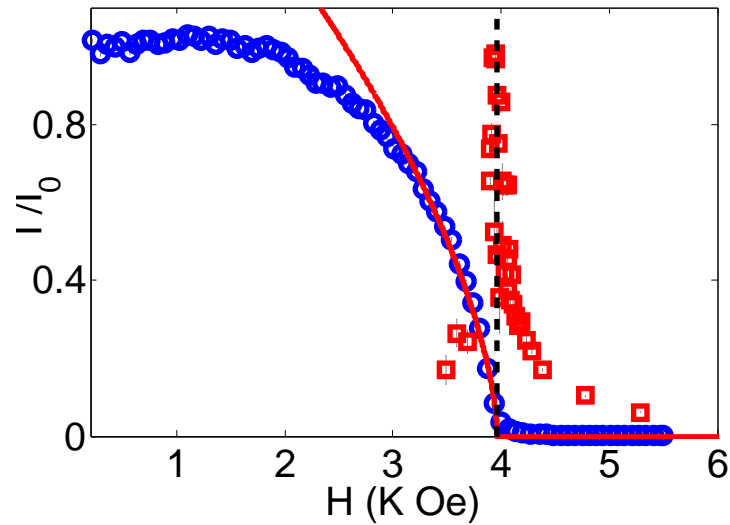
Figure 4.10: Intensity of the Q=(010) magnetic Bragg peak as a function of field along the c–axis at $T = 80$ mK (blue circles) and critical scattering (red squares) extracted by fitting a resolution–corrected sum of a delta function and a Lorentzian to Q scans. The red line is the power law–fit.

Figure 4.11: Q=(010) intensity as a function of temperature at $H = 0$ (blue circles) and a c-axis field at $T = 80$ mK (red squares). Lines are power–law fits. Inset: Intensity of the Bragg peak (blue circles) and critical scattering (red squares) extracted by fitting a resolution corrected sum of a delta function and a Lorentzian to Q scans.

4.4.2 Discussion

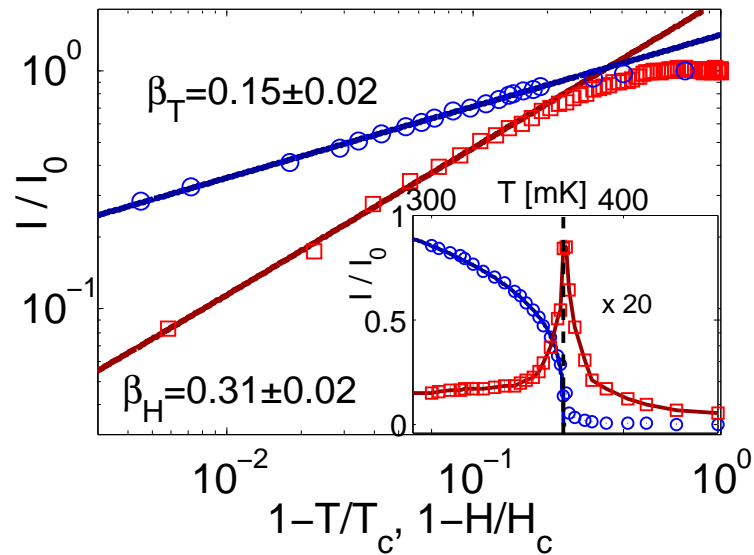Here, the nature of the phase transitions is discussed. With respect to the classical phase transition, the extracted order parameter exponent ($\beta_T = 0.15 \pm 0.02$) is far from $\beta = 0.3 - 0.35$ of the standard 3D universality classes [51]. It instead satisfies the window $0.125 - 0.23$ reported for 2D-XY criticality [52]. In addition, the specific heat exponent $\alpha = -0.28 \pm 0.04$ is more negative than $\alpha = -0.13$ to -0.198 predicted for classical, dipolar and quantum 3D Heisenberg models. Both exponents are consistent with recent Monte-Carlo studies on a dipolar 2D bi-layer square lattice, reporting $\beta = 0.18 \pm 0.02$ and $\alpha \simeq -0.4$ [53]. It is important to consider the other critical exponents for more subtle explanations of the observed behavior. The four additional exponents are specified by γ, ν, δ and η notations. γ and ν are related to the susceptibility and correlation length of the system, respectively. δ describes the variation of the order parameter in field ($M \approx H^{1/\delta}$), and η is the anomalous scaling dimension of the spatial correlation function ($< S_0 S_r >= |r|^{d-2+\eta}$). The latter two are valid exactly at the transition points. The renormalization group introduced by Wilson in 1970 provides a method to calculate the critical exponents. In fact, the value of the exponents depend on the spatial dimension, symmetry and range of the interactions, but not on their form and magnitude. Therefore, there exist *universality classes*, where the transitions belonging to the same universality class have the same critical exponents. A remarkable feature is that not all of the exponents are independent. For instance:

$$\alpha + 2\beta + \gamma = 2 \tag{4.8}$$

$$\gamma = \beta(\delta - 1). \tag{4.9}$$

Combining these relations with the hyperscaling relations $\gamma = (2 - \eta)\nu$ and $\alpha = 2 - d\nu$,

$$\delta = \frac{2 - \alpha}{\beta} - 1 \tag{4.10}$$

$$\eta = 2 - d\frac{\delta - 1}{\delta + 1} \tag{4.11}$$

could be obtained, which are believed to be the super universal exponents, depending only on the spatial dimensions. Inserting the extracted thermal critical exponents from specific heat ($\alpha = -0.28 \pm 0.04$) and order parameter ($\beta_T = 0.15 \pm 0.02$) into Eq. 4.10

results in $\delta \simeq 14.2$. In addition, injecting δ into Eq. 4.11 gives $\eta = 0.26$ for $d = 2$. This value of η (which is different from zero predicted by MF) signals strong fluctuations in the system, and is consistent with the large deviation in transition temperature from the mean-field prediction (723 mK). For 3D (Ising, XY and Heisenberg) $\delta = 4.7$, $\eta = 0.03$ are expected [51], whereas $\delta = 15$ and $\eta = 0.25$ are known for the 2D (Ising and XY/h_4) systems [54, 52]. Therefore, exponent $\delta = 14.2$ for LiErF$_4$ matches very closely the reported 2D values. 2D behavior of the thermal phase transition, which is not expected from the long-ranged 3D nature of the dipolar interactions, is very surprising. The observed effective dimensional reduction of the system could have been arisen from quantum fluctuations and the anisotropic nature of the dipolar interactions Based on Mermin-Wagner theorem the long-range order in pure 2D XY models is not possible, but even infinitesimal 4-fold (h_4) anisotropy leads to conventional order slightly above the Kosterlitz-Thouless transition. It is reported that weak h_4 anisotropy results in the effective exponents $\eta \simeq 0.35$ and $\beta \simeq 0.23$ [52], which on increasing h_4 approach $\eta = 0.25$ and $\beta = 0.125$ [55]. The estimated h$_4$ anisotropy in LiErF$_4$, provided below, is roughly close to the predicted value by Taroni. *et.al.* for $\beta = 0.15$ (obtained for LiErF$_4$) on a square lattice nearest neighbor.

Regarding the quantum phase transition, the $\beta_H = 0.31 \pm 0.02$ extracted for the critical exponent of the order parameter close to the quantum critical point is in agreement with the classical 3D systems, further confirming the Hertz result that a QPT in a d-dimensional system (2D XY/h_4 in this case) scales as a classical system in $d+1$ dimensions [56].

4.4.3 Order by disorder phenomena

In the previous section, "order by disorder" was mentioned as a possible explanation for the nature of the spin space dimensional reduction in LiErF$_4$. The concept of order by disorder was first introduced by Villain *et.al.* in 1980 [57], when studying a frustrated Ising model on a square lattice. At $T = 0$ the system is disordered. At higher temperatures where thermal fluctuations are present, a true transition to a ferrimagnetic state is observed. In addition, the ordered state could be preserved by site dilution with nonmagnetic ions, so the idea of "order by disorder" came out for the first time. Similar phenomena exist in quantum systems. There, quantum

fluctuations induce symmetry breaking in a degenerate ground–state manifold. At low temperatures some particular collinear states are entropically selected. Such a selection of order by quantum fluctuations was presented by Henley [58].

In LiErF$_4$, there is a continuously degenerate ground state manifold at the mean-field level, which is obtained by rotating the spins in the adjacent layers of the BLAFM system alternatively clockwise and anti–clockwise by an angle θ. But in reality when the fluctuations are present in the system, the symmetry is broken and the structure with spins pointing along a or b directions is preferred. Therefore, the spins only adopt angles of $\theta = 0, \pi/2, \pi, 3\pi/2$. In fact, with RPA the initial slope of the dispersions, and therefore the low energy density of states, as a function of θ can be calculated. The slope is minimal and the density of nearby low–energy states are maximal when moments are along a or b–axis. Hence, a reduction to the four–fold h_4 degeneracy could be explained via order by disorder mechanism.

4.4.4 h_4 **anisotropy and universality class**

There are two possible sources of the proposed h_4 anisotropy in LiErF$_4$: 1) One has its origin in crystal field. In LiErF$_4$, the crystal field parameters $B_4^4, B_6^4(s)$ and $B_6^4(c)$ induce planar anisotropy to the system. 2) The second anisotropy comes from order by disorder phenomena, discussed earlier. In order to understand the strength of the anisotropy induced from each source, the corresponding h_4 terms should be evaluated. According to the Monte Carlo simulations by Taroni. *et.al* on a nearest neighbor square lattice clock model [55], the value of $h_4/J \simeq 1$ yield effective $\beta_T = 0.15$ (J is the coupling strength). This is the value obtained in the classical regime for LiErF$_4$. To relate their results to LiErF$_4$ with long ranged dipolar couplings, the calculations can be compared within the MF approximation. The nearest neighbor square lattice has 4 neighbors ($h_{MF} = 4J$), which gives $h_4/4J \approx 1/4$ for the case of $\beta = 0.15$. Considering the MF ground state dipolar energy, the h_4 terms introduced by each source of anisotropy could be evaluated (see Appendix B for more details):

$$h_{MF} = \sum_{i,j,\alpha,\beta} \mathcal{J}_D \mathbf{J}_{xy}^2 \overline{\overline{D}}(i, j, \alpha, \beta) = 60.25 \; \mu\text{eV}. \tag{4.12}$$

1. Clock model was implied in LiErF$_4$ by calculating the classical energy of the crystal field while rotating the magnetic moment of length $J_{xy} = 3.28$ (being one of the states from the lowest-energy crystal-field doublet) in the plane. This results in $h_{4(cf)} = 0.11$ μeV, and therefore, $h_{4(cf)}/h_{MF} = 0.0018 \sim 0.18\%$. Hence, the h$_{4(cf)}$ anisotropy originating from the crystal field is nearly negligible, and insufficient to explain the observed $\beta = 0.15$ in LiErF$_4$.

2. For dipoles on a diamond-lattice, Henley addressed the quantum fluctuations as the source of order by disorder (obdo) at 0 K [59, 60]. LiErF$_4$ is in fact a distorted version of the diamond lattice. Therefore, Henley's argument can be used to calculate the size of the anisotropy induced by dipolar interactions in LiErF$_4$. Following their expression, obtained by second order perturbation theory, the energy correction to the ground state is $h_{4(obdo)} = 5.26$ μeV for LiErF$_4$. This gives $h_{4(obdo)}/h_{MF} = 0.09$, roughly of the same order of magnitude predicted by Taroni *et.al* [55]. Hence, the anisotropy induced from order-by-disorder may play role in the observed $\beta^T = 0.15$ (signalig a 2D universality class) at the thermal phase transition. Of course, this agreement should only be taken as an order of magnitude, because the comparison is done to a nearest neighbor clock-model on a 2D square lattice and not to a 3D dipolar coupled lattice. Secondly, Henley calculates quantum fluctuations, whereas it might be necessary to also include the thermal fluctuations around T_N .

4.4.5 Order parameter studies of the Isotopic sample

Order parameter studies on the isotopic sample were performed at E4 two-axis diffractometer at HZB in Berlin, on a $2 \times 2 \times 20$ mm^3 single crystal covered with a few μm of gold. The sample was aligned with *c*-axis perpendicular to the scattering plane. The aim of the experiment, was to investigate the effect of the hyperfine interaction on the phase diagram; especially in the vicinity of the QCP – where quantum fluctuations compete with low energy scale interactions so the hyperfine effect is expected to be more severe [61]. Below $T \sim$ 370mK, the $Q = (100)$ magnetic reflection exhibited the best signal-to-noise ratio. The BP intensity was obtained by fitting a resolution–corrected sum of a Gaussian and Lorentzian functions to crystal rotation (ω) scans. Due to the poor q resolution of the instrument, the intense BP separation from the

weak wide diffuse scattering, and therefore the proper critical scattering studies were difficult. Figure 4.12 demonstrates an example of a typical ω scan around the BP.
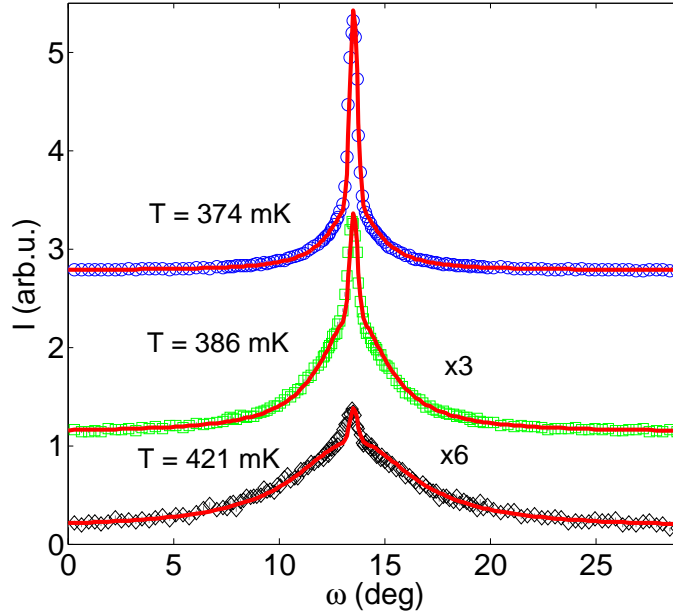

Figure 4.12: Typical ω scans transverse to Q=(100) reflection at different temperatures. The scans are have been fitted to a resolution–corrected sum of a Gaussian and Lorentzian functions.

The order parameter curve of the classical phase transition is similar to the result obtained from the natural sample. Close to T_N, the thermal fluctuations are strong, therefore a proper fit to the scans is difficult. The exponent β could vary between $0.16 - 0.24$, and $\beta_T^I = 0.16 \pm 0.03$ gave the best fit. Fixing the exponent to 0.3, to test the probability of a 3D value, increased the uncertainty of the fit. Figure 4.13 shows the behavior of the two samples' classical order parameter, where the curves have been scaled to ease the comparison.

Surprisingly, in the presence of an applied magnetic field ($H \parallel c$) – at base temperature – the order parameter of the isotopic system behaves very differently from the natural sample. The critical exponent ($\beta_H^I = 0.5 \pm 0.01$) is MF-like, and is far off from $\beta_H^N = 0.31 \pm 0.02$, obtained from the previous measurements on the natural sample (Fig. 4.14). This odd behavior could in principle come from three sources: (1) the absence of the hyperfine effect in Li^{168}ErF$_4$, which could re-scale the quantum fluctuations close
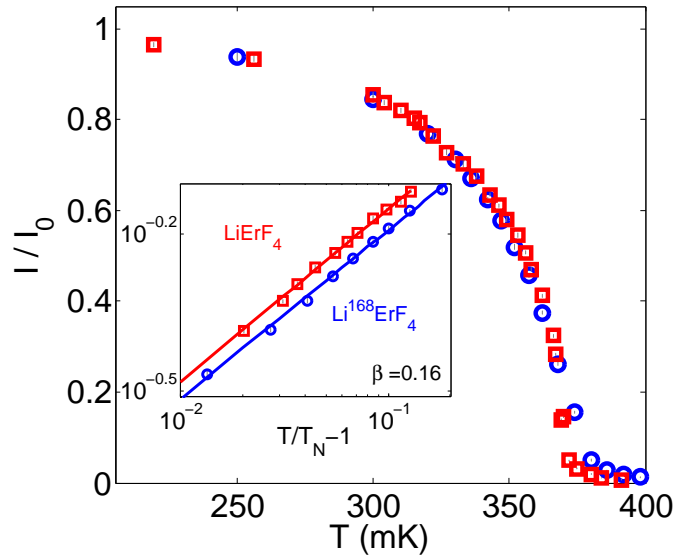
Figure 4.13: Intensity (order parameter squared) of Q=(100) BP versus temperature for natural (red squares) and isotopic (blue circles) samples. The curves have been scaled for better comparison. As the power–law fits around the critical region indicate (inset), both curves have the same critical exponents.

to H$_c$. Its effect on the phase diagram was already observed from AC-susceptibility measurements (Fig.4.8). On the other hand, the hyperfine coupling in natural Er is very small (~ 0.5 μeV). Therefore, it is difficult to believe such a dramatic effect to be just the result of hyperfine–free interaction in the isotopic sample. (2) Another possibility for the observed discrepancy could be the sample quality. Growing an isotopic sample is more difficult than the one with natural abundancy. Optically, the Li^{168}ErF$_4$ sample is porous and is not as perfect as the natural sample. Therefore, it is possible that the existence of some amount of impurities could have changed the sample characteristics. But given the same values for both T_N and H$_c$ and similar classical exponent, this probability is weakened. (3) One more reason could be the demagnetization effect due to the different shape of the measured samples. LiErF$_4$ (natural) sample is a rectangle with the long ($\sim$ 30mm) length along the c axis. On the other hand, the isotopic sample is needle–shaped, with length $\sim 30°$ away from the field direction ($\parallel$ c). The higher demagnetization field in the isotopic sample is obvious due to its larger H$_c$ value – by roughly $\sim$ 10% – compared to the H$_c$ of the natural sample. In fact, the demagnetization field lowers the effective field on the sample so

61

the critical field appears at a higher value. In the rectangular (natural) sample, since the path of the magnetic field is large (it is almost 3 times larger than in the other two in–plane directions) the demagnetization field is small (as usually for needle-like samples). However, in the isotopic sample – where its irregular shape makes the demagnetization field calculation complicated – it seems that the thin path of ~ 2 mm is more preferable for the magnetic flux to pass through, rather than through the relatively larger distance outside the sample (disk-like). Whether the demagnetization field can alter the exponent, and if so, how much, is not clear. One should notice that in LiErF$_4$ $g_\perp \sim 4g_\parallel$, so the longitudinal demagnetization field should not be sizeable. Hence, the noticeable difference between the order parameter curves of the samples at QPT is a mystery and needs further inquiries.
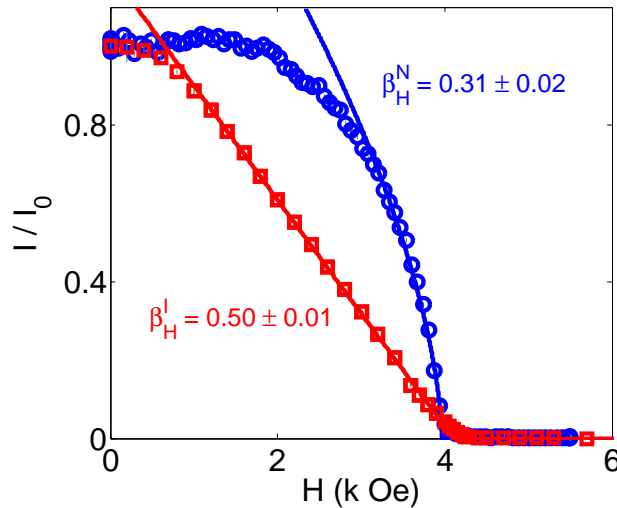

Figure 4.14: Intensity (order parameter squared) of Q=(100) BP versus applied field along the *c*–axis. The isotopic sample (red squares) clearly shows a different exponent (MF-like) from the natural (blue circles) sample (3D class). The slightly higher value of H_c in the Li^{168}ErF$_4$ system could be due to the demagnetization effect mentioned in the text.

Due to the lack of available dataset, it was not possible to map the detailed shape of the phase boundary of the isotopic sample. However, the absence of the upturn around QCP – in agreement with Ac-susceptibility measurements – is roughly visible at low temperatures. Figure 4.15 displays the evolution of the order parameter curve as a function of magnetic field ($\parallel c$) at different temperatures.
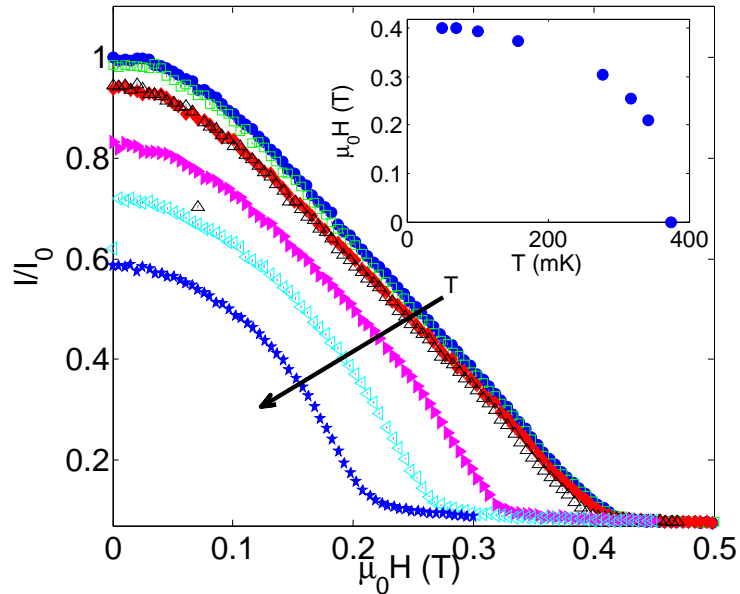
Figure 4.15: Intensity (order parameter squared) of (100) BP versus applied field along c axis at different temperatures. The absence of the upturn at QCP is obvious from the phase diagram (inset).

4.5 Complementary techniques to study order parameter

The next two subsections introduce neutron backscattering and muon spin rotation (μSR) as tested methods to investigate the order parameter. Although the experiments were not successful – as are explained in details in the following – to study the desired subject, they still provided useful information about the measured systems.

4.5.1 Nuclear spin excitations in LiReF$_4$ (Re=Ho,Er), studied by neutron back scattering technique

According to neutron scattering and AC-susceptibility measurements, hyperfine interactions play an important role in the phase diagram of LiHoF$_4$. Careful studies of the excitation spectra while tuning through the QCP revealed that hyperfine coupling to the nuclear spin bath forestalls the electronic mode softening expected for a QPT

[3]. This limits the ability to observe intrinsic electronic quantum criticalities. As discussed in sections 4.4.5 and 4.3, the hyperfine interactions – although not dramatic – also play a role in the phase diagram of LiErF$_4$. Therefore, studying the nuclear excitations helps in quantitative understanding of the effect. Probing nuclear energies demands high resolution spectrometers. Besides, low temperatures ($T < 1$K) are typically required to suppress any thermal dynamics of the electronic system. Considering the typical hyperfine splittings of the range of few μeV, high resolution backscattering neutron spectrometers are suitable to measure their effect [62]. Hence, the inelastic scattering of the neutrons from nuclear spins can be studied if the nucleus incoherent scattering is strong enough. In the process of scattering a neutron from a nucleus with spin I, the spin of the neutron flips with the probability of 2/3. The nucleus, which the spin-flipped neutron has scattered from, changes its magnetic quantum number by ± 1, due to the conservation of the angular momentum. Therefore, if the nuclear ground state is split into different energy levels as a consequence of the hyperfine interactions, the neutron spin–flip causes a change in the energy levels. This energy change is transferred to the scattered neutron. If the incident energy is higher than the inelastic signal, one expects a single elastic peak and two inelastic peaks on energy–loss and energy–gain sides – if the sample has only one stable isotope. Moreover, the energy of the inelastic signal is proportional to the order parameter in the systems containing only one magnetic sublattice [63].

Since LiReF$_4$ single crystals are of high quality, the extinction might be an issue. Extinction is essentially the attenuation of the primary beam by Bragg scattering from perfect crystals, which increases with the order parameter. Therefore, an extinction–free way of order parameter determination is to track the hyperfine energy splitting versus temperature/field. Chatterji *et. al.* [64] measured hyperfine interactions in CoF$_2$ through high–resolution neutron spectroscopy. They succeeded in measuring the order parameter with the critical exponent $\beta = 0.313 \pm 0.007$. In this approximation, nuclear moment is simply a spectator measuring the expectation value of the electronic moments. In systems with strong hyperfine coupling and a low electronic energy scale, hybridization will happen and the nuclear channel will contain richer behavior. LiHoF$_4$ and LiErF$_4$ lie on this threshold, when field and temperature allow tuning from spectator to hybrid behavior. Holmium has only one stable isotope ([165]Ho) with 100% natural abundance. Its nuclear spin is $I = 7/2$, where the nuclear

magnetic moment ($4.17\mu_N$) and the incoherent scattering cross section (0.36 barn) are fairly large. Therefore, Ho and Ho-based compounds are suitable to study nuclear spin excitations. On the other hand, Erbium has only one stable isotope containing nuclear spin (^{167}Er), $I = 7/2$, with only 23% natural abundance. Its nuclear magnetic moment is $-0.56\mu_N$, and the incoherent scattering cross section is ~ 1.1 barn. Hence, Er-based materials are also good candidates to investigate low energy excitations. The Hamiltonian of the hyperfine interaction is:

$$\mathcal{H} = A(\mathbf{I} \cdot \mathbf{J}), \tag{4.13}$$

where A is the hyperfine coupling. Its value is 3.36 μeV [5] and 0.5 μeV [44] for Ho and Er ions, respectively. $\mathbf{I}$ and $\mathbf{J}$ stand for the nuclear and electronic angular momenta, respectively. At zero temperature, the MF calculation of the single ion hyperfine interaction – corresponding to the ground state energy change of $\Delta E = E_m - E_{m\pm1}$ ($\Delta I = 1$) [65] – gives 19 μeV and 1.7 μeV for Ho and Er ions, respectively. It is a rough approximation which provides a good starting range to look for the excitations in the measurement. The experiment was performed at the backscattering neutron spectrometer SPHERES of the Jülich Centre for Neutron Science located at the FRM II reactor in Munich. Three blades of LiHoF$_4$ crystals – each with dimension of $10 \times 1.5 \times 30$ mm^3 – and one single blade of LiErF$_4$ were used for the measurement. The crystals were aligned with ab in the horizontal scattering plane. A precise alignment was not necessary simply because the measurements were performed in zero magnetic field. The selected $\lambda_i = 6.271$ Å provided δE ~ 1 μeV resolution at the elastic line. The aim of the experiment was firstly, a more accurate determination of the hyperfine coupling parameter (A), which is important for quantitative models. Secondly, an independent way of measuring the order parameter to ensure the already extracted value for β_T was desired. Figure 4.16 presents the typical energy scan obtained from both systems. The spectra are the result of summing up the counts of the individual detectors placed at different scattering angles. Surprisingly, no inelastic signal could be detected from the samples, nor in any single detector. Several reasons could attribute to no signal observation: (1) It was found out that the samples were not aligned properly with respect to the center of the beam, resulting in a loss of some amount of the signal. (2) The rather high absorption cross sections of Er (~ 554 barn) and Ho (~ 225 barn) could have weakened the signal. (3) Insufficient neutron flux at SPHERES could be another

reason for the unsuccessful experiment. Ehlers *et.al.* were able to measure the nuclear energy splitting of another Ho-based system, Ho$_2$Ti$_2$O$_7$, at the powerful backscattering spectrometer BASIS at the Spallation Neutron Source (SNS)/Oak Ridge [66]. Based on their observations, the intensity of the inelastic excitation was less than ~ 20% of the elastic intensity, which is of the order of the background in the presented experiment. However, the idea and the theory behind that are rather interesting. A higher–flux facility would probably give a more promising result. Especially, the measurement is more feasible in LiHoF$_4$ due to the rather large hyperfine coupling of the Ho nuclei.

4.5.2 μSR measurements on LiErF$_4$

Since muons are able to probe the local field at the sites they occupy within a lattice as well as its spatial and temporal variation, they are a suitable tool to study magnetic systems. To date, no μSR measurements on LiErF$_4$ have been reported. The goal of our muon experiment on LiErF$_4$ was to measure the AFM order parameter as a function of field and temperature. Since the muon precession frequency is proportional to the local field, the μSR signal can track the order parameter. In addition, the measured signal can provide information about the nature of the internal magnetic field distribution, as well as its width and fluctuations. These measurements could be further compared with the Ising member of the family (LiHoF$_4$) and improve the knowledge of the system at the microscopic scale. The experiment was performed on four plates of gold sputtered $12 \times 4.5 \times 1.5$ mm^3 single crystals attached to a silver sample holder side by side (providing a total 12×18 mm^2 surface) to optimize the full area coverage of the holder. The c-axis was perpendicular to the surface of the holder and along the magnetic field direction. The measurement was carried out at the "Low Temperature Facility" (LTF) at Paul Scherrer Institut (PSI), in Zero Field (ZF), Longitudinal field (LF), and Transverse Field (TF) modes. In the LF case, the muon spin were along the applied magnetic field; and in the TF measurements the muons were implanted with the spin at 45° away from the c-axis. Temperature scans at zero field were performed from $0.019 - 3.5$ K. A typical example of two ZF runs below and above the transition temperature is presented in Fig. 4.17. Over the whole temperature range, the data looked qualitatively similar, and could be fitted by two exponential functions
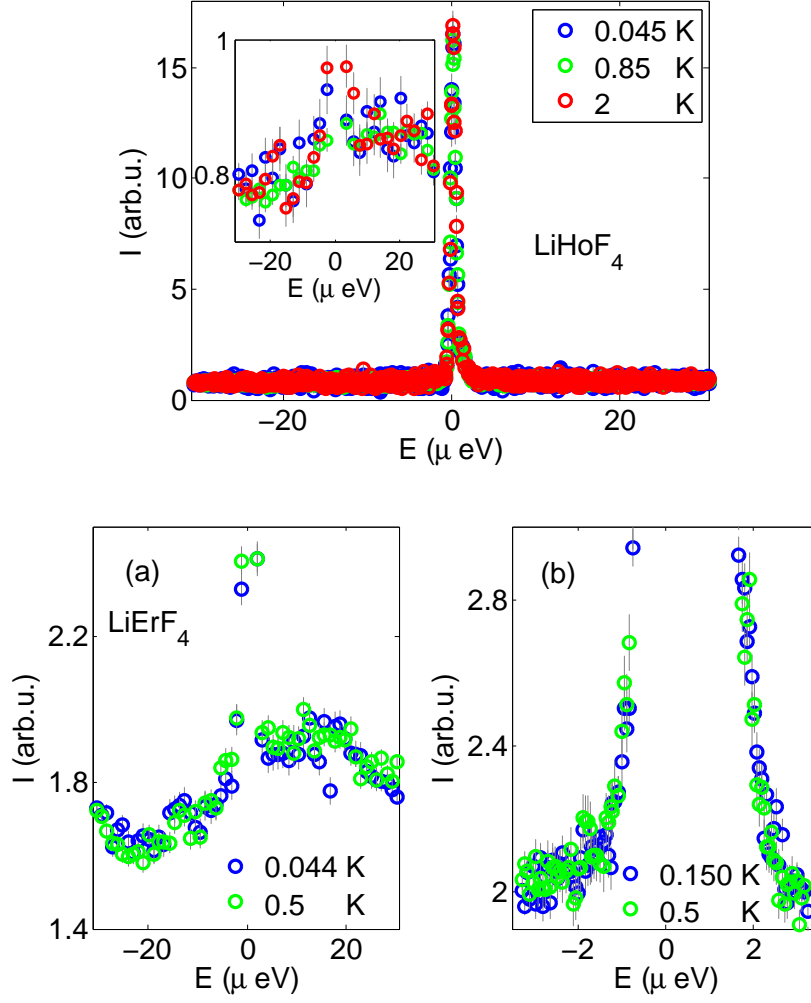
Figure 4.16: Top: Inelastic spectra of LiHoF$_4$, measured on the back scattering neutron spectrometer SPHERES/FRMII at three different temperatures, below and above $T_c = 1.53$ K. Bottom: Inelastic spectra for LiErF$_4$ with wide (a) and narrow (b) energy scans, below and above $T_N = 0.37$ K. No inelastic signal was observed in the range $\pm 30\,\mu$eV, mostly due to the insufficient flux.

$$G(t,\lambda) = Afe^{-\lambda_1 t} + A(1-f)e^{-\lambda_2 t}, \tag{4.14}$$

where $A = 0.138$ is the overall amplitude of the signal, which was constant at all temperatures. $f = 0.88$ is the fraction of the total amplitude – corresponding to the first exponential, and λ_1 and λ_2 are the relaxation rates of the two functions,
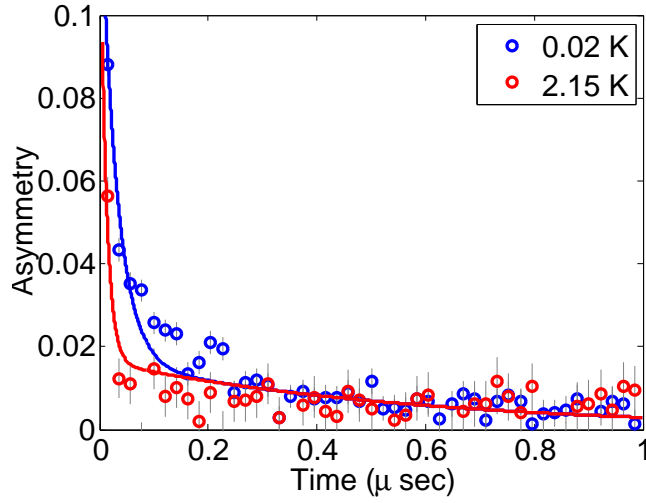
respectively.

Figure 4.17: ZF asymmetry versus time at two temperatures, below and above T_N = 0.37 K. The scans look qualitatively similar. The relaxation to zero asymmetry with time is a characteristic of magnetic fluctuations, as explained in the text.

The response is different from the usual Kubo-Toyabe (KT) function at static local fields, with a flat tail reaching to 1/3 at long time. In fact, the extracted signal relaxes to zero as a function of time, which is more like the behavior expected from magnetic fluctuations [37]:

$$G(t, v) = Te^{(T-1)vt}, \tag{4.15}$$

where T is the asymmetry of the static signal at very long times ($T = 1/3$ for the KT case), and v corresponds to the internal field fluctuation rate. As in many fluorine systems, muons most likely stop at half–way between the nearest neighbor fluorine nuclei, which are (0 ±1/4 1/8) and (±1/4 0 -1/8) within the unit cell of LiReF$_4$ [67]. The calculated dipolar field contribution from Er ions at these sites summed over $15 \times 15 \times 15$ lattices – at the ordered state – is about 22 kOe, which corresponds to a muon precession frequency of about v = 298 MHz (the gyromagnetic ratio of the muon is γ = 135.5 MHz/T). Therefore, a large internal field generated by Er ions with considerable magnetic moment ($J = 15/2$), is indeed expected to be observed in the experiment. It turned out that λ_2 (the slower relaxation rate) is temperature

independent, and most probably comes from a fraction of the muons which did not land inside the sample. On the other hand, the faster component λ_1 (Fig. 4.18) decreases towards T_N while cooling down from 3K, and remains almost constant below the transition within the error bars. The amplitude of the ZF signal was observed to be smaller than expected (it is typically 0.25). Since the antiferromagnetic state occurs in 100% of the sample, it is unlikely that the missing asymmetry is due to a fast relaxing fraction of muons. Instead, it is probable that the field at the muon site is so big that the signal is quickly relaxed to about 1/3 of the asymmetry within the initial blind window (5.3 ns); and then the only thing that was observed was the relaxation of the 1/3 tail due to "slow" fluctuations of the local magnetic field. In fact, and from what was mentioned above, it can be expected that the static μSR signal in LiErF$_4$ relaxes in a time scale of 3ns ($\approx 1/298$ MHz) which is smaller than the blind window of the signal. Within this assumption, the fast relaxing part of the ZF signal can be analyzed with Eq. 4.15 [37]. Comparing the Eq. 4.14 and 4.15 suggests a proportionality factor of $\nu \approx 1.8 \times \lambda_1$ for the internal field fluctuation rate. Unfortunately, the errorbars in the data are not small enough for further investigation of the order parameter critical exponent. In the case of LiHoF$_4$ and LiHo$_x$Y$_{1-x}$F$_4$, a large static field generated by the Ho nuclei, and a fast relaxation rate of the signal could be measured [68]. The "quasi–static" scenario proposed here for the XY–AFM member of the family LiErF$_4$, confirms the argument of the larger internal fluctuations of the system with the h_4 anisotropy, which results in a larger deviation from the MF predictions.

LF studies at 20 mK were performed in the presence of several magnetic fields applied in the direction of the muon spins within 0.5–8 kOe range. In contrast to LiHoF$_4$, where the amplitude of the signal decreases as a function of field, implying a static internal field of 20 kOe [37], here in LiErF$_4$ the signal amplitude did not vary all the way up to 8 kOe (Fig. 4.19). This observation confirms that the static internal field at the muon site is bigger than 20 kOe, in agreement with the "quasi–static" picture – discussed in ZF analysis. As presented in Fig. 4.19, the relaxation rate of the signal shows a broad maximum at the transition field.

In TF measurements (Fig.4.20) the muon spin is rotated by 45° with respect to the applied field. A fast oscillation at the beginning of the signals was noticed together with a fully precessing background. The background was found to have a field–independent
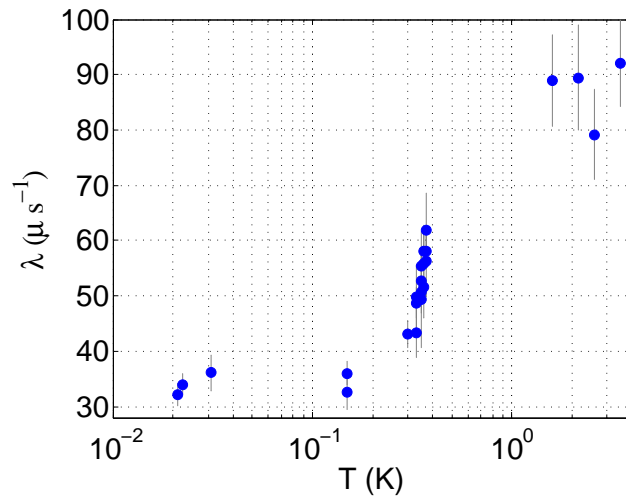
Figure 4.18: Temperature dependence of the fast relaxation rate (λ_1) in zero field. When cooling from 3.5 K, λ_1 decreases towards T_N and remains constant below the transition. Unfortunately, the errorbars are too large to determine the critical exponent of the phase transition.
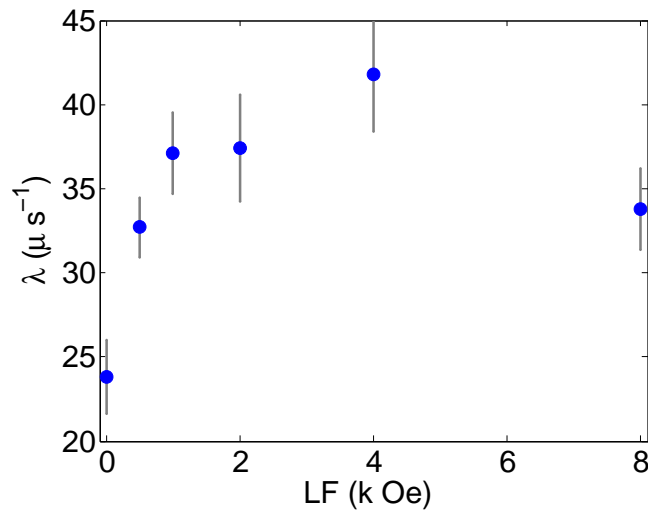

Figure 4.19: LF dependence of the relaxation rate ($\lambda_L F$) at 20 mK, shows a maximum at H_c, where the enhancement of the quantum fluctuations are expected.

relaxation rate and a frequency equal to the Larmor frequency of the muon. The background was fitted above 0.1 μs, and then it was kept fixed for the early time (< 0.1 μs) analysis. The fast oscillating part of the signal was fitted to a Gaussian damped harmonic function:

$$G(v, t) = Ae^{-(\lambda t)^2} \cos(2\pi v t + \phi), \tag{4.16}$$

where the amplitude $A = 0.075$ was found to be field-independent, and kept constant for all runs. λ, v and ϕ are the relaxation rate, frequency and the phase of the internal field response, respectively. As presented in Fig. 4.21 all fitting parameters exhibit a noticeable change in the 2–3 kOe range, after which they become constant (within the errorbars). Unfortunately, no more quantitative information could be extracted from TF measurements because of the large existing uncertainties.

In summary, μsr measurements on LiErF$_4$ confirm the existence of a fluctuating local field produced by Er ions in the system. In fact, the internal field at the muon sites is so large that the signal relaxes within the first 3 ns, and therefore can not be covered completely within the muon's time window, and only its relaxing tail can be recorded. This observations are in agreement with the large deviation of the critical points from the MF predictions and the order-by-disorder scenario.
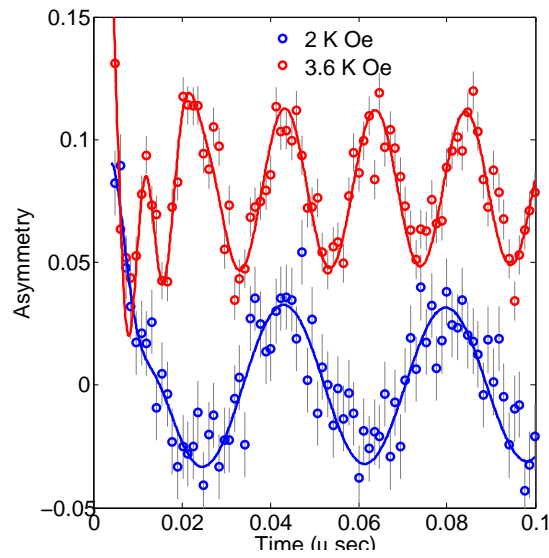
Figure 4.20: Asymmetry versus time at 22mK. Faster oscillations are obvious close to H_c. The scan at 3.6 kOe is shifted for better visualization.
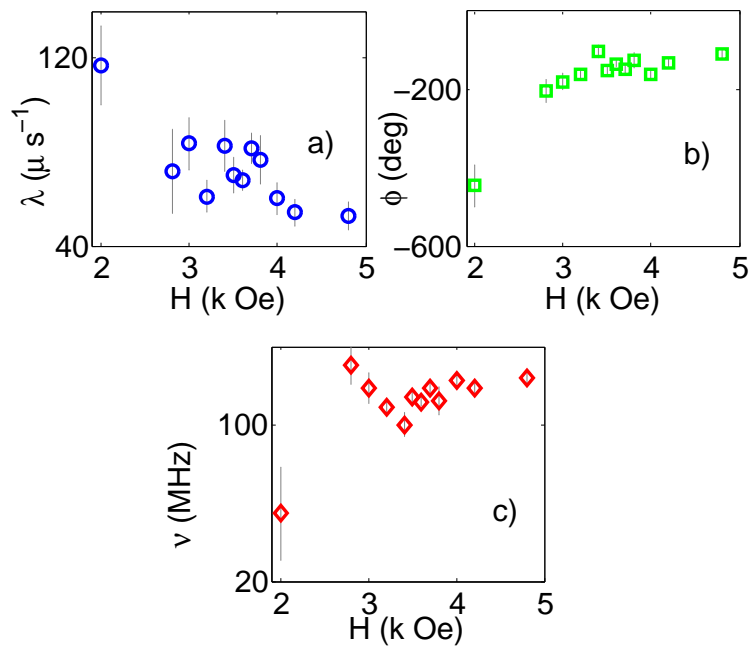

Figure 4.21: TF dependence of the fitting parameters in Eq. 4.16 at 20 mK. The sizable change in all parameters is observable in the 2-3 kOe range.

4.6 Magnetic correlation length studies of LiErF$_4$

Magnetic correlation studies on LiErF$_4$ (natural sample) were performed along all three crystallographic directions. Due to several difficulties from the experimental point of view, the measurements along the crystallographic c-axis are presented in appendix A. Imperfect collimation in field studies and a sudden failure in the thermometer performance during the experiment are the reasons for the remaining doubts.

The measurements along a,b-axes were carried out on V2 three-axis spectrometer at HZB/Berlin – as a part of the order parameter investigations (4.4.1). A $10 \times 10 \times 30$ mm^3 single crystal of the natural sample (cut into blades and plated with gold to improve thermalization) was oriented with (h,0,0) and (0,k,0) reciprocal lattice vectors in the horizontal scattering plane. Two $40'$ collimators were inserted after the monochromator and after the sample to facilitate the diffuse scattering separation, which is weakly spread on the sides of the intense magnetic BP. This improves the signal–to–noise ratio. Correlation length and critical scattering were measured by wide longitudinal ($1+\xi$ 0 0) and transverse (1 ξ 0) reciprocal scans through the (100) magnetic BP at different temperatures/magnetic fields ($\parallel c$-axis) in the vicinity of both classical and quantum phase transitions. Figure 4.22 compares the two scans in perpendicular directions at 384 mK. From the figure, it is clear that the longitudinal scan is wider than the transversal one. This behavior, which demonstrates the highly anisotropic distribution of the intensity in reciprocal space, is the same for the whole studied temperature range.

The structure factor S(Q) for the critical scattering could be modeled by a Lorentzian function. In the case of the longitudinal scan for instance it is given by:

$$S(Q) = \frac{\chi_0}{1 + (Q_H - Q_H^0)^2 \xi_a^2},$$

(4.17)

where Q_H and ξ_a are the wavevector component along Q=(H,0,0) direction, and the correlation length along a, respectively. The amplitude of the critical scattering (χ_0) is proportional to the staggered susceptibility. Therefore, its temperature/field dependence obeys the scaling law relation [69, 70]. Data were fitted to a Lorentzian
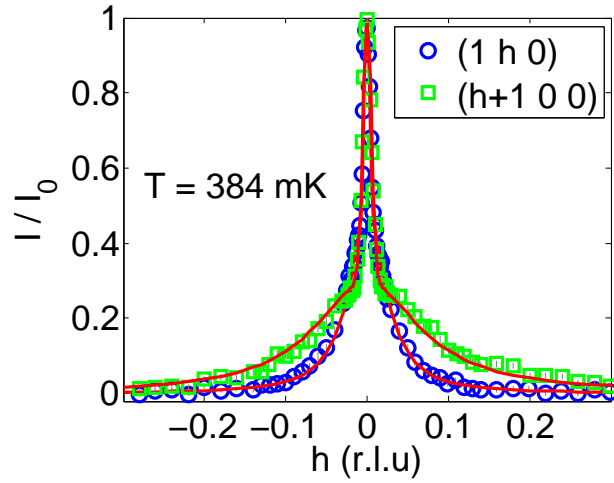
Figure 4.22: Two scans perpendicular to each other at Q=(100). The anisotropy of the critical scattering in the reciprocal space is clear from the Lorentzian widths comparison.

function folded with the resolution of the instrument. Fig. 4.23 presents the example of some fits to (1ξ0) scans at several different temperatures.

The correlation length – the inverse width of the critical scattering – diverges at the phase transition. Hence, the Lorentzian width of the modeled line shape should fall to zero at the critical points. This is followed by the divergence of the susceptibility. This behavior is followed at the same value of temperature/field for I (critical scattering intensity),ξ (correlation length)and χ (susceptibility). As depicted in Fig. 4.24, for $T > T_N$ at zero field the amplitude of the critical fluctuations could be fitted by $I \propto \chi^\gamma$ with $\gamma_b = 0.83 \pm 0.04$ and $\gamma_a = 0.82 \pm 0.04$ for transverse and longitudinal scans, respectively.

Above the transition temperature the spin-spin correlation length follows a power law with transverse and longitudinal exponents equal to $\nu_b = 0.55 \pm 0.05$ and $\nu_a = 0.44 \pm 0.05$, respectively. The difference in the value of the in-plane correlation lengths is related to the planar anisotropy of the critical scattering mentioned earlier. The intrinsic width has a minimum at the transition point, but still doesn't reach the resolution limit of the instrument. The anisotropic nature of the critical scattering and a non–perfect diffuse signal separation could explain the remanent value. Figure 4.25

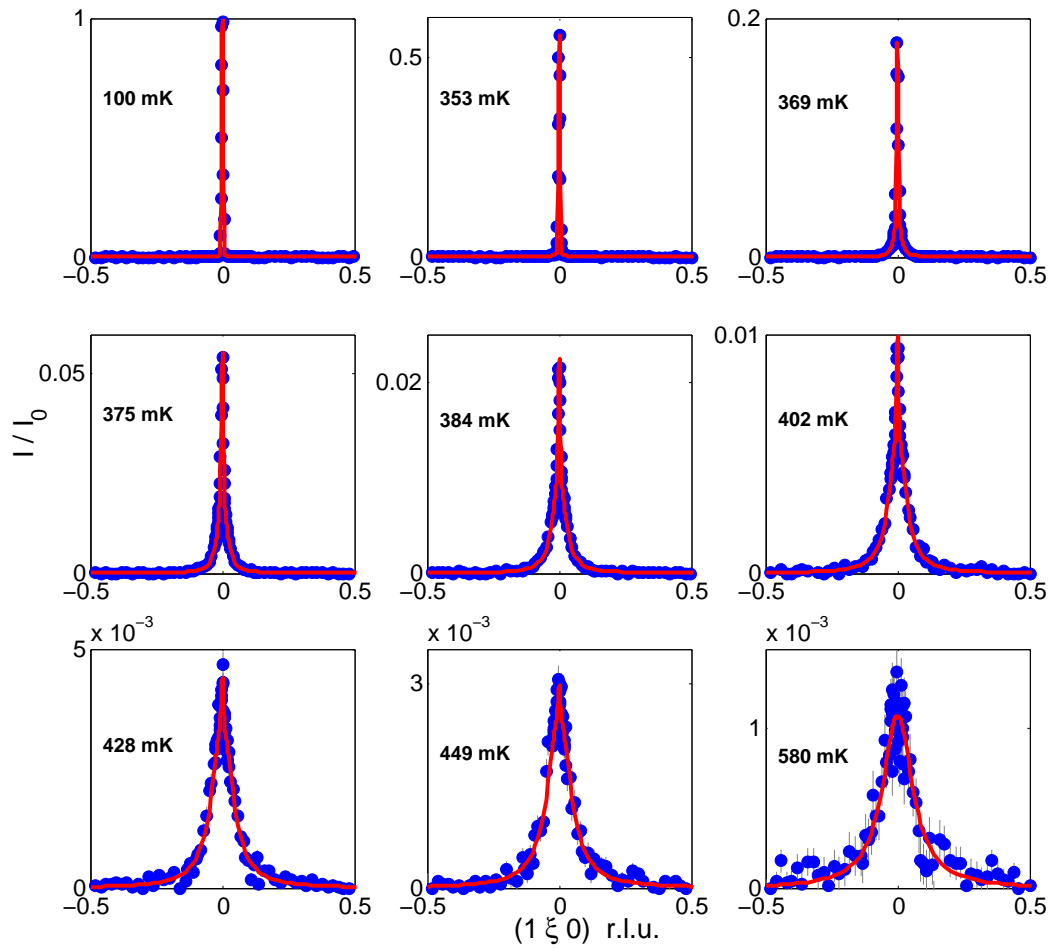Figure 4.23: A series of scans along Q=(1ξ0) at zero field. The evolution of the fits is demonstrated at different temperatures.
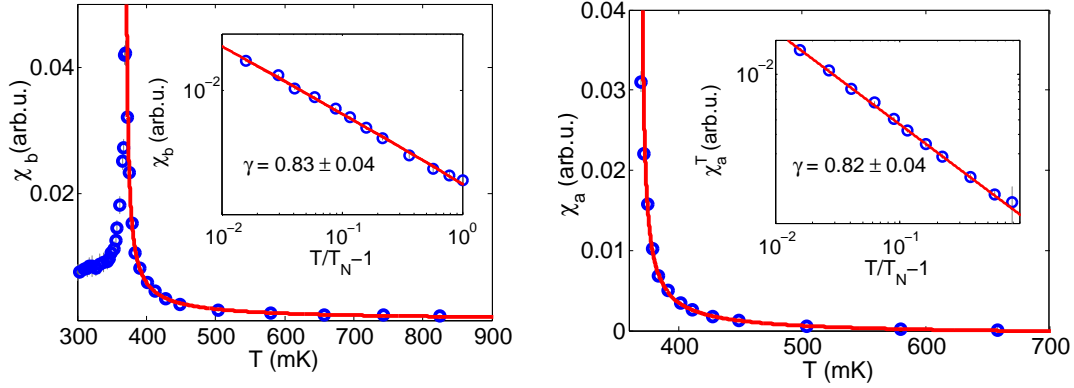
Figure 4.24: Susceptibility (critical scattering amplitude) versus temperature in $(1\xi 0)$ (left), and $(1 + \xi 00)$ (right) scans. The red lines are the power law fit to the curves at $T > T_N$. The insets present the critical exponent extraction in the logarithmic scale.

shows the evolution of the width and correlation length as a function of temperature in both directions. The planar critical exponents of the correlation length at the classical phase transition are compared in Fig. 4.26.

At the base temperature, field scans were performed along Q=$(1\xi 0)$ only. For an unknown reason, field data have lower quality compared to temperature scans with similar statistics. Hence, the uncertainties of the fits are larger. Above H$_c$, the Lorentzian width and intensity – presenting the reciprocal correlation length and susceptibility – obey power–law scaling with $\gamma_b^H = 1.44 \pm 0.2$ and $\nu_b^H = 0.71 \pm 0.04$, respectively (Fig. 4.27).
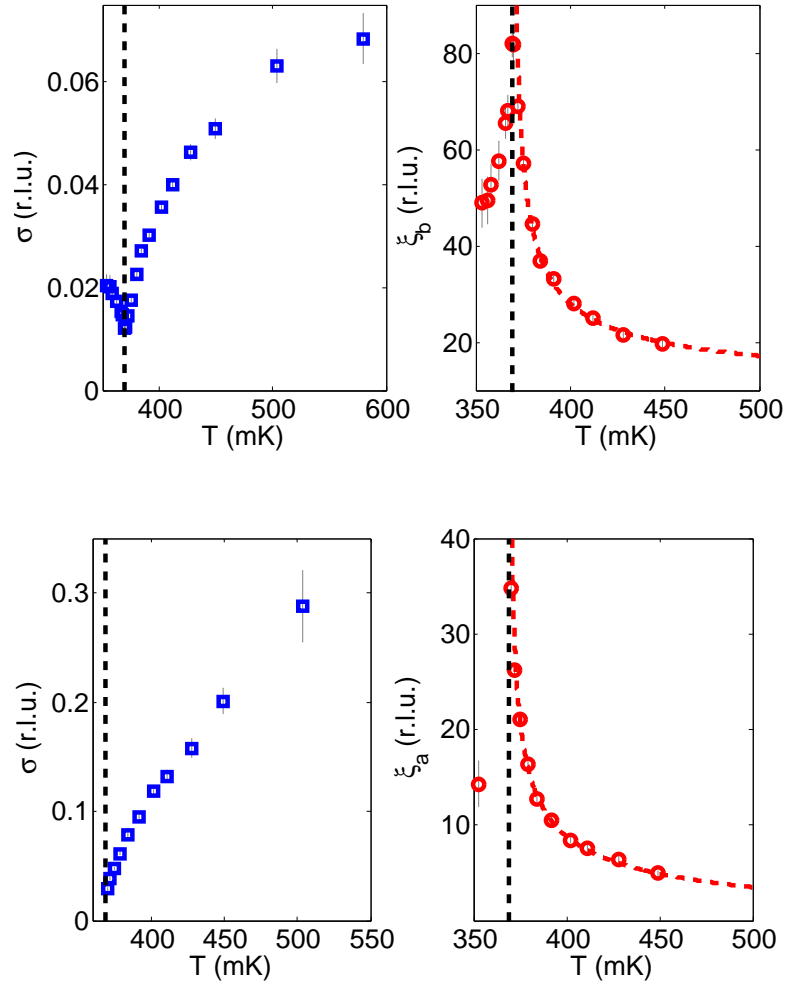
Figure 4.25: Critical scattering width and correlation length versus temperature in Q=(1ξ0) (left), and Q=(1 + ξ00) (right) scans. The red lines are the power law fit to the curves at $T > T_N$.
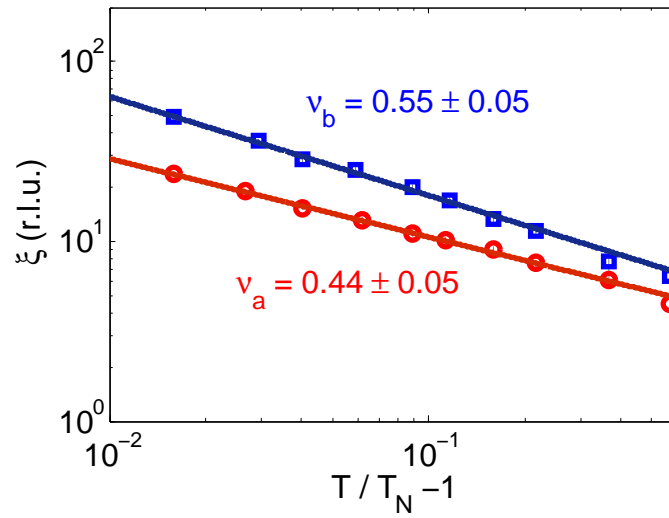
Figure 4.26: The planar critical exponents of the correlation length in the vicinity of the classical phase transition.
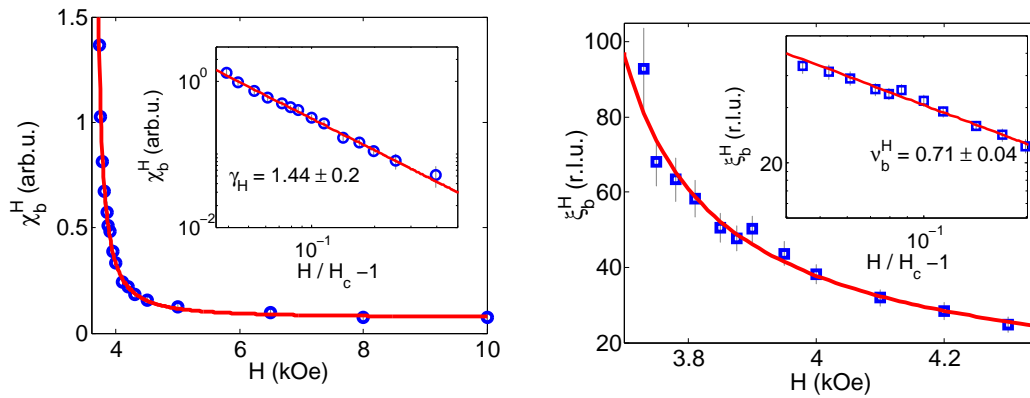
Figure 4.27: Left: The amplitude of the critical scattering versus $H \parallel c$, and the power law fit. Right: The correlation length behavior above H$_c$, and the critical exponent extraction.

4.6.1 Discussion

In section 4.4.1, the critical exponents of the order parameter (β) and specific heat (α), and the nature of both classical and quantum phase transitions were obtained. In the previous section, two other exponents (γ and ν) were extracted. For the thermal phase transition we first compare our results directly to the reported values:

- The estimated h_4 anisotropy in LiErF$_4$ from order-by-disorder phenomena (discussed in 4.4.4) is in the same order of magnitude of the predictions by Taroni *et.al* [55] for $\beta = 0.15$, which is the value obtained in LiErF$_4$.

- The exponent $\alpha = -0.28 \pm 0.04$ for the specific heat is far from the predictions of 3D classes (-0.13 to -0.2). Unfortunately, there is no specific heat report on the the 2D XY/h$_4$ universality class, except for a rough numerical estimate on a square lattice dipolar system with $\alpha = -0.4 \pm 0.2$ [53]. This value, within the errorbar, is consistent to the result obtained for LiErF$_4$.

- The determined h_4 value and β for LiErF$_4$ correspond to $\nu = 1.19$ according to Ref. [55]. This number is far from the here extracted exponents (0.44–0.55) for the correlation length in the *ab*–plane.

- The measured critical exponent for the susceptibility ($\gamma = 0.83 \pm 0.04$) is far from the 2D Ising and 3D models (Table 4.3) [51].

- Finally, our calculated critical exponents (using α, β and scaling relations, assuming d=2) of $\delta = 14.2$ (magnetization) and $\eta = 0.26$ (anomalous dimension for the spatial correlation function) are in agreement with the predictions of the 2D (Ising/XY) models.

Secondly, we can test the internal consistency of the measured parameters against the scaling relations. Let us first consider:

$$2\beta = d\nu - \gamma \tag{4.18}$$

$$\gamma = (2 - \eta)\nu \tag{4.19}$$

From Eq. 4.18, which links the susceptibility and correlation length exponents to β, one can for a fixed β extract ν from γ, and *vice versa*. Using Eq. 4.18, the planar (*ab*) critical exponents for the diffuse scattering amplitude $\gamma_a = 0.82 \pm 0.04$ and $\gamma_b = 0.83 \pm 0.04$ give $\nu_a^{2D} \sim 0.56$ and $\nu_b^{2D} \sim 0.57$ for a 2D system. On the other hand, if one assume $d = 3$, the corresponding exponents for the in-plane correlation length would be $\nu_a^{3D} \sim 0.37$ and $\nu_b^{3D} \sim 0.38$, respectively. Furthermore, the experimental values extracted from the power law fit to inverse width of the critical scattering, are $\nu_a = 0.44 \pm 0.05$ and $\nu_b = 0.55 \pm 0.05$. The comparison of the correlation length exponents extracted from Eq. 4.18 with the values from the experiment (within the errorbars), suggests a 2D–like universality class in LiErF$_4$. This strengthens the previous arguments from the order parameter and specific heat studies. In addition, inserting the obtained values for ν and γ into Eq. 4.19, results in $\eta \simeq 0.36$, which is slightly different from 0.26 extracted earlier (by α and β). It should be noticed that the $\beta/\nu = 1/8$ condition corresponding to a 2D Ising model seems not valid in LiErF$_4$ [55]. Now we continue the inquiries with two other scaling relations:

$$\alpha + 2\beta + \gamma = 2 \tag{4.20}$$
$$\alpha + d\nu = 2. \tag{4.21}$$

Inserting the obtained exponents for α, β and γ in the left hand side of the Eq. 4.20 gives 0.8 instead of 2. The same procedure for Eq. 4.21 results in -1.3 (for d=2) and -0.8 (for d=3). Therefore, it is obvious that the relevant exponents are not consistent with this second set of relations. On the other hand, the Eq. 4.18 is achieved by the combination of the Eqs. 4.20 and 4.21, excluding α from the relation. As mentioned earlier, this equation is satisfied with the extracted values for β, ν and γ for a two dimensional system. Therefore, it is possible that one of the parameters mentioned above is not accurate enough; giving invalidity to some of the scaling relations. Further studies are required to confirm this fact, *e.g.* analysis of the line shape of the scattering function at T$_N$ could verify the value of η experimentally. Table 4.3 summarizes the critical parameters of LiErF$_4$ at T$_N$ and H$_c$. The reported values for the mean-field, 2D Ising and 3D universality classes are also given for comparison.

Table 4.3: Critical exponents comparison: Mean-field, 3D models, 2D/Ising, and LiErF$_4$ (this work).

Exponent	β	γ	ν	η	δ	α
Mean-field	0.5	1	0.5	0	3	0
3D [51]						
Ising	0.32	1.24	0.63	0.04	4.8	0.11
XY	0.35	1.32	0.67	0.04	4.8	-0.01
Heisenberg	0.36	1.39	0.71	0.04	4.8	-0.12
2D						
Ising [54]	0.125	1.75	1	0.25	15	0
XY/h$_4$ [55]	0.1-0.25		1-1.37	0.25	15	
LiErF$_4$ (at T_N)	0.15 (0.02)	0.82 (0.04)	0.44-0.55 (0.05)	0.26	14.2	-0.28 (0.04)
LiErF$_4$ (at H_c)	0.31 (0.02)	1.44 (0.2)	0.71 (0.04)			

Regarding to the QPT at the base temperature the Lorentzian fit to the data satisfies $\nu_b^H = 0.71 \pm 0.04$, which clearly matches with the 3D models–in agreement with the order parameter studies. On the other hand, inserting the extracted exponent for the staggered susceptibility ($\gamma_b^H = 1.44 \pm 0.2$) into Eq. 4.18 results in $\nu^{H,2D} = 1.03$ and $\nu^{H,3D} = 0.69$ for the critical exponents of the correlation length for $d = 2$ and $d = 3$ respectively. Unfortunately, no more exponent at QPT is measured to test other scaling relations.

4.7 Excitation spectrum in LiErF$_4$

The hallmark of a quantum phase transition (QPT) is a concomitant softening of the characteristic excitations. In the case of LiHoF$_4$ the remaining gap around the QCP originated from mixing with the nuclear spins through the hyperfine coupling [3]. In LiErF$_4$ the advantage of the weak hyperfine interaction with $A = 0.43$ μeV, and the fact that only 23% of the natural abundance of Er isotopes carry nuclear spins, result in decreasing the effect in the low–energy excitations. In fact within a resolution of $\simeq 40\mu$eV, a seemingly softening of the electronic excitation at H$_c$ was measured in the previous studies [19], confirming the presence of a QPT in the system. Moreover, the spin bath effect can be switched on and off using the isotopic Er. Here, a full dispersion of the magnetic excitations in the ordered state at H=0 was obtained with the high resolution TOF spectrometer LET at ISIS on two gold sputtered $10 \times 30 \times 1.5$ mm^3 blades of LiErF$_4$ single crystals. The two plates were inserted in parallel – to improve the total cross section – inside a copper sample holder covered with a few μm of gold. The *ac* crystallographic plane was placed in the horizontal scattering plane, and the choice of $E_i = 1.5$ meV provided the resolution of ~ 14 μeV $\approx 1\%$ at the elastic line. The large magnetic moment of the sample ($J = 15/2$) and negligible incoherent scattering resulted in fast data acquisition with satisfactory statistics. The excellent signal and low background allowed the so-called Horace scans, whereby full four dimensional data sets (3 momentum and one energy axis) could be achieved (Fig. 4.28). This provided the possibility to perform many cuts along different reciprocal directions for more quantitative analysis. Because of the limited angular coverage of the detector (60°) at LET, the sample was aligned in such a way that Q=(00-1) magnetic BP (with shorter reciprocal value) was placed at the elastic line, thus providing access to the complete Brillouin zone (BZ) along the *c*-axis. On the other hand, only ±40 % of the BZ could be covered along the *a,b* directions.

4.7.1 Base temperature spectrum

At the selected directions in reciprocal space, the excitations were evaluated by RPA calculation – convoluted with a Gaussian function with a fixed width as an approximation for the instrumental resolution – taking into account the two magnetic domain
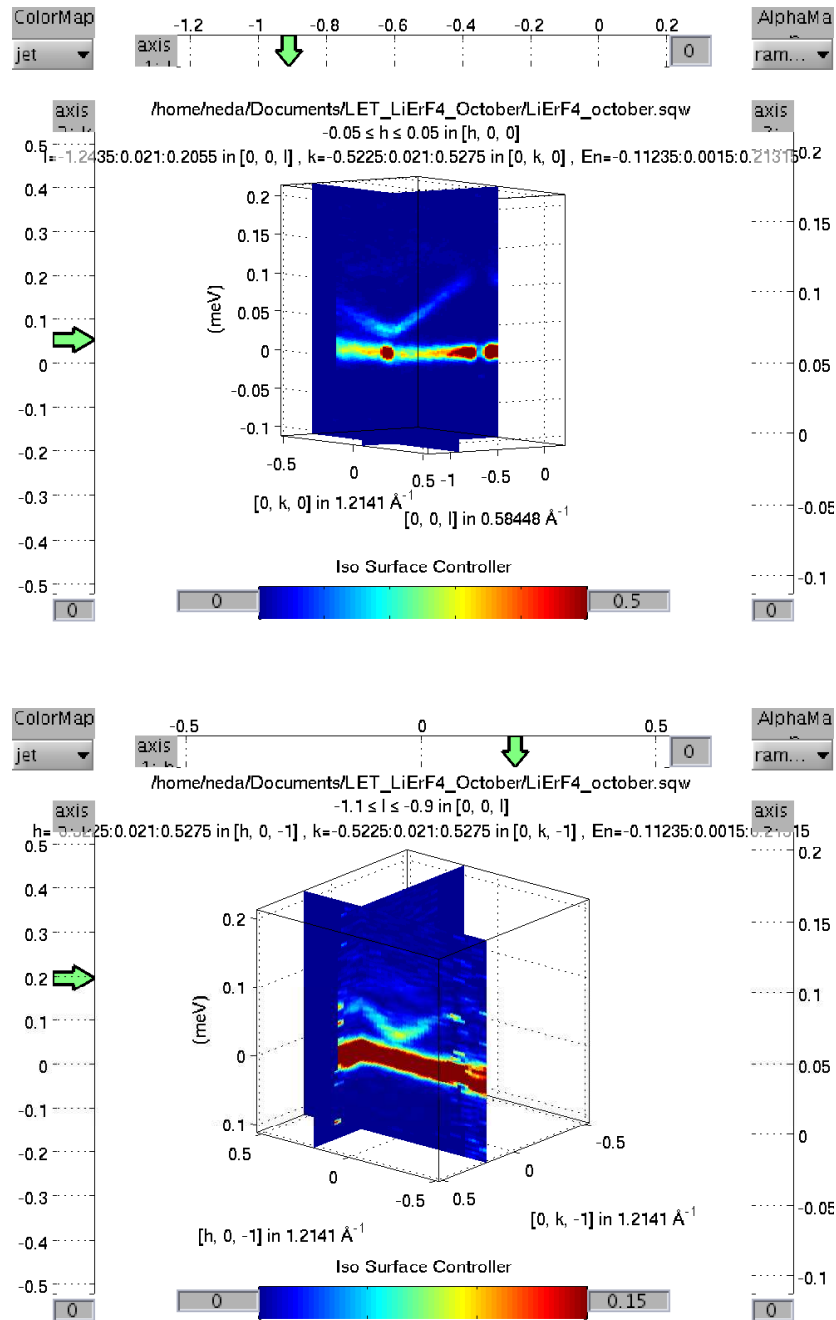
Figure 4.28: Two different 3-dimensional cuts from the 4D-Horace scans performed at LET/ISIS. Top: the in-plane *ac* dispersion. Bottom: the *ab* dispersion (*b* is the out-of-plane component).

structure. Figure 4.29 shows the fits at selected Q points. The red line is the Gaussian fit to the data. The pink and green lines are the RPA calculations originating from two domains, and the black line is the sum of both domain contributions. The good agreement between experiment and calculation confirms the correctly determined magnetic structure of LiErF$_4$, in favor of the two domain model. Figure 4.30 depicts a 2-dimensional view of the excitation spectra obtained by the RPA-MF calculation and experiment along several selected directions.
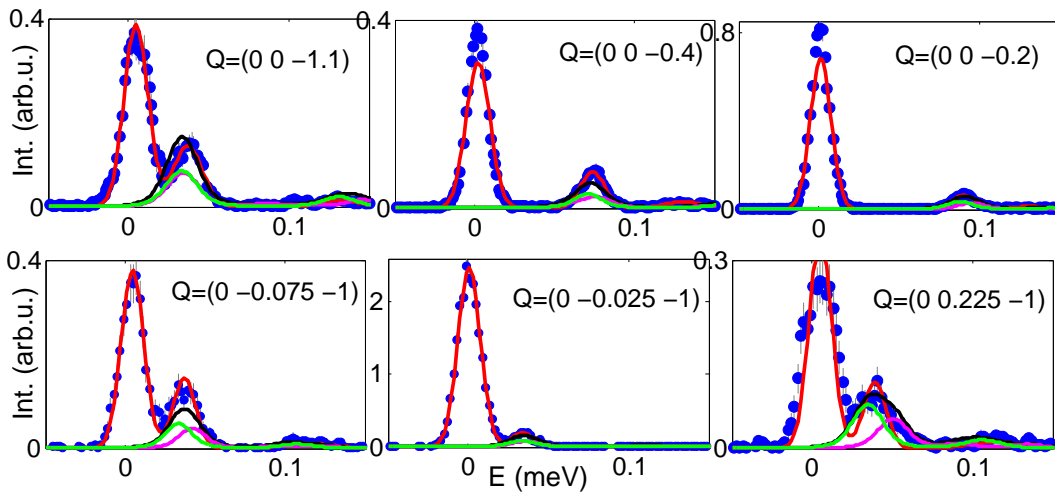
Figure 4.29: Excitations at selected Q points at H=0. The red line is the Gaussian fit to the data. The pink and green lines are the RPA calculations for the two domains, and the black line is a sum of both domain contributions.

Dispersions along Q=(00l), Q=(h0-1) and Q=(0k-1) are presented in Fig. 4.31, which are obtained by fitting the 1D cuts with simple Gaussian functions – folded with a Gaussian function with the fixed width corresponding to the finite instrumental resolution. The spectrum is gapped at the zone center. Fitting to a damped harmonic oscillator model, the RPA calculation could reproduce the correct slope of the excitation spectrum, considering the two-domain structure of the zero-field magnetic lattice in the calculations.

Figure 4.30: The top three panels are the MF-RPA calculation at a selected point in Q space. The left two are the calculations performed for the two domains, and the third is the sum of both. The bottom two panels are the experimental 2D cuts from the Horace scans. The points correspond to the dispersion obtained by the fits to the data.
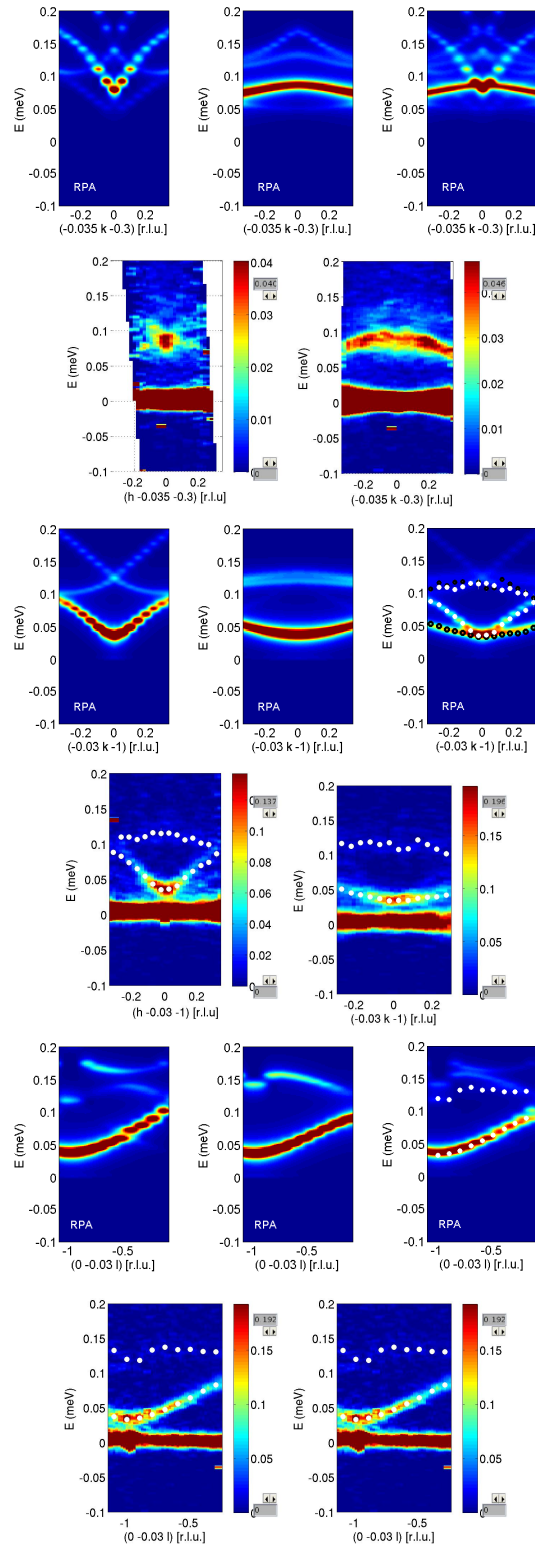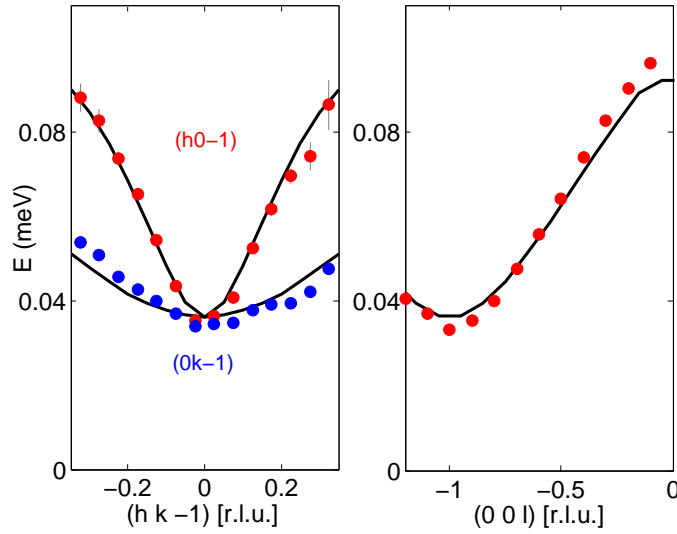
Figure 4.31: Dispersion of the magnetic excitations in LiErF$_4$ at $H = 0$ and $T = 22$ mK. The spectrum is gapped at the zone center Q=(00-1). The black solid curves are the RPA calculations, considering two possible domain structure. RPA is able to reproduce the correct slope of the dispersion.

4.7.2   Excitations at elevated temperatures

As a function of temperature, the excitations soften, and within the instrumental resolution the gap in the dispersion disappears at the thermal phase transition. The energy of the excitations were determined by fitting the data to a Gaussian function folded with instrumental resolution which was modeled by another Gaussian (Fig. 4.32). In addition, the critical scattering diverges when approaching T_N – as presented in Fig. 4.32 – which provides an independent way of transition temperature determination. Interestingly, the RPA calculation does not reproduce the slope of the the gap-versus-temperature curve obtained from the experiment. As Fig. 4.32 displays, RPA predicts a similar value for the measured gap at the base temperature (including hyperfine interaction), whereas at any higher temperatures it underestimates the energy of the excitations. It is clear that the calculated gap has a sharp drop towards 200 mK, where it becomes less steep towards higher temperatures. The upturn disappears when hyperfine effect is neglected in the calculation. As mentioned in 4.4.4, order by disorder phenomena introduce an h_4 anisotropy to the ground state of LiErF$_4$,

which might be the reason for the larger measured energy gap below T_N (except at 22 mK) compared to the RPA predictions. The similar extracted values for the gap at the base temperature from the experiment and RPA theory, might have a physical interpretation or might be only a coincidence, since the calculated curve lies below the measured curve in any other temperature. The reason for the absence of the upturn from the hyperfine interaction (calculated by RPA) in the experiment could be either, in the experiment the sample was not cold enough to show the effect, or MF-RPA overestimates the effect of the hyperfine interaction. It should be noticed that quantum fluctuations are not included in the calculations. In addition, thermal fluctuations have been considered only in the single ion susceptibility calculation. Therefore, the smaller gap of the excitations in theory, could be related to the absence of the fluctuations in the calculation.
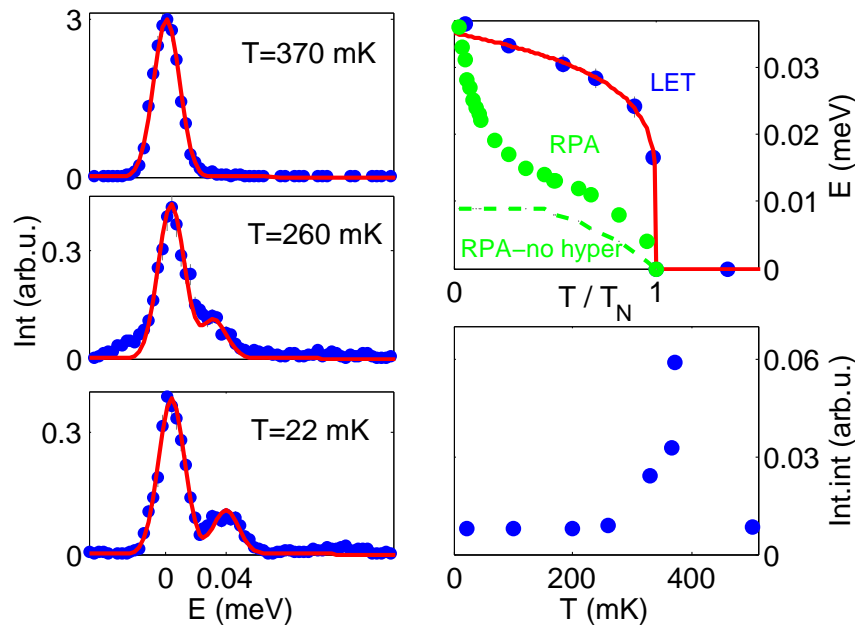
Figure 4.32: Temperature dependence of the inelastic excitation. The gap of the dispersion closes towards T_N, where the scattering intensity diverges. RPA calculation underestimates to value of the gap at all temperatures except at the base. In the dashed line the hyperfine interaction is neglected in the calculation.

4.8   Conclusion

LiErF$_4$ is an example of a XY dipolar AFM. In zero field, it orders at $T_N = 370$ mK through a classical phase transition. A QPT occurs at $H_c = 4$ kOe applied along the crystallographic c-axis. The universality class of the system was investigated by studying the behavior of the order parameter, specific heat, correlation length, and their relevant critical exponents, in the vicinity of the transitions. The thermal phase transition belongs to the 2DXY/h_4 class, whereas the QPT is 3D. The dispersion of the excitation energies is gapped at the high symmetry reciprocal space points, and closes at T_N. The gapped dispersion of the excitations is more likely the combination of order-by-disorder, hyperfine coupling to the nuclear states, and the cf anisotropy.

5 The phase diagram of LiHo$_x$Y$_{1-x}$F$_4$

In this chapter, LiHoF$_4$ and its diluted series with non magnetic Y ions, representing another family member of LiReF$_4$ are partially studied as a side project in continuation of the previous work [19]. The phase diagram is mapped by means of neutron scattering up to 75% dilution of the magnetic sites, and the results are compared with mean-field predictions.

5.1 Introduction

Among the LiReF$_4$ family of compounds, the LiHoF$_4$ Ising dipolar material has attracted many theoretical and experimental efforts. A 50 kOe field ($H_\perp$) transverse to the easy axis introduces quantum fluctuations to the system [6]. The role of hyperfine interactions on the phase diagram of LiHoF$_4$ close to the quantum critical region is discussed in [5, 3]. In fact, the coupling of the $4f$ electronic moments to the nuclear spin bath are larger than both the mean dipole-dipole interaction and the exchange coupling in the vicinity of the QPT. This affects the low temperature boundary of the phase diagram around the critical field ($H_c \approx 50$ kOe). The ability to dilute Ho sites with nonmagnetic Yttrium ions provides a rich arena to explore how disorder and randomness affect the magnetic properties and collective phenomena [3]. The system is ferromagnetically ordered at low temperature (below $T_c \simeq 1.53$ K) above a critical Ho concentration ($x_c \approx 25\%$) [7]. Below x_c, a transition to a spin glass (SG) state has been argued [8] although, some numerical calculations have not found evidence for a SG transition [71, 72]. On the other hand, it has been reported [73] that in LiHo$_x$Y$_{1-x}$F$_4$ a

real spin glass phase can only appear in zero field, and for any other values of $H_\perp$ random fields and quantum fluctuations might obscure the correct interpretation [9, 10, 11, 12]. However, in the less diluted series – which are the subject of this chapter – the random fields are less pronounced to destroy the long range order of the system [56]. In the following, the phase diagram of the diluted LiHo$_x$Y$_{1-x}$F$_4$($0.25 \le x \le 1$) obtained by MF calculation is presented. The results are then compared with the neutron scattering measurements on the same concentrations. The observed discrepancies and the probable reasons for that are discussed afterwards.

5.2 Phase diagram studies by MF calculations

As mentioned in 2.2, the total Hamiltonian describing the system includes five terms:

$$
\begin{aligned}
\mathcal{H} &= \mathcal{H}_{CF} + \mathcal{H}_{hyp} + \mathcal{H}_z + \mathcal{H}_D + \mathcal{H}_{ex} \\
&= \sum_i \left[\mathcal{H}_{CF}(\mathbf{J}_i) + A\mathbf{J}_i \cdot \mathbf{I}_i - g\mu_B \mathbf{J}_i.\mathbf{H} \right] \\
&\quad - \frac{1}{2} \sum_{ij} \sum_{\alpha\beta} \mathcal{J}_D \overline{\overline{D}}_{\alpha\beta} \mathbf{J}_{i\alpha} \mathbf{J}_{j\beta} - \frac{1}{2} \sum_{ij,n.n.} \mathcal{J}_{ex} \mathbf{J}_i \cdot \mathbf{J}_j
\end{aligned}
\tag{5.1}
$$

Recalling, $\mathcal{H}_{CF}$ is the crystal field, $\mathcal{H}_{hyp}$ the hyperfine coupling to the nuclear spins, $\mathcal{H}_z$ the Zeeman term, $\mathcal{H}_D$ the dominant dipolar interaction, and $\mathcal{H}_{ex}$ the nearest neighbors Heisenberg exchange interaction. $J = 8$ and $I = 7/2$ correspond to electronic and nuclear angular momentums, respectively. The Landé factor parameter (g) in Zeeman term is 5/4. $A = 3.361$ μeV is the hyperfine coupling constant reported from hyperfine resonance [17] and specific heat measurements [15]. The full rare earth Hamiltonian was diagonalized through the Virtual-Crystal-Mean-Field (VCMF) approximation, mentioned in 2.6; hence, the phase diagram of LiHo$_x$Y$_{1-x}$F$_4$ could be mapped qualitatively. The exchange coupling in the calculation was fixed to $J_{ex} = 0.1$ μeV. The crystal field parameters are those reported in reference [5], except for $B_6^4(s)$ which is a fine–tuning parameter. Instead, $B_6^4(s) = 6$ μeV value obtained by fitting the crystal field energy levels was used. It should be noticed that tuning the $B_6^4(s)$ parameter only alters the value of H_c, and no change occurs in the overall behavior of the phase diagram. Normalizing the effective length of the local magnetic moments along the z-axis (J_z) by a factor (0.785), gives H$_{c(MF)}^{x=1} \simeq 53$kOe which is close

to the critical field extracted from the neutron scattering measurements. Since the aim of this work is to distinguish the difference between the phase diagrams extracted from MF predictions and experimental observations (to understand the physics conducting the system), this scaling is useful when comparing the phase boundaries.

The phase diagram of five different Ho concentrations of $LiHo_xY_{1-x}F_4$ $0.25 \leq x \leq 1$ was calculated, assuming the samples have a spherical shape. Periodic boundaries were taken into account, and the long range interactions were limited to a fixed radius threshold. The results are shown in Fig. 5.1. The dashed lines represent the calculations neglecting the hyperfine interaction.
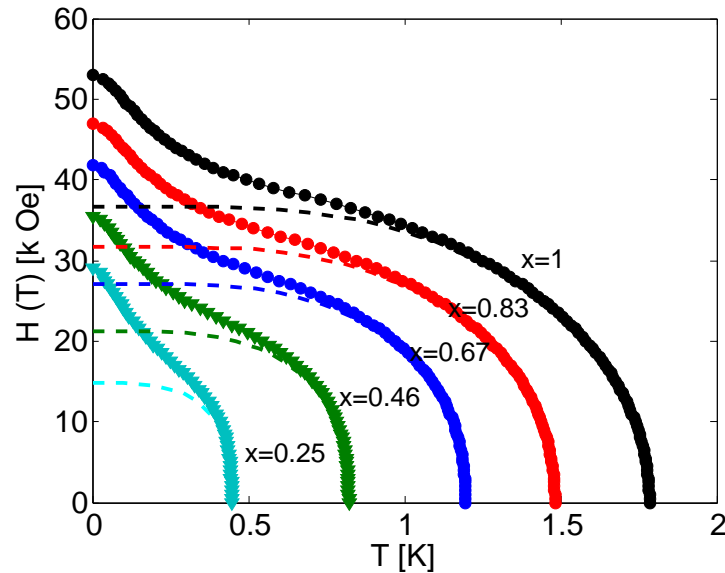
Figure 5.1: T-H phase diagram of $LiHo_xY_{1-x}F_4 (0.25 \leq x \leq 1)$ calculated by VCMF. The dashed lines are the calculation without the hyperfine interaction.

5.3 Phase diagram studies by neutron scattering

The T-H phase diagrams of five compounds from $LiHo_xY_{1-x}F_4$ family with $0.25 \leq x \leq 1$ in transverse fields ($H_\perp$) to the easy axis, have been mapped using neutron diffraction [19]. The resolution limited Bragg peaks at $Q = (200)$ reflection indicated true long range ferromagnetic order in all samples in temperature scans in zero field. The

extracted Curie temperatures (T_c) were in agreement with the susceptibility results reported earlier [74]. Down to 46% dilution, the observed linear suppression of T_c by doping satisfies the predictions of the mean field theory ($T_c(x) = x \cdot T_c(x = 1)$), as presented in Fig. 5.2.

Figure 5.2: The Phase diagram of LiHo$_x$Y$_{1-x}$F$_4$versus x [19]. The measured T_c by means of neutron scattering is in accordance with the susceptibility data from [74]. The squares are the VCMF predictions of T$_c$ for the mentioned concentrations.
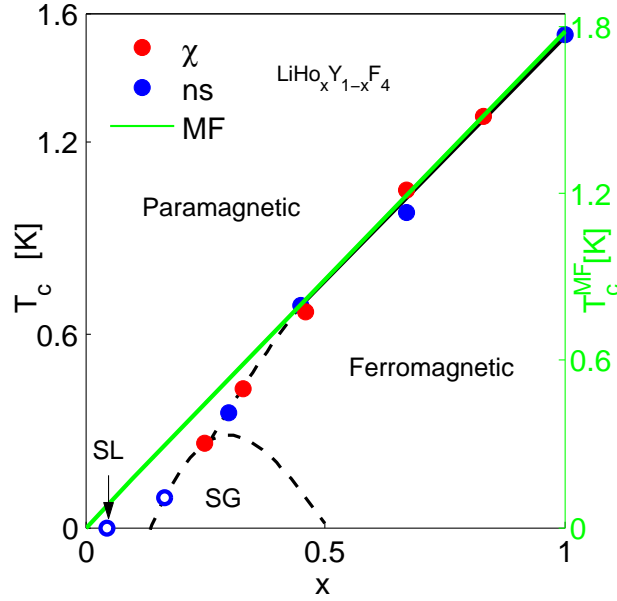
In addition, the transverse field measurements, in which the samples were cooled in zero field (ZFC) down to the base temperature (T $\approx$ 120 mK), also revealed the long range ordering (LRO) transition in all samples, through the sharp BP having the resolution limited width. The intensities of the (200) BP, which is proportional to the order parameter squared, versus H at the base temperature is depicted in Fig. 5.3 for the measured concentrations. The transverse scans through $Q = (200)$ at each point in field were extended in reciprocal space such that the diffuse component as well as the Bragg scattering was covered. As a model to fit the data a Gaussian (with a fixed width corresponding to the finite instrumental resolution) plus a Lorentzian was considered. The enhancement of the critical scattering for $x \leq 0.46$ is obvious from the graph.

The critical scattering was subtracted from the curves, to facilitate the order parameter
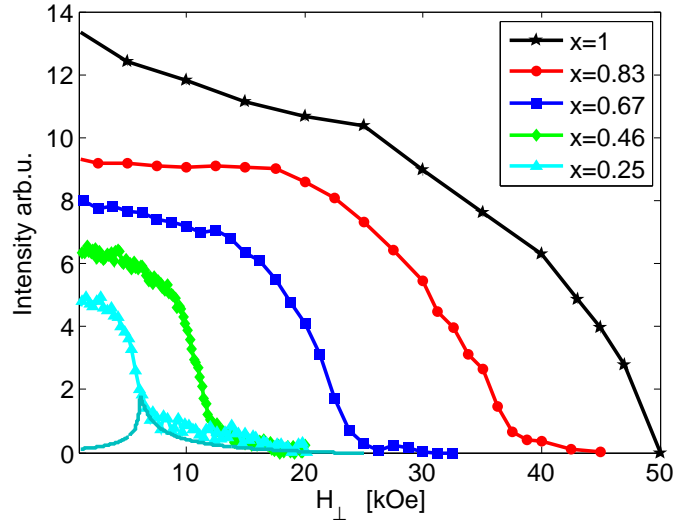
Figure 5.3: The intensity of the (200) Bragg peak versus $H_\perp$ in LiHo$_x$Y$_{1-x}$F$_4$ (0.25 ≤ x ≤ 1) at the base temperature. The line in cyan is the critical scattering of the x=0.25 sample, which was subtracted from the data for critical exponent studies.

comparison. Fig. 5.4 compares the order parameter of the measured samples versus field at base temperature, where the curves are scaled with their corresponding H$_c$ values. Indeed similar behavior of the order parameter is observable from the plot.

The extracted critical exponents of the order parameter from power law fits to the Bragg peak intensity in the critical regimes are in good agreement with the values reported for the pure compound ($x = 1$), in the vicinity of both thermal and quantum phase transitions. For the quantum phase transition, $\beta_H = 0.47 \pm 0.02$ is close to the mean field exponent $\beta_{MF} = 0.5$, whereas $\beta_T = 0.32 \pm 0.02$ for the thermal phase transition at T_c is lower and is consistent with $\beta_{3D} = 1/3$ of the 3D-Ising model. This interesting outcome indicates that the criticality is not affected by dilutions up to 75%. Fig. 5.5 presents a comparison between the $x = 0.46$ and $x = 1$ concentrations. However, the conclusion drawn from the susceptibility measurements on $x = 0.44$ concentration [75] is in contradiction to the neutron results. There, the internal random fields are considered to be responsible for the phase transition, and a different exponent in the thermal regime is reported. More experimental investigations to understand the reasons for this discrepancy are of interest.

The temperature–field phase diagram of LiHo$_x$Y$_{1-x}$F$_4$ obtained by neutron scattering

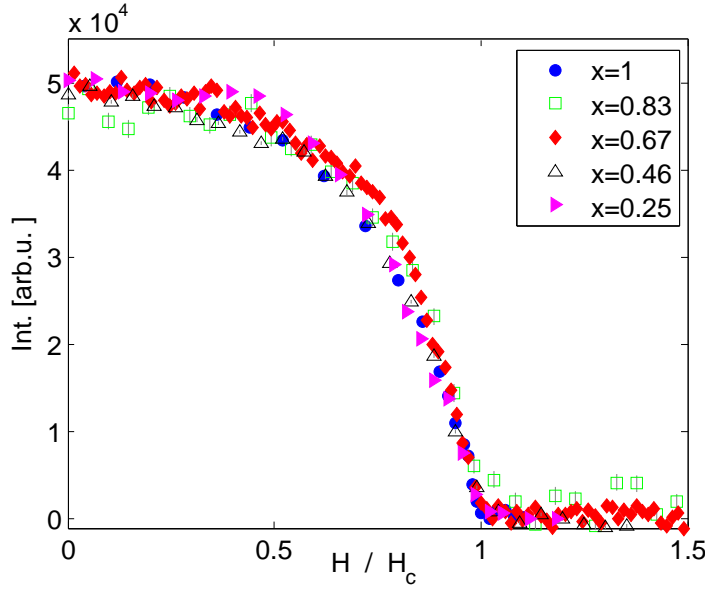Figure 5.4: The behavior of the order parameter versus field at base temperature for LiHo$_x$Y$_{1-x}$F$_4$ (0.25 ≤ x ≤ 1) are identical.

is depicted in Fig. 5.6. The extracted curves from the MF calculation are added to the plot, while have been scaled such the field axis match the low temperature range of the experimental data. This improves the comparison of the phase boundaries, and helps for the zero temperature H$_c$ extraction. The scaling factor increases from 1 for the pure compound to about 4 for the x = 0.25 sample, which shows the faster critical field reduction in the experiment compared to the MF calculation. The feature is more pronounced when normalizing the field and temperature in the phase diagram by the associated predicted mean field values (see Fig. 5.7).

The transition field $H_{c\perp}$ decreases from ~ 50 kOe for the Ho concentration of 100% to ~ 7 kOe for x=0.25, which is much faster than the mean field prediction (Fig. 5.8). The hyperfine interaction seems less crucial at ~ $T_c/2$, therefore, the field values at this temperature could be compared with the critical fields extracted by MF calculation neglecting the hyperfine effect. The difference in $H_{c(\text{MF})}^{\text{with-hyperfine}} - H_{c(\text{MF})}^{\text{without-hyperfine}}$ is almost constant, because hyperfine term has been included in the single ion Hamiltonian, hence, it is not x dependent. On the other hand, $H_{c(\text{exp})}^{\text{with-hyperfine}} - H_{c(\text{exp})}^{\text{without-hyperfine}}$ decreases from x=1 to x=0.46, where it be-

94
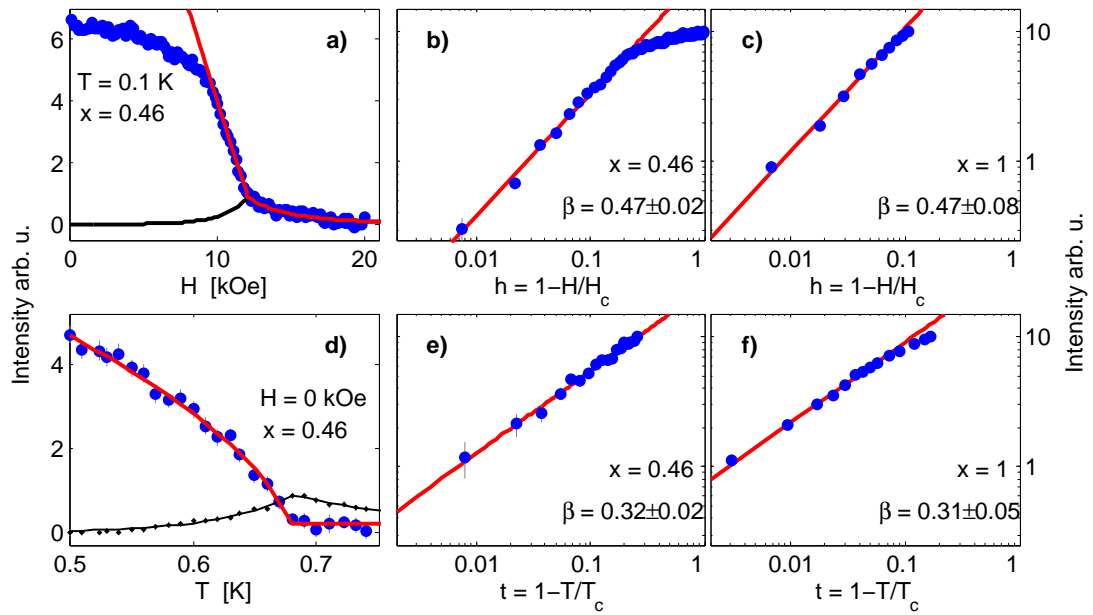
Figure 5.5: Intensity of the magnetic Bragg peak (200) around the phase transition in LiHo$_x$Y$_{1-x}$F$_4$, $x = 0.46$ compared with $x = 1$. The signal originating from critical scattering is indicated by the black curve in (a,d) and was subtracted for further analysis (b,c,e,f). The critical exponents of the magnetization in the diluted and pure compounds are identical [19].
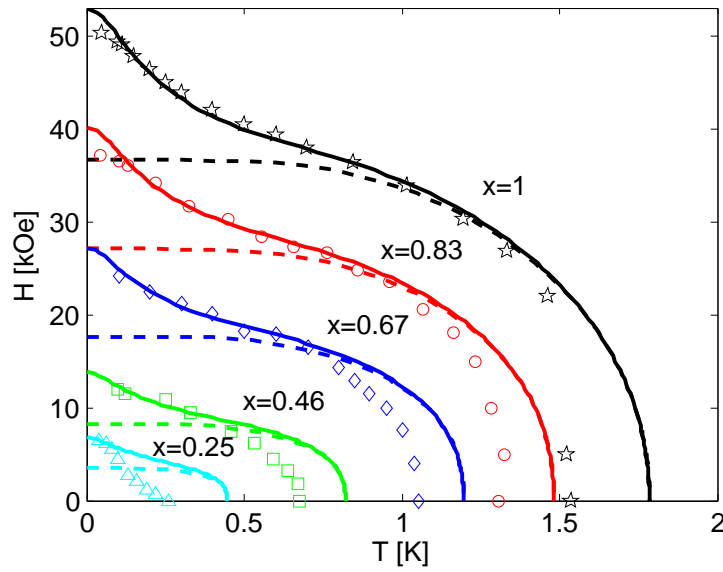
Figure 5.6: Phase diagram of LiHo$_x$Y$_{1-x}$F$_4$($0.25 \leq x \leq 0.83$) from neutron diffraction (symbols). The data for $x = 1$ are adapted from AC-susceptibility measurements by [50], which show a clean phase boundary at low temperatures. The solid (dashed) lines are the VCMF calculation with (without) hyperfine interaction.
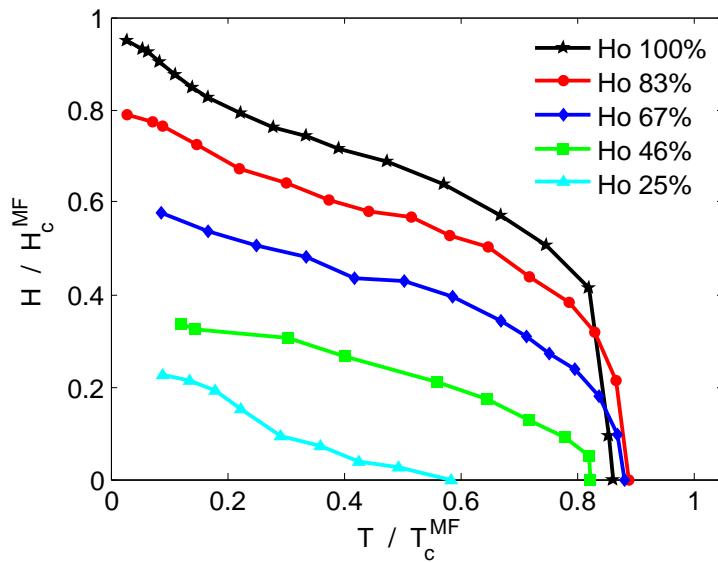
Figure 5.7: The phase diagram of LiHo$_x$Y$_{1-x}$F$_4$($0.25 \leq x \leq 1$) obtained from neutron diffraction scaled by T_c and H_c values predicted for each concentration.

comes almost constant below this concentration. Therefore, hyperfine effect decreases at lower Ho concentrations.
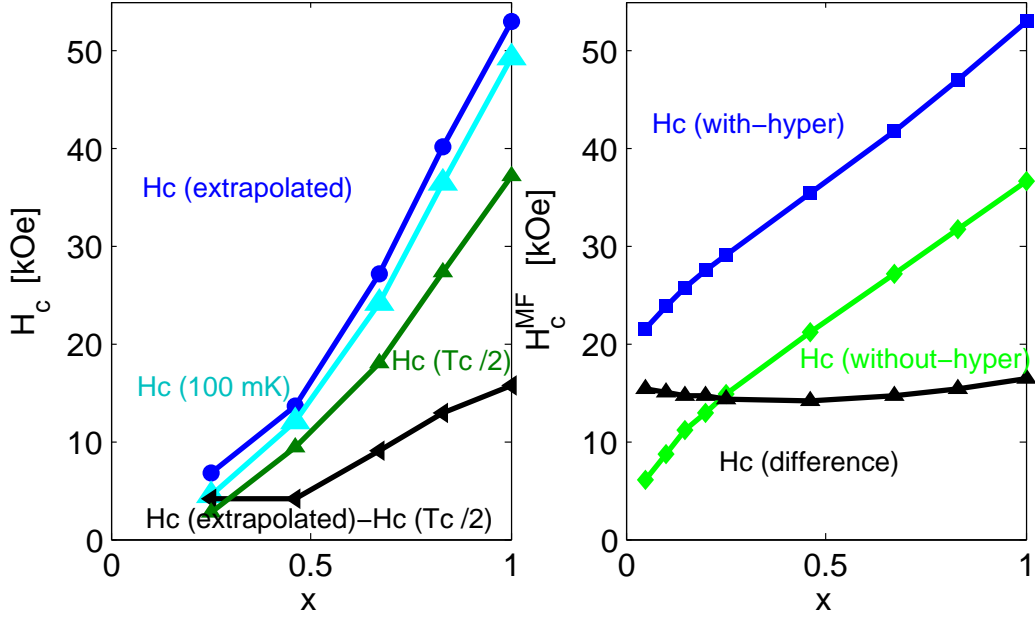
Figure 5.8: Left: H_c-x for LiHo$_x$Y$_{1-x}$F$_4$ ($0.25 \leq x \leq 1$) obtained from neutron scattering. The H$_c$ values at zero temperature are obtained by scaling the MF curve to match the low temperature part of the experimental curves. The values are compared with the experimental H$_c$ at 100 mK. The curves have similar tendencies. At $T_c/2$ the hyperfine effect seems less severe. Hence, $H_{c(\text{exp})}^{\text{with-hyperfine}} - H_{c(\text{exp})}^{\text{without-hyperfine}}$ could demonstrate the decrease of the hyperfine effect at lower Ho concentrations. Right: The calculations have been performed via MF approximation for comparison. The faster experimental H$_c$ suppression compared to MF is observed.

The reason for the faster reduction of H$_c$ in the experiment comparing to MF calculation could be disorder and quantum fluctuations, which are neglected in the theory. It has been argued [61] that through dilution, the off diagonal terms of the dipolar interactions, which are in principle canceled by symmetry in the pure LiHoF$_4$ compound, are no longer absent in diluted systems. These terms introduce both local effective longitudinal interactions and a fluctuating term in the transverse direction. As a result, the effective transverse field is enhanced, which reduces the critical field of the transition.

5.4 Discussion

For proper understanding of the physics of the LiHo$_x$Y$_{1-x}$F$_4$ system, we shall compare our results with theoretical studies. The classical random field Ising model (CRFIM), which has been widely studied [76], can describe the system in the low transverse field region where the quantum fluctuations are negligible. By increasing the applied transverse field, the quantum tunneling between the Ising GS doublets will introduce fluctuations and randomness to the system. To clarify the observations, one can rewrite the Hamiltonian inspired from ref.[77]:

$$\mathcal{H} = \sum_{ij} V_{ij}^{zz} \sigma_i^z \sigma_j^z + \sum_{ij} V_{ij}^{zx} \sigma_i^z \sigma_j^x + \sum_i \gamma_i \sigma_i^z + \Gamma \sum_i \sigma_i^x, \tag{5.2}$$

Where V_{ij}^{zz} and V_{ij}^{zx} are the strength of longitudinal and transverse dipolar interactions, respectively. Transverse interactions, which are induced from interplay between off diagonal interactions and applied transverse field, add an additional term to the effective $H_\perp$, and reduce the expected critical field. σ_i is the Pauli operator and γ_i denotes the effective local random field. The term Γ defines the effective transverse field. In fact, one could describe the local randomness as domain walls, which are pinned by the weak transverse fields at elevated temperatures close to T_c. When $H_\perp$ increases, it induces tunneling between the domains and breaks their localization. Hence, QF gain importance and the transition to paramagnetic (PM) state occurs [78]. The result of QF and random field enhancement is the H_c suppression. This argument is in agreement with the observed increase of the scaling factor (and faster critical field reduction) with dilution when comparing the related MF and neutron scattering phase diagrams. On the other hand, because the transverse dipolar interactions are weaker for the more diluted samples, their role in enhancing the effective transverse field is less crucial than in higher Ho concentrations. This could explain the results for $x = 0.25$, where the experiment (Fig. 5.8) shows a more moderate critical field suppression versus x, and a sudden change in the slope of the curve occurs reaching the 25% concentration. This feature have been argued by Schechter *et al.* [11], where the minimum in $H_{c\perp}$ reduction by x in the presence of off diagonal interactions is discussed.

5.5 Conclusion

Neutron scattering studies of $LiHo_xY_{1-x}F_4$ could confirm the presence of QPT in the range ($0.25 \leq x \leq 1$). The calculated phase diagram of the measured concentrations by MF could provide a quantitative comparison between experiment and theory. The transverse field, randomness, and off diagonal dipolar interactions play important role on the $LiHo_xY_{1-x}F_4$ phase diagram properties, which neglecting them show significant effect especially close to QCP, where quantum fluctuations are present.

6 Conclusions

The LiReF$_4$ family of compounds, where Re stands for a rare-earth element, provide a wide arena to explore fundamental questions in many body correlated physics such as quantum entanglement, collective phenomena, classical and quantum phase transitions (QPT). In fact, the simple and well-understood Hamiltonian of the system makes it a suitable candidate for theoretical advances, providing a guide for experimental studies.

LiHoF$_4$, the Ising ferromagnetic member of the family has attracted significant experimental efforts, being a realization of the experimentally accessible transverse–field–induced QPT. Hyperfine interaction strongly influences the phase diagram at low temperatures around the QCP, and leads to a considerable increase of H$_c$.

It was studied that dilution with nonmagnetic Yttrium ions induces randomness to the system, which eventually destroys the ferromagnetic order below a marginal Ho concentration, as a result of the interplay of the off–diagonal terms in dipolar interactions and the applied transverse field. By means of neutron scattering experiments here we observed that above the critical doping ($x \simeq 0.25$), the long–ranged ferromagnetic state survives in LiHo$_x$Y$_{1-x}$F$_4$, where the order parameter and the related critical exponents around both thermal and quantum critical regimes behave as in the pure ($x = 1$) compound. The faster suppression of the critical field comparing to the mean–field approximation was quantified. The decrease of the hyperfine effect by dilution could be observed from comparison of the experimental critical fields at base temperature and $T_c/2$.

LiErF$_4$ is a XY AFM member of LiReF$_4$ family, exhibiting a pronounced XY-anisotropy

with $g_\perp / g_\parallel \simeq 3.7$. The small hyperfine coupling ($A \simeq 0.5\ \mu$eV) of the naturally occurring Er (with only 23% nuclear spins), and the advantage of nuclear-spin-free existence of ^{168}Er stable isotope weaken the effect of spin bath in this system, as confirmed by AC-susceptibility and neutron scattering measurements of the phase diagram. Critical exponents obtained from specific and order parameter, together with the relevant scaling relations, suggest 2DXY/h_4 universality class behavior of the thermal phase transition. The critical exponents of the correlation length and staggered susceptibility were extracted from diffuse neutron scattering measurements. However, they appear to be different from the predictions of 2D Ising and 3D models. Furthermore, the 3D nature of the system at the quantum critical regime is in accordance with the expected additional dimension when presenting a QPT within a classical picture. The h_4 anisotropy has its major origin in order–by–disorder phenomena by quantum fluctuations. This is in agreement with the considerable deviation of the critical temperature and critical field from MF predictions. The softening of the characteristic electronic excitations at the critical field highlights the QPT nature of the low temperature transition, which could not be observed in *e.g.* LiHoF$_4$ with the larger hyperfine effect. The excitations were measured using new high–resolution TOF instrument LET. The full dispersion obtained at the base temperature could be reproduced by random phase approximation (RPA). The observed gap of $\sim 30\ \mu$eV softens as a function of temperature and closes at T$_N$. RPA underestimates the value of the gap, which could be due to the absence of the fluctuations in the theory.

7 Outlook

Comparing to *e.g.* $LiHoF_4$ and its diluted series, $LiErF_4$ has not been explored much. Therefore, with respect to the interesting results obtained within this thesis, the field is open for various exciting theoretical and experimental advances. As a future project a complementary correlation length measurements along the *c*-axis in the vicinity of both thermal and quantum regimes is suggested. In accordance with the $2DXY/h_4$ behavior of the system weaker magnetic correlations are expected in out–of–plane direction. In addition, specific heat investigations around QCP could further confirm the classical 3D universality class of the system. A continuation study of the excitations in the presence of an applied magnetic field along the *c*-axis is planned on the LET spectrometer. The good resolution of the instrument allows to verify the so called ω/T scaling through the measurements at H_c at the base temperature and several elevated temperatures similar to the previous study of CaCuAu [79] except with the advantage that the microscopic Hamiltonian is completely determined here. In addition, a complete 4-dimensional (Horace) scan at T_N could shed light on the possibility for the dimensional reduction phenomena. To further test the effect of disorder and randomness, an enhancement of off-diagonal terms via substitution of Ho for Er ions is expected. An added benefit of Er is the existence of isotopes with and without nuclear spins, allowing comparative exploration of decoherence and mixing effects. Interestingly, the recently produced nano-crystals of $LiReF_4$ [80], could open a field to investigate the magnetic structures at lower dimensions. The 2D dipolar-coupled behavior of the system could have a rather far application in producing nanomagnetic arrays for ultra-high-density magnetic storage technology [1, 2].

A Correlation length studies of LiErF$_4$ along c-axis

As mentioned in 4.6, due to several uncertainties from the experimental point of view, the measurements along the crystallographic c-axis are presented in the appendix. Field measurements were performed at IN14 cold TAS at ILL. A single piece of LiErF$_4$ crystal with $5 \times 5 \times 20$ mm^3 dimension, covered with gold, aligned with ac in the horizontal scattering plane. A horizontal magnet was used to apply the magnetic field along the crystallographic c-axis. longitudinal scans performed along Q=(00-3) magnetic reflection. The selected $k_i = k_f = 1.54$ Å^{-1} in open configuration provided a resolution of 0.01 Å^{-1}, which was not perfect for the weak diffuse scattering separation from the intense magnetic BP around H$_c$. Within the last couple of days of the experiment, three tight 20$'$ collimators were inserted between the monocromator-BE filter, sample-analyzer, and analyzer-detector. This configuration together with the choice of $k_i = k_f = 1.35$Å^{-1} provided $\delta Q = 0.003$ Å^{-1}, which reduced the statistics by a factor of three. Therefore, the time was not sufficient to get enough points. In addition, due to the fact that the quality of the field scans is worse than temperature scans, good statistics are required to obtain smooth curves, that helps for more accurate fits and analysis. However, some preliminary analysis which might be helpful for the the further planned experiments are shown in fig. A.1. A resolution corrected sum of a Gaussian and a Lorentzian functions, used as a model to fit the data.

Temperature studies at zero field carried on 4F1 triple axis spectrometer /LLB. The measurement performed on the similar sample as IN14 experiment, keeping the same configuration for the alignment, k_i, and collimations. Critical scattering along c-axis was measured through transverse scans to Q=(100) magnetic BP. The best fit to the

Appendix A. Correlation length studies of LiErF$_4$ along *c*-axis
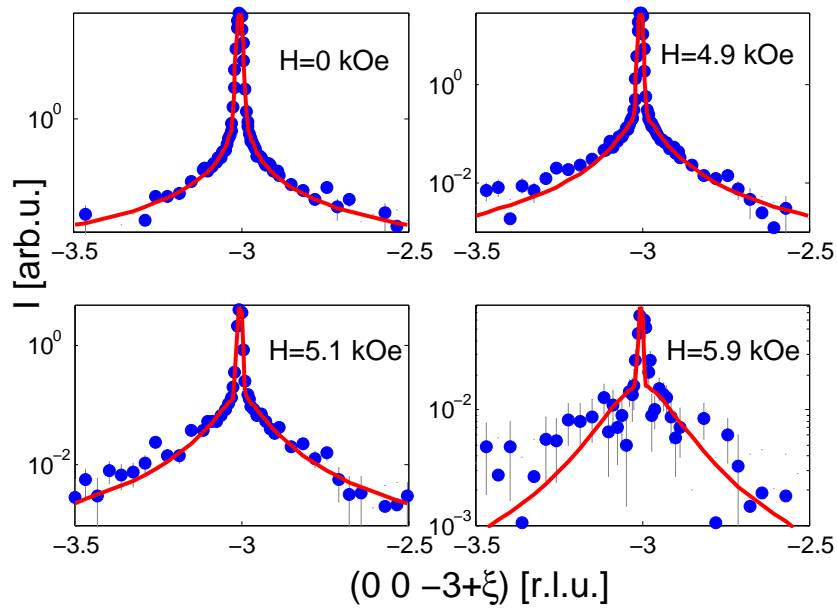
Figure A.1: Fits to Q=(00ξ) at zero field and few fields in the vicinity of H$_c$ at collimated configuration.

data obtained by summation of two Voigt functions, which the lorentzian width of one of the Voigt components appeared temperature independent (most probably having back ground origin), and kept fixed for further analysis. Fig. A.2 presents a series of scans along Q=(10ξ) below and above T_N = 375 mK. The not perfect fit at T_N could mean that critical scattering at the transition point is not described by a pure Lorentzian model. Moreover, the model is working well to fit the data above the transition. Unfortunately, a sudden failure happened on performance of the thermometer during the experiment, which means the exact temperature of the sample was not known. This doubt on the actual value of T, doesn't allow any further analysis. Based on the above statements, no subtle argument can be given on the measurements along the *c*-axis –due to the mentioned experimental uncertainties. Therefore, more experiments are planned for further studies.

Figure A.2: A series of scans along Q=(10ξ) at zero field. The evolution of the fits is demonstrated at different temperatures.

B h_4 anisotropy and universality class

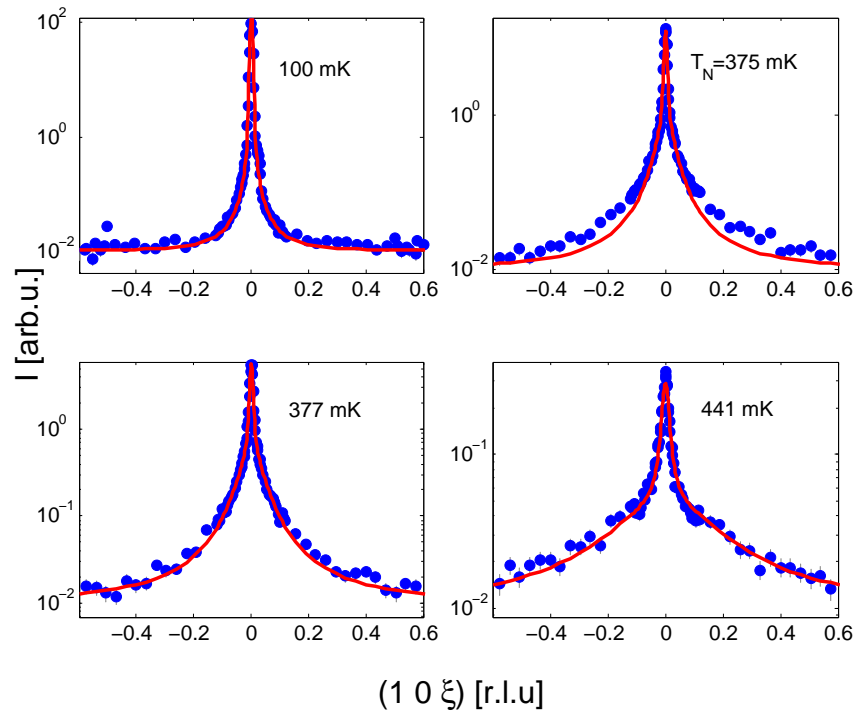Here we estimate the h_4 anisotropy in LiErF$_4$ and compare to the 2D universal window for critical exponents calculated by A. Taroni *et al.* in the generic case of the clock model [55]. The clock model

$$\mathcal{H}_{\text{clock}} = -\mathcal{J}_{\text{clock}} \sum_{\langle i,j \rangle} \cos(\theta_{\text{i}} - \theta_{\text{j}}) - h_4 \sum_{\text{i}} \cos(4\theta) \tag{B.1}$$

is equivalent to the classical spin Hamiltonian with $\mathbf{S}_i = (\cos(\theta_{\text{i}}), \sin(\theta_{\text{i}}), 0)$:

$$\mathcal{H}_{\text{clock}} = -\mathcal{J}_{\text{clock}} \sum_{\langle i,j \rangle} \mathbf{S}_i \cdot \mathbf{S}_j - h_4 \sum_{i} (S_i^{x4} + S_j^{y4} - 6S_i^{x2} S_i^{y2}). \tag{B.2}$$

To compare with our system, we write both the clock model and LiErF$_4$ Hamiltonians in the mean field approximation with, in the case of LiErF$_4$, $\mathbf{J}_i = j_{xy}\mathbf{S}_i$ where $j_{xy} = |\langle d|J^x|d \rangle| = 3.28$, $|d\rangle$ being one of the states from the lowest-energy crystal-field doublet.

$$\mathcal{H}_{\text{clock}}^{\text{MF}} = \sum_i \mathbf{S}_i \cdot \mathbf{H}_{\text{clock}}^{\text{MF}} - h_4 \sum_i (S_i^{x4} + S_J^{y4} - 6S_i^{x2} S_i^{y2}) \tag{B.3}$$

$$\mathcal{H}_{\text{Er}}^{\text{MF}} = \sum_n \mathbf{S}_n \cdot \mathbf{H}_{\text{Er,n}}^{\text{MF}} + \mathcal{H}_{CF} \tag{B.4}$$

with n indexing the sites within the LiErF$_4$ unit cell. The mean fields are

$$|\mathbf{H}_{\text{clock}}^{\text{MF}}| = |\sum_{NN} \mathcal{J}_{\text{clock}} \langle \mathbf{S} \rangle| = -4\mathcal{J}_{\text{clock}} \tag{B.5}$$

Appendix B. h_4 anisotropy and universality class

$$|\mathbf{H}_{\mathrm{Er,n}}^{\mathrm{MF}}| \quad = \quad |\sum_m \mathcal{J}_D j_{xy}^2 \overline{\overline{D}}_{mn}(\mathbf{q}=0)\langle \mathbf{S}_m \rangle| = 60.25\mu eV \quad \forall \mathrm{n}. \tag{B.6}$$

The two models can thus be compared by their respective ratios $\frac{h_4}{|\mathbf{H}_{\mathrm{clock}}^{\mathrm{MF}}|} = \frac{h_4}{4\mathcal{J}_{\mathrm{clock}}}$ and $\frac{h_{4\mathrm{Er}}}{|\mathbf{H}_{\mathrm{Er,n}}^{\mathrm{MF}}|}$ with $h_{4\mathrm{Er}}$ the four-fold planar anisotropy to be determined in LiErF$_4$. There are two potential sources of h$_4$ anisotropy, which we have evaluated: Crystal field and order-by-disorder:

1. In the LiErF$_4$ crystal field, the positive parameters B_l^0, $l = 2, 4, 6$, ensure the magnetic moment is lying in the *ab* crystallographic plane. But the operators $\sum_{l=4,6} B_l^4(c)\mathbf{O}_l^4(c) + B_6^4(s)\mathbf{O}_6^4(s)$ can induce a small planar anisotropy. Calculating the classical energy of the crystal field while rotating a magnetic moment of length j_{xy} gives a four-fold anisotropic energy of $h_{4\mathrm{Er}}^{\mathrm{CF}} = 0.11\mu eV$. This value is negligible relative to $|\mathbf{H}_{Er}^{MF}|$, and thus the crystal field anisotropy alone cannot explain the small β exponent found in our case.

2. The quantum and thermal fluctuations, if anisotropic, may also induce a breaking of the continuous rotational XY symmetry, a phenomenon known as order-by-disorder. To estimate its size, we use C. L. Henley's result for the second order perturbation theory energy correction to the ground-state in the case of a dipolar coupled spin system [58, 59]. The magnetic order in LiErF$_4$ entails a continuous symmetry corresponding to nearest neighbors rotating about the z axis in opposite directions. Writing the effective spin Hamiltonian (eq.4.3) in a rotated frame of reference $\mathbf{S}_i = \hat{\mathbf{l}}_i S_i^x + \hat{\mathbf{m}}_i S_i^y + \hat{\mathbf{n}}_i S_i^z$ with $(\hat{\mathbf{l}}_i, \hat{\mathbf{m}}_i, \hat{\mathbf{n}}_i)$ an orthonormal triad and $\hat{\mathbf{n}}_i$ the spin's classical ground-state direction, the second order correction to the ground state energy is given by

$$\delta E_2 = -\sum_{i<j} 2S|b_{ij}|^2/[h_i + h_j - a_{ij}] \tag{B.7}$$

where $h_i = S\sum_j a_{ij}$, $a_{ij} = \hat{\mathbf{n}}_i^T \overline{\overline{\mathcal{J}}}_{ij} \hat{\mathbf{n}}_j$ and $b_{ij} = \frac{1}{4}(\hat{\mathbf{l}}_i - i\hat{\mathbf{m}}_i)^T \overline{\overline{\mathcal{J}}}_{ij}(\hat{\mathbf{l}}_j - i\hat{\mathbf{m}}_j)$. Rotating the frame of reference in opposite direction every second layer, we find a four-fold anisotropy $h_{4\mathrm{Er}}^{obdo} = 5.26\mu eV$, giving a sizable ratio $\frac{h_{4\mathrm{Er}}^{obdo}}{|\mathbf{H}_{\mathrm{Er,n}}^{\mathrm{MF}}|} = 0.09$. In the work of Taroni *et. al*, $\beta = 0.15$ (which is what we measure in LiErF$_4$) corresponds to $\mathcal{J}_{clock} \simeq |\mathbf{H}^{MF}| \Rightarrow \frac{h_4}{|\mathbf{H}^{MF}|} \simeq 0.25$. The above estimate from order-by-disorder is within a factor of 3 from this result, hence, of the required order of magnitude.

Bearing in mind that LiErF$_4$ and the square lattice clock model are different models, that we compare on the mean-field level, and that we only estimate quantum , not thermal fluctuations, a closer numerical agreement can not be expected.

Bibliography

[1] JI Martin, J. Nogues, K. Liu, JL Vicent, and I.K. Schuller. Ordered magnetic nanostructures: fabrication and properties. *Journal of magnetism and magnetic materials*, 256(1-3):449–501, 2003.

[2] M.V. Lubarda, S. Li, B. Livshitz, E.E. Fullerton, and V. Lomakin. Antiferromagnetically coupled capped bit patterned media for high-density magnetic recording. *Applied Physics Letters*, 98:012513, 2011.

[3] HM Rønnow, R. Parthasarathy, J. Jensen, G. Aeppli, TF Rosenbaum, and DF McMorrow. Quantum phase transition of a magnet in a spin bath. *Science*, 308(5720):389, 2005.

[4] P. B. Chakraborty, P. Henelius, H. Kjønsberg, A. W. Sandvik, and S. M. Girvin. Theory of the magnetic phase diagram of LiHoF$_4$. *Phys. Rev. B*, 70:144411, Oct 2004.

[5] H. M. Rønnow, J. Jensen, R. Parthasarathy, G. Aeppli, T. F. Rosenbaum, D. F. McMorrow, and C. Kraemer. Magnetic excitations near the quantum phase transition in the ising ferromagnet LiHoF$_4$. *Phys. Rev. B*, 75:054426, Feb 2007.

[6] Subir Sachdev. Quantum phase transitions. *Physics World*, 12:33–38, Apr 1999.

[7] Juan J. Alonso and Julio F. Fernández. Monte carlo study of the spin-glass phase of the site-diluted dipolar Ising model. *Phys. Rev. B*, 81:064408, Feb 2010.

[8] Wenhao Wu, D. Bitko, T. F. Rosenbaum, and G. Aeppli. Quenching of the nonlinear susceptibility at a T =0 spin glass transition. *Phys. Rev. Lett.*, 71:1919–1922, Sep 1993.

Bibliography

[9] S. Ghosh, R. Parthasarathy, TF Rosenbaum, and G. Aeppli. Coherent spin oscillations in a disordered magnet. *Science*, 296(5576):2195, 2002.

[10] S. Ghosh, TF Rosenbaum, G. Aeppli, and SN Coppersmith. Entangled quantum states of magnetic dipoles. *Nature*, 425:48, 2003.

[11] M. Schechter and P. C. E. Stamp. Derivation of the low-T phase diagram of LiHo$_x$Y$_{1-x}$F$_4$: A dipolar quantum Ising magnet. *Phys. Rev. B*, 78:054438, Aug 2008.

[12] D. H. Reich, T. F. Rosenbaum, and G. Aeppli. Glassy relaxation without freezing in a random dipolar-coupled Ising magnet. *Phys. Rev. Lett.*, 59:1969–1972, Oct 1987.

[13] P. E. Hansen, T. Johansson, and R. Nevald. Magnetic properties of lithium rare-earth fluorides: Ferromagnetism in LiErF$_4$ and LiHoF$_4$ and crystal-field parameters at the rare-earth and Li sites. *Phys. Rev. B*, 12:5315–5324, Dec 1975.

[14] P. Beauvillain, J. Renard, P. Hansen, et al. Low-temperature magnetic susceptibility of LiErF$_4$: evidence of antiferromagnetic ordering at 0.38 K. *Journal of Physics C: Solid State Physics*, 10:L709, 1977.

[15] G. Mennenga, LJ de Jongh, WJ Huiskamp, and I. Laursen. A comparative study of the magnetic ordering specific heats of four dipolar magnets: LiRF$_4$ (R= Er, Dy, Ho, Tb). *Journal of magnetism and magnetic materials*, 44(1-2):48–58, 1984.

[16] P. De Groot, P. Janssen, F. Herlach, G. De Vos, and J. Witters. A magnetic resonance spectrometer for fir frequencies; measurement on LiErF$_4$. *International journal of infrared and millimeter waves*, 5(2):135–146, 1984.

[17] J. Magariño, J. Tuchendler, P. Beauvillain, and I. Laursen. EPR experiments in LiTbF$_4$, LiHoF$_4$, and LiErF$_4$ at submillimeter frequencies. *Phys. Rev. B*, 21:18–28, Jan 1980.

[18] C. Kraemer, N. Nikseresht, Julian O. Piatek, N. Tsyrulin, B. Dalla Piazza, K. Kiefer, B. Klemke, Thomas F. Rosenbaum, G. Aeppli, Ché. Gannarelli, K. Prokes, T. Podlesnyak, A. Strässle, L. Keller, O. Zaharko, K. Krämer, and H.M. Rø nnow. Dipolar antiferromagnetism and quantum criticality in LiErF$_4$. *Submitted to Science*.

[19] Conradin Kraemer. *Quantum Phase Transitions in a Magnetic Model System.* PhD thesis, 2009.

[20] S. Sachdev. *Quantum phase transitions.* Wiley Online Library, 2007.

[21] M. Vojta. Quantum phase transitions. *Reports on Progress in Physics*, 66:2069, 2003.

[22] A. Husmann, J. Brooke, T. F. Rosenbaum, X. Yao, and J. M. Honig. Nonlinear electric field effects at a continuous mott-hubbard transition. *Phys. Rev. Lett.*, 84:2465–2468, Mar 2000.

[23] S. L. Sondhi, S. M. Girvin, J. P. Carini, and D. Shahar. Continuous quantum phase transitions. *Rev. Mod. Phys.*, 69:315–333, Jan 1997.

[24] H. P. Christensen. Spectroscopic analysis of $LiHoF_4$ and $LiErF_4$. *Phys. Rev. B*, 19:6564–6572, Jun 1979.

[25] KWH Stevens. Matrix elements and operator equivalents connected with the magnetic properties of rare earth ions. *Proceedings of the Physical Society. Section A,* 65:209, 1952.

[26] J. Jensen and A.R. Mackintosh. *Rare earth magnetism.* Clarendon Oxford, 1991.

[27] B. Dalla Piazza and P.H.M. Rønnow. Mean-field calculations on the diluted dipolar magnet $LiHo_{1-x}Y - xF_4$, 2009.

[28] G.L. Squires. *Introduction to the theory of thermal neutron scattering.* Dover Pubns, 1996.

[29] A. Furrer, J. Mesot, and T. Strässle. *Neutron scattering in condensed matter physics.* World Scientific Singapore, 2009.

[30] K. Lefmann. Neutron scattering: Theory, instrumentation, and simulation, 2010.

[31] S.W. Lovesey and SW Lovesey. *Theory of neutron scattering from condensed matter.* Clarendon press Oxford, 1984.

[32] B. Schmid, B. Halg, A. Furrer, W. Urland, and R. Kremer. Structure and crystal fields of $PrBr_3$ and $PrCl_3$: A neutron study. *Journal of Applied Physics*, 61(8):3426–3428, 1987.

Bibliography

[33] G. Shirane, S.M. Shapiro, and J.M. Tranquada. *Neutron scattering with a triple-axis spectrometer: basic techniques.* Cambridge Univ Pr, 2002.

[34] RI Bewley, JW Taylor, and SM Bennington. Let, a cold neutron multi-disk chopper spectrometer at ISIS. *Nuclear Instruments and Methods in Physics Research Section A: Accelerators, Spectrometers, Detectors and Associated Equipment*, 2011.

[35] K Kiefer. Diplomarbeit, 1997.

[36] K Kiefer. Dissertation, 2004.

[37] Jose Rodriguez. *Study of the dipolar Ising system* $LiHo_xY_{1-x}F_4$ *using* μSR. PhD thesis, 2009.

[38] T. Hahn et al. *International Tables for Crystallography, Vol. A: Space-group symmetry, No.88.* 2005.

[39] P. Beauvillain, J. P. Renard, I. Laursen, and P. J. Walker. Critical behavior of the magnetic susceptibility of the uniaxial ferromagnet $LiHoF_4$. *Phys. Rev. B*, 18:3360–3368, Oct 1978.

[40] J. Als-Nielsen, L. M. Holmes, and H. J. Guggenheim. Wave-vector-dependent susceptibility at $T > T_c$ in a dipolar ising ferromagnet. *Phys. Rev. Lett.*, 32:610–613, Mar 1974.

[41] N. Craig and T. Lester. The hitchhiker's guide to the dilution refrigerator, 2004.

[42] Sushil K. Misra and Joshua Felsteiner. Low-temperature ordered states of Lithium Rare-earth tetraFluorides $LiRF_4$). *Phys. Rev. B*, 15:4309–4312, May 1977.

[43] J. M. Luttinger and L. Tisza. Theory of dipole interaction in crystals. *Phys. Rev.*, 70:954–964, Dec 1946.

[44] J. P. Sattler and J. Nemarich. Electron-Paramagnetic-Resonance spectra of Nd^{3+}, Dy^{3+}, Er^{3+}, and Yb^{3+} in Lithium Yttrium Fluoride. *Phys. Rev. B*, 4:1–5, Jul 1971.

[45] MT Hutchings. Point-charge calculations of energy levels of magnetic ions in crystalline electric fields. *Solid State Physics*, 16:227–273, 1964.

[46] K. Andres. Combined electron-nuclear magnetic-ordering phenomena in singlet-ground-state systems. *Phys. Rev. B*, 7:4295–4300, May 1973.

[47] MJM Leask, MR Wells, RCC Ward, SM Hayden, and J. Jensen. Magnetic excitations in the dipole-coupled singlet-singlet system HoF_3. *Journal of Physics: Condensed Matter*, 6:505, 1994.

[48] AP Ramirez and J. Jensen. The nuclear heat capacity of HoF_3. *Journal of Physics: Condensed Matter*, 6:L215, 1994.

[49] M. Nikolo. Superconductivity: A guide to alternating current susceptibility measurements and alternating current susceptometer design. *American Journal of Physics*, 63(1):57–65, 1995.

[50] David Bitko. *Order and disorder in a model quantum magnet.* PhD thesis, 1997.

[51] P.M. Chaikin and T.C. Lubensky. *Principles of condensed matter physics.* Cambridge Univ Pr, 2000.

[52] RF Wang, C. Nisoli, RS Freitas, J. Li, W. McConville, BJ Cooley, MS Lund, N. Samarth, C. Leighton, VH Crespi, et al. Artificial spin ice in a geometrically frustrated lattice of nanoscale ferromagnetic islands. *Nature*, 439(7074):303–306, 2006.

[53] L. A. S. Mól and B. V. Costa. Anisotropic heisenberg model with dipolar interactions: Monte carlo simulations of the planar-to-paramagnetic phase transition in a bilayer system. *Phys. Rev. B*, 79:054404, Feb 2009.

[54] F. Kagawa, K. Miyagawa, and K. Kanoda. Unconventional critical behaviour in a quasi-two-dimensional organic conductor. *Nature*, 436(7050):534–537, 2005.

[55] A. Taroni, S.T. Bramwell, and P.C.W. Holdsworth. Universal window for two-dimensional critical exponents. *Journal of Physics: Condensed Matter*, 20:275233, 2008.

[56] DM Silevitch, D. Bitko, J. Brooke, S. Ghosh, G. Aeppli, and TF Rosenbaum. A ferromagnet in a continuously tunable random field. *Nature*, 448(7153):567–570, 2007.

Bibliography

[57] J. Villain, R. Bidaux, J.P. Carton, and R. Conte. Order as an effect of disorder. *Journal de Physique*, 41(11):1263–1272, 1980.

[58] C.L. Henley. Ordering by disorder: Ground-state selection in fcc vector antiferro-magnets. *Journal of Applied Physics*, 61(8):3962–3964, 1987.

[59] Christopher L. Henley. Selection by quantum fluctuations of dipolar order in a diamond lattice. *Phys. Rev. Lett.*, 73:2788–2788, Nov 1994.

[60] Sona Prakash and Christopher L. Henley. Ordering due to disorder in dipolar magnets on two-dimensional lattices. *Phys. Rev. B*, 42:6574–6589, Oct 1990.

[61] M. Schechter and P. C. E. Stamp. Significance of the hyperfine interactions in the phase diagram of $LiHo_xY_{1-x}F_4$. *Phys. Rev. Lett.*, 95:267208, Dec 2005.

[62] A. Heidemann, D. Richter, and KHJ Buschow. Investigation of the hyperfine fields in the compounds $LaCo_{13}$, $LaCo_5$, YCo_5 and $ThCo_5$ by means of inelastic neutron scattering. *Zeitschrift für Physik B Condensed Matter*, 22(4):367–372, 1975.

[63] T. Chatterji and G. J. Schneider. Low-energy nuclear spin excitations in CoO. *Phys. Rev. B*, 79:212409, Jun 2009.

[64] T. Chatterji and GJ Schneider. Anomalous hyperfine interaction in CoF_2 investigated by high resolution neutron spectroscopy. *Journal of Physics: Condensed Matter*, 21:436008, 2009.

[65] RI Schermer and M. Blume. Polarization effects in slow-neutron scattering. III. nuclear polarization. *Physical Review*, 166:554–561, 1968.

[66] G. Ehlers, E. Mamontov, M. Zamponi, K. C. Kam, and J. S. Gardner. Direct observation of a nuclear spin excitation in $Ho_2Ti_2O_7$. *Phys. Rev. Lett.*, 102:016405, Jan 2009.

[67] R. C. Johnson, K. H. Chen, S. R. Giblin, J. S. Lord, A. Amato, C. Baines, B. Barbara, B. Z. Malkin, and M. J. Graf. μSR study of spin dynamics in $LiY_xHo_{1-x}F_4$. *Phys. Rev. B*, 83:174440, May 2011.

[68] J. Rodriguez, A. A. Aczel, J. P. Carlo, S. R. Dunsiger, G. J. MacDougall, P. L. Russo, A. T. Savici, Y. J. Uemura, C. R. Wiebe, and G. M. Luke. Study of the ground

state properties of $LiHo_xY_{1-x}F_4$ using muon spin relaxation. *Phys. Rev. Lett.*, 105:107203, Sep 2010.

[69] SJ Payne, MJ Harris, ME Hagen, and MT Dove. A neutron diffraction study of the order-disorder phase transition in Sodium Nitrate. *Journal of Physics: Condensed Matter*, 9:2423, 1997.

[70] VA Dyadkin, SV Grigoriev, EV Moskvin, SV Maleyev, D. Menzel, J. Schoenes, and H. Eckerlebe. Critical scattering in the helimagnets $Fe_{1-x}Co_xSi$. *Physica B: Condensed Matter*, 404(17):2520–2523, 2009.

[71] A. Biltmo and P. Henelius. Phase diagram of the dilute magnet $LiHo_xY_{1-x}F_4$. *Phys. Rev. B*, 76:054423, Aug 2007.

[72] A. Biltmo and P. Henelius. Low-temperature properties of the dilute dipolar magnet $LiHo_xY_{1-x}F_4$. *Phys. Rev. B*, 78:054437, Aug 2008.

[73] Moshe Schechter and Nicolas Laflorencie. Quantum spin glass and the dipolar interaction. *Phys. Rev. Lett.*, 97:137204, Sep 2006.

[74] D. H. Reich, B. Ellman, J. Yang, T. F. Rosenbaum, G. Aeppli, and D. P. Belanger. Dipolar magnets and glasses: Neutron-scattering, dynamical, and calorimetric studies of randomly distributed ising spins. *Phys. Rev. B*, 42:4631–4644, Sep 1990.

[75] S. M. A. Tabei, M. J. P. Gingras, Y.-J. Kao, P. Stasiak, and J.-Y. Fortin. Induced random fields in the $LiHo_xY_{1-x}F_4$ quantum ising magnet in a transverse magnetic field. *Phys. Rev. Lett.*, 97:237203, Dec 2006.

[76] T. Senthil. Properties of the random-field Ising model in a transverse magnetic field. *Phys. Rev. B*, 57:8375–8380, Apr 1998.

[77] Moshe Schechter. $LiHo_xY_{1-x}F_4$ as a random-field Ising ferromagnet. *Phys. Rev. B*, 77:020401, Jan 2008.

[78] DM Silevitch, G. Aeppli, and TF Rosenbaum. Switchable hardening of a ferromagnet at fixed temperature. *Proceedings of the National Academy of Sciences*, 107(7):2797, 2010.

Bibliography

[79] A. Schröder, G. Aeppli, E. Bucher, R. Ramazashvili, and P. Coleman. Scaling of magnetic fluctuations near a quantum phase transition. *Phys. Rev. Lett.*, 80:5623–5626, Jun 1998.

[80] Q. Zhang and B. Yan. Hydrothermal synthesis and characterization of LiREF$_4$ (re= y, tb- lu) nanocrystals and their core- shell nanostructures. *Inorganic chemistry*, 2010.

Curriculum Vitae

Neda Nikseresht Ghanepour

EPFL - SB - ICMP - LQM
station 3
CH-1015 Lausanne, Switzerland
tel: +41-21-693-44-75, *fax*: +41-21-693-46-66
e-mail: neda.nikseresht@epfl.ch

personal address:
Route de la Plaine, 5
CH-1022 Chavannes/Renens
e-mail: nedanikseresht@gmail.com
mobile: +41-78-927-92-94

date of birth: July 14th, 1982
place of birth: Tehran, Iran
Nationality: Iran
marital status: single.

Education

05/2008-present:	**PhD** in the Laboratory for Quantum Magnetism, EPFL, Lausanne, Switzerland. *PhD thesis*: Classical and Quantum Critical Phenomena in the Dipolar Antiferromagnet $LiErF_4$. *supervisor*: Prof. H. M. Rønnow.
10/2005-11/2007	**MS** in Sharif University of Technology, Tehran, Iran. *Diploma thesis*: Syntheses and study of the effect of Pr ion substitution for Ce in $RuGd_{1.5}Ce_{0.5-x}Pr_xSr_2Cu_2O_{10-\delta}$ rutheno-cuprates. *Supervisor*: Prof. M. Akhavan.
02/2001-07/2004:	**BS** in Zanjan University, Zanjan, Iran.
10/1996-07/2000:	**High school degree** in Moalem high school, Tehran, Iran.

Experience

05/2008-12/2011:	**Theaching Assistant** in EPFL. Supervising Bachelor Students for practical works in optics, metrology and superconductivity/magentism. Corrections of students' reports.
01/2010-present:	**Responsible for the SQUID magnetometer** of our labortory. Helping scientists to handle their experiments, and measurements for collaboration works.

Skills

Languages:	farsi: native speaker english: fluent

french: basic

Computer skills:	MatLab, LaTeX, SolidWork, Microsoft Office suite.
Laboratory skills:	• DC magnetization measurements using SQUID magnetometer
	• AC Susceptibility measurements
	• Handling Neutron scattering experiments elastic/inelastic
	• Vibrating Sample Magnetometer (VSM)
	• Resistivity measurements using 4-point probe technique
	• Magnetoresistance measurements
	• Calsination and sintering furnaces
	• Solid-State reaction synthesis method in different atmospheres
	• Vacuum techniques
	• XRD

Workshops and schools attended

July 2008:	Summer school on Superconductivity, Taiwan.
September 2009:	11th Oxford School on Neutron Scattering, Oxford, UK.
May 2010:	Muon Spectroscopy training school, ISIS, Oxford, UK.
August 2010:	Summer school on Condensed Matter Research, Zuoz, Switzerland.

Publications and contributions to conferences

• S. Fallahi, M. Mazaheri, **N. Nikseresht**, H.M. Rønnow, and M. Akhavan, *Effect of Ca substitution on crystal structure and superconducting properties of ferromagnetic superconductor $RuSr_{2-x}Ca_xGd_{1.4}Ce_{0.6}Cu_2O_{10-\delta}$,* Journal of Magnetism and Magnetic Materials **34**, 949 (2012).

• G. Deng, D.M. Radheep, R. Thiyagarajan, E. Pomjakushina, S. Wang, **N. Nikseresht**, S. Arumugam, and K. Conder, *High oxygen pressure single crystal growth of highly Ca-doped spin ladder compound $Sr_{14-x}Ca_xCu_{24}O_{41}$ (x > 12),* Journal of Crystal Growth **327**, 182 (2011).

• S. Wang, E. Pomjakushina, T. Shiroka, G. Deng, **N. Nikseresht**, C. Ruegg, H.M. Rønnow, and K. Conder, *Crystal growth and characterization of the dilutable frustrated spin-ladder compound $Bi(Cu_{1-x}Zn_x)_2PO_6$,* Journal of Crystal Growth **313**, 51 (2010).

• **N. Nikseresht**, A. Khajehnezhad, H. Hadipour, and M. Akhavan, *The effect of chemical pressure in rutheno-cuprates,* Physica C: Superconductivity and its Applications **470**, 285 (2010).

• A Khajehnezhad, **N. Nikseresht**, H. Hadipour, and M. Akhavan, *Comparing the physical properties of Pr/Gd and Pr/Ce substitutions in $Ru(Gd_{1.5}Ce_{0.5})Sr_2Cu_2O_{10-\delta}$,* European

122

Physical Journal B **63**, 461 (2008).

accepted article:

• C. Kraemer, **N. Nikseresht**, J. Piatek, N. Tsyrulin, B. Dalla Piazza, K. Kiefer, B. Klemke, T.F. Rosenbaum, G. Aeppli, C. Gannarelli, K. Prokes, A. Podlesnyak, T. Strässle, L. Keller, O. Zaharko, K.W. Krämer, and H.M. Rønnow, *Dipolar antiferromagnetism and quantum criticality in LiErF$_4$*, accepted to *Science.*

articles in preparation:

• **N. Nikseresht**, B. Dalla Piazza, C. Kraemer, J. Jesen, and H.M. Rønnow, *Phase diagram studies of LiHo$_x$Y$_{1-x}$F$_4$.*
• **N. Nikseresht** *et al., Correlation length studies of LiErF$_4$.*
• **N. Nikseresht** *et al., Excitations and dynamics in LiErF$_4$.*

selected contributions to conferences:

• (oral presentation) **N. Nikseresht**, A. Khajehnezhad, H. Hadipour, and M. Akhavan, *Effect of Pr substitution on competition between magnetism and superconductivity in RuGd$_{1.5}$Ce$_{0.5-x}$Pr$_x$Sr$_2$Cu$_2$O$_{10}$ rutheno-cuprates*, Conference on Magentic and Super-conducting Materials (MSM), sep. 2007, Khiva, Uzbekistan.
• (oral presentation) **N. Nikseresht**, H. Hadipour, and M. Akhavan, *Effect of chemical pressure on superconductivity in Pr-doped Ru-1222 (Gd) Compounds*, Internationnal Conference on Superconductivity, July 2008, Taiwan.
• (oral presentation) **N. Nikseresht**, H. Rønnow, *Order parameter investigation of LiErF$_4$ magnetic system by μSR measurement*, μSR Users' meeting, BVRA 2010, Paul Scherrer Institut (PSI), Jan 2010, Switzerland.
• (poster presentation) **N. Nikseresht**, C. Kraemer, K. Kiefer, B. Klemke, and H.M. Rønnow, *Specific heat study of criticality in the dipolar XY antiferromagnet LiErF$_4$*, International Conference on Magnetism (ICM) 2009, Karlsruhe, Germany.